Optical conductivity

- complex dielectric constant: $\epsilon = \epsilon_1 + i\epsilon_2$

- by definition: $\sqrt{\epsilon} = n + ik = \hat{n}$

$$\boxed{\epsilon_1 = n^2 - k^2 \qquad \epsilon_2 = 2nk}$$

- with complex conductivity: $\sigma = \sigma_1 + i\sigma_2$

  and $\epsilon = 1 + \dfrac{i\sigma}{\epsilon_0 \omega}$

$$\boxed{\sigma_1 = \epsilon_0 \epsilon_2 \omega \qquad \sigma_2 = \epsilon_0 (1 - \epsilon_1)\omega}$$

	Dielectric constant $\hat{\epsilon}$	Conductivity $\hat{\sigma}$	Refractive index $\hat{N}$
$\hat{\epsilon}$	$\hat{\epsilon} = \epsilon_1 + \mathrm{i}\epsilon_2$	$\epsilon_1 = 1 - \frac{4\pi\sigma_2}{\omega}$ $\epsilon_2 = \frac{4\pi\sigma_1}{\omega}$	$\epsilon_1 = \frac{n^2-k^2}{\mu_1}$ $\epsilon_2 = \frac{2nk}{\mu_1}$
$\hat{\sigma}$	$\sigma_1 = \frac{\omega\epsilon_2}{4\pi}$ $\sigma_2 = (1-\epsilon_1)\frac{\omega}{4\pi}$	$\hat{\sigma} = \sigma_1 + \mathrm{i}\sigma_2$	$\sigma_1 = \frac{nk\omega}{2\pi\mu_1}$ $\sigma_2 = \left(1 - \frac{n^2-k^2}{\mu_1}\right)\frac{\omega}{4\pi}$
$\hat{N}$	$n = \left\{\frac{\mu_1}{2}\left[\epsilon_1^2+\epsilon_2^2\right]^{1/2} + \frac{\epsilon_1\mu_1}{2}\right\}^{1/2}$ $k = \left\{\frac{\mu_1}{2}\left[\epsilon_1^2+\epsilon_2^2\right]^{1/2} - \frac{\epsilon_1\mu_1}{2}\right\}^{1/2}$	$n = \left\{\frac{\mu_1}{2}\left[\left(1-\frac{4\pi\sigma_2}{\omega}\right)^2 + \left(\frac{4\pi\sigma_1}{\omega}\right)^2\right]^{1/2} + \frac{\mu_1}{2} - \frac{2\pi\mu_1\sigma_2}{\omega}\right\}^{1/2}$ $k = \left\{\frac{\mu_1}{2}\left[\left(1-\frac{4\pi\sigma_2}{\omega}\right)^2 + \left(\frac{4\pi\sigma_1}{\omega}\right)^2\right]^{1/2} - \frac{\mu_1}{2} + \frac{2\pi\mu_1\sigma_2}{\omega}\right\}^{1/2}$	$\hat{N} = n + \mathrm{i}k$

Table 7.1 Free electron density and plasma properties of some metals. The figures are for room temperature unless stated otherwise. The electron densities are based on data taken from Wyckoff (1963). The plasma frequency ω_p is calculated from eqn 7.6, and λ_p is the wavelength corresponding to this frequency.

Metal	Valency	N ($10^{28}\,m^{-3}$)	$\omega_p/2\pi$ (10^{15} Hz)	λ_p (nm)
Li (77 K)	1	4.70	1.95	154
Na (5 K)	1	2.65	1.46	205
K (5 K)	1	1.40	1.06	282
Rb (5 K)	1	1.15	0.96	312
Cs (5 K)	1	0.91	0.86	350
Cu	1	8.47	2.61	115
Ag	1	5.86	2.17	138
Au	1	5.90	2.18	138
Be	2	24.7	4.46	67
Mg	2	8.61	2.63	114
Ca	2	4.61	1.93	156
Al	3	18.1	3.82	79

Experimentelles Beispiel: Aluminium

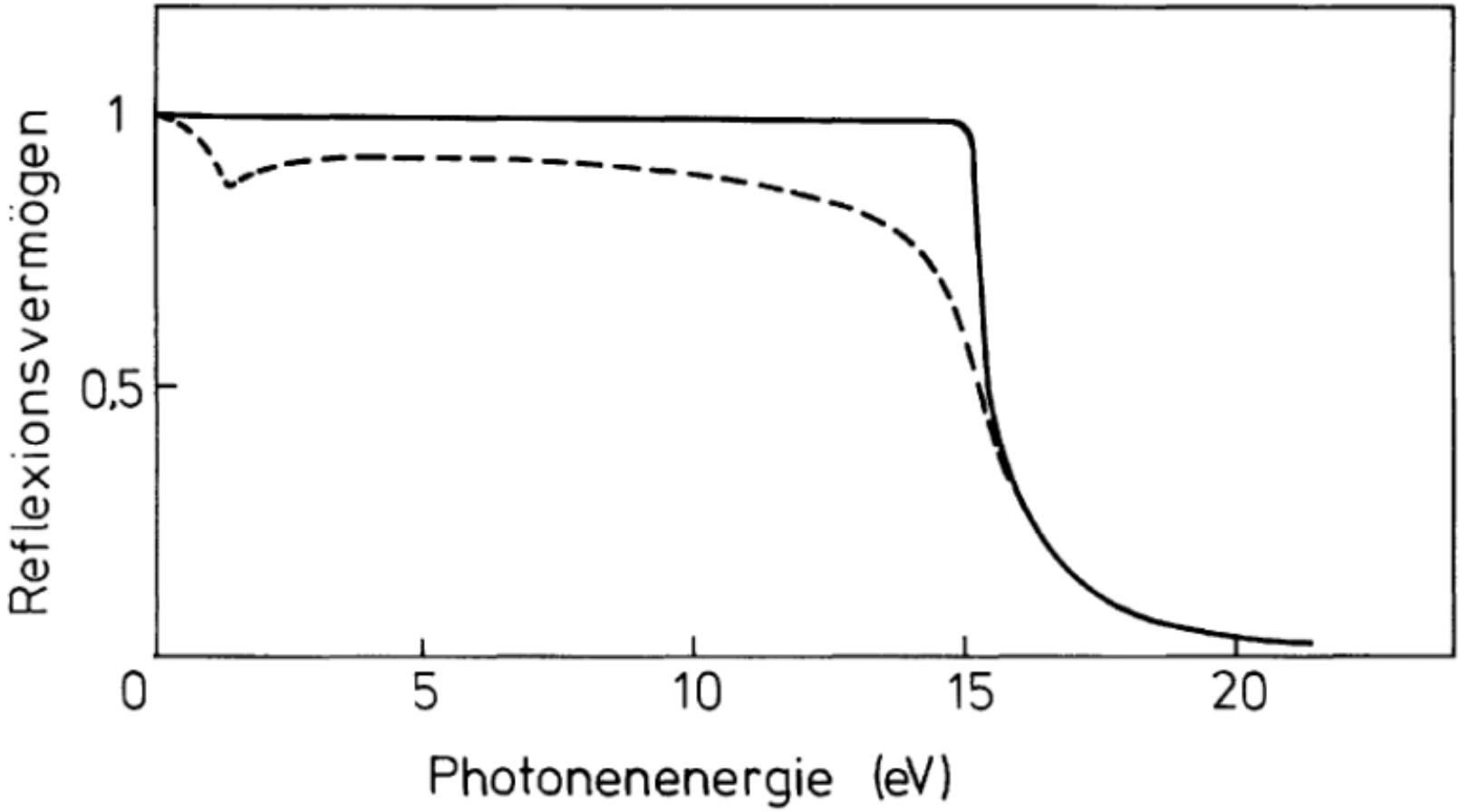

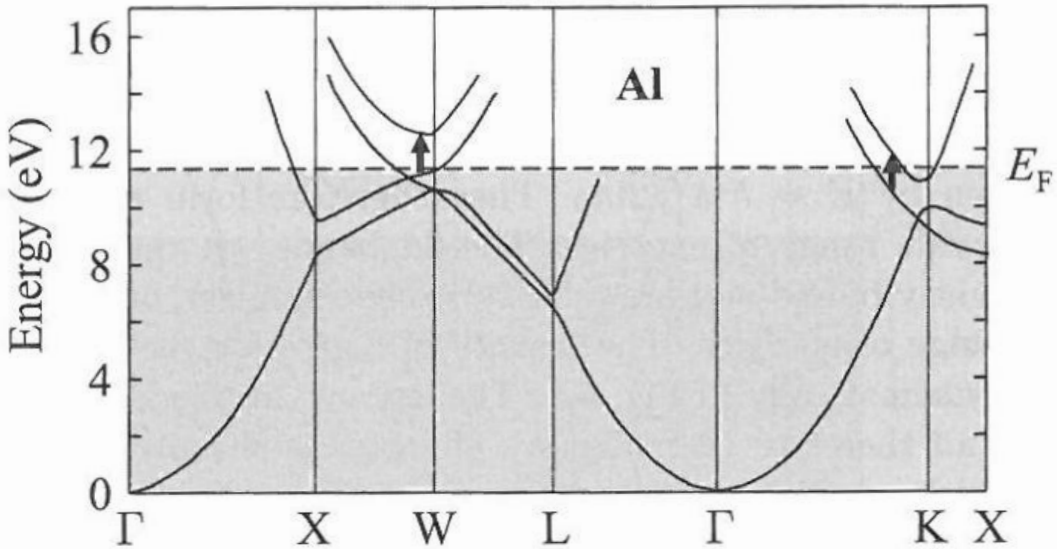

Fig. 7.3 Band diagram of aluminium. The transitions at the W and K points that are responsible for the reflectivity dip at 1.5 eV are labelled. After Segall (1961), © American Physical Society, reprinted with permission.

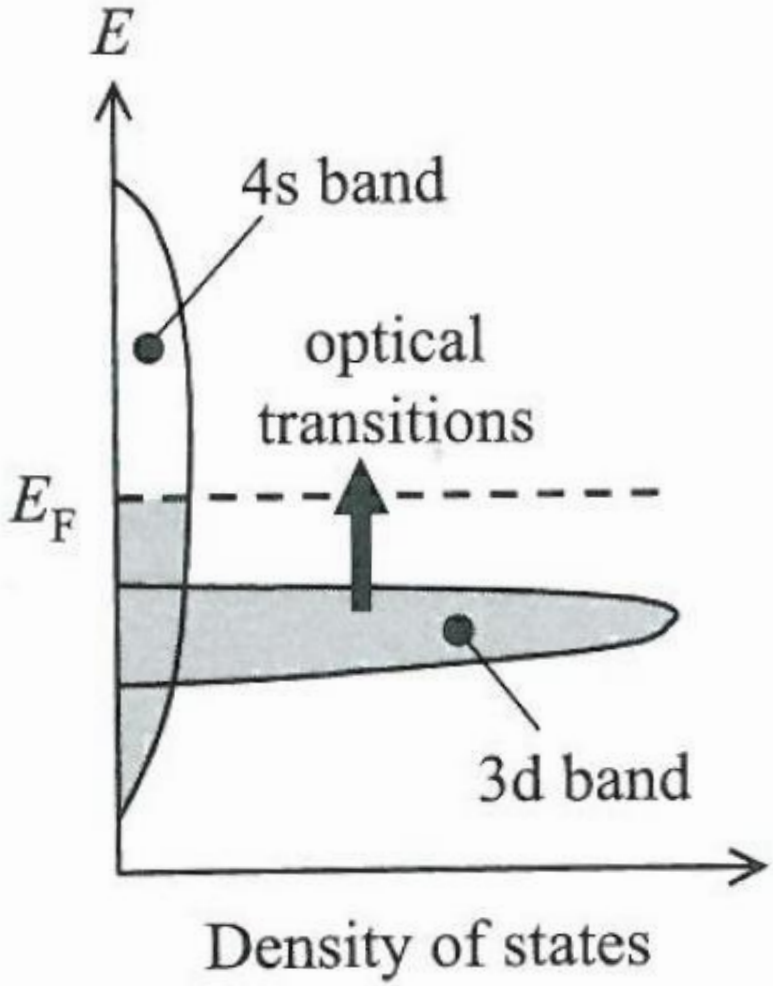

Fig. 7.4 Schematic density of states for the 3d and 4s bands of a transition metal such as copper.

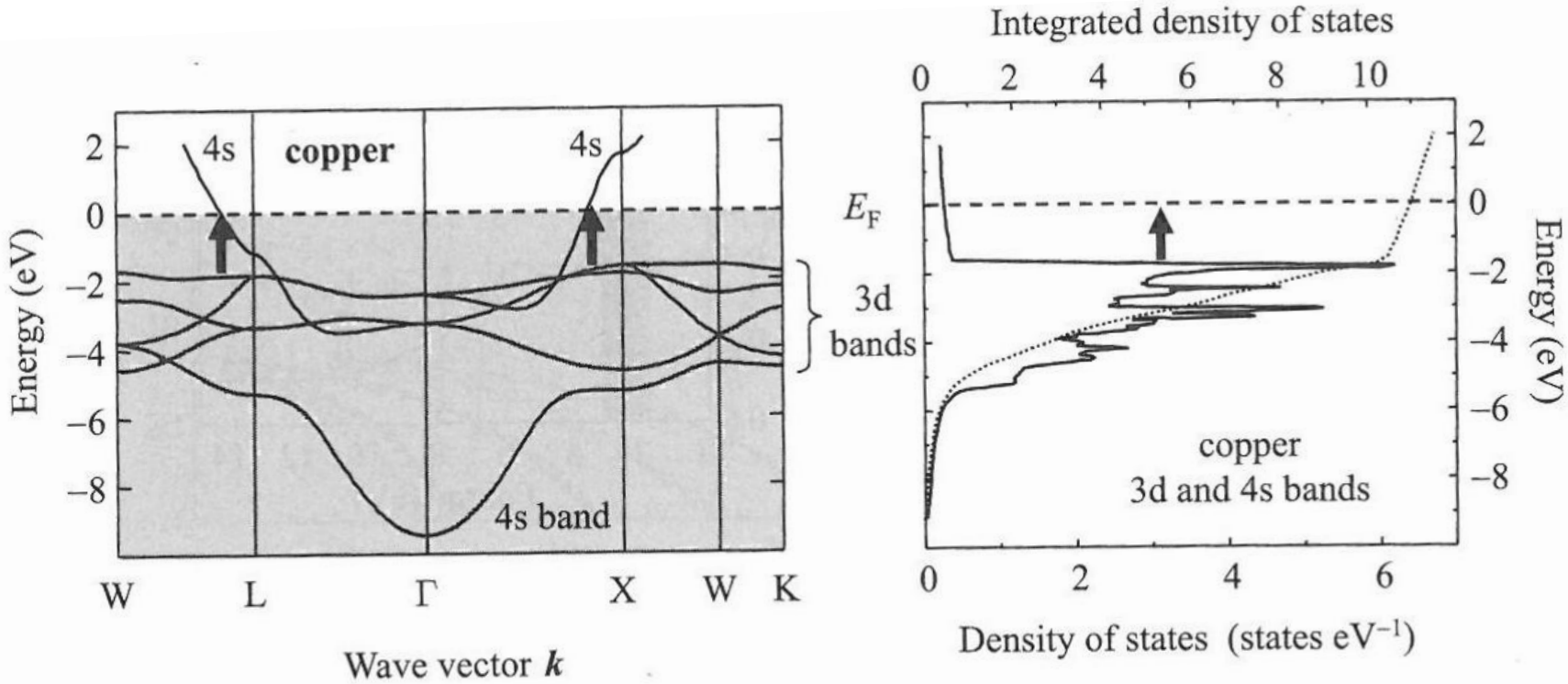

Fig. 7.5 Calculated band structure of copper. The transitions from the 3d bands responsible for the interband transit around 2 eV are identified. The right-hand side of the figure shows the density of states calculated from the band structure. strongly peaked features between about −2 eV and −5 eV are due to the 3d bands. The dotted line is the integrated densit states. The Fermi level (defined here as $E = 0$) corresponds to the energy at which the integrated density of states is equa 11. After Moruzzi et al. (1978).

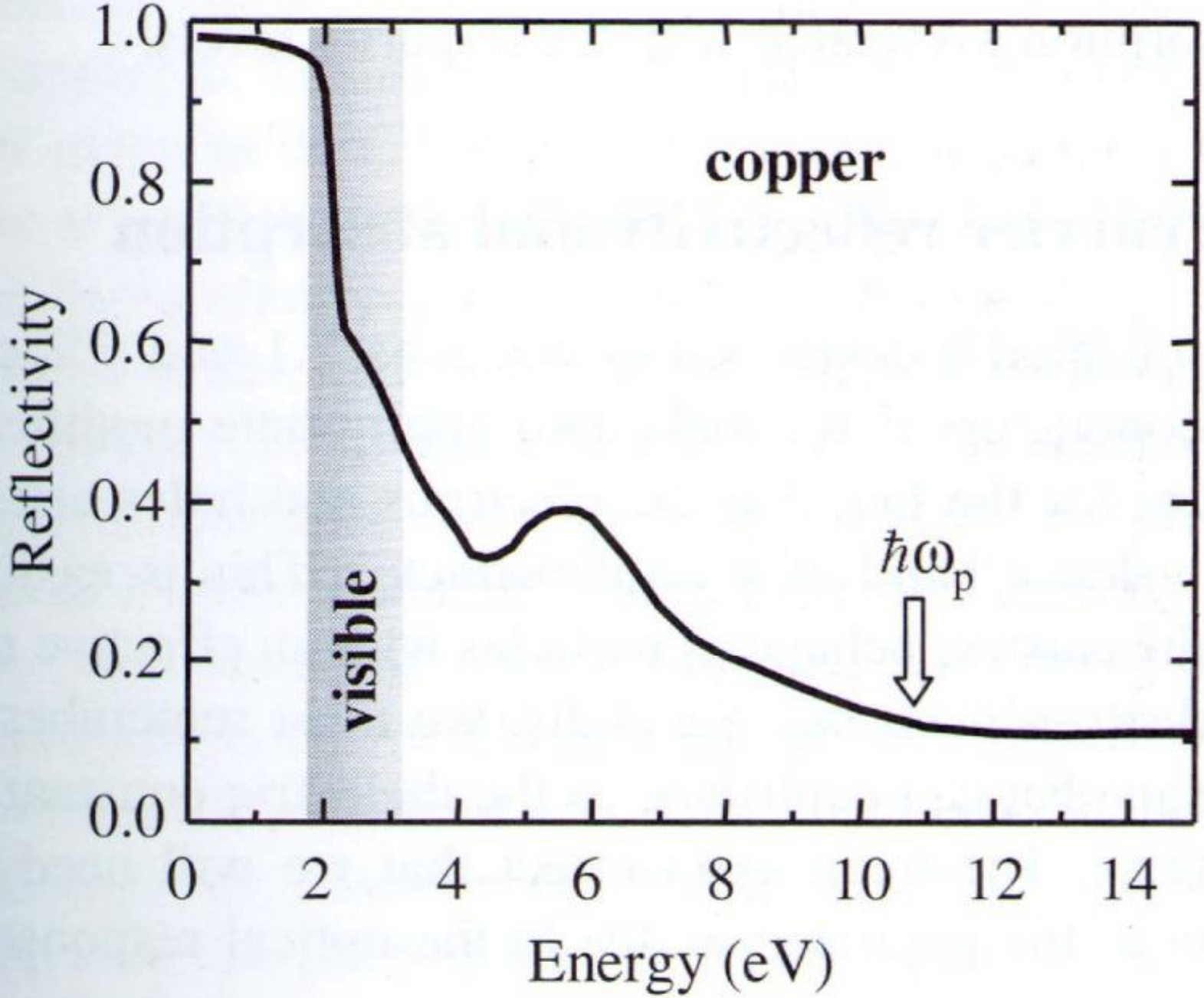
copper
visible
$\hbar\omega_p$
Reflectivity
Energy (eV)
1.0
0.8
0.6
0.4
0.2
0.0
0
2
4
6
8
10
12
14

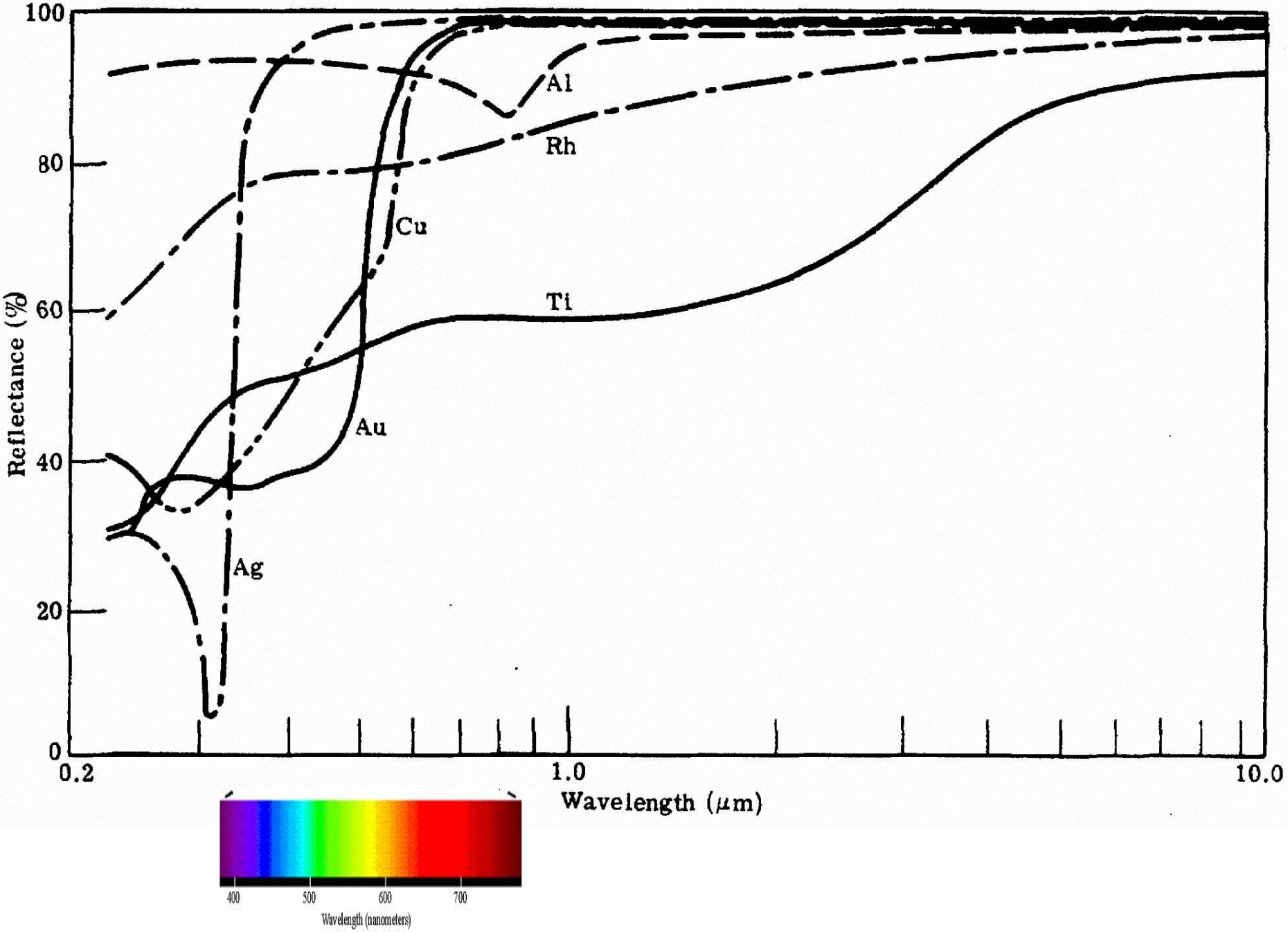
100
80
60
40
20
0
Reflectance (%)
0.2
1.0
10.0
Wavelength (μm)
Al
Rh
Cu
Ti
Au
Ag
400
500
600
700
Wavelength (nanometers)

Experimentelles Beispiel: Isolator-Metall-Phasenübergang in Manganaten

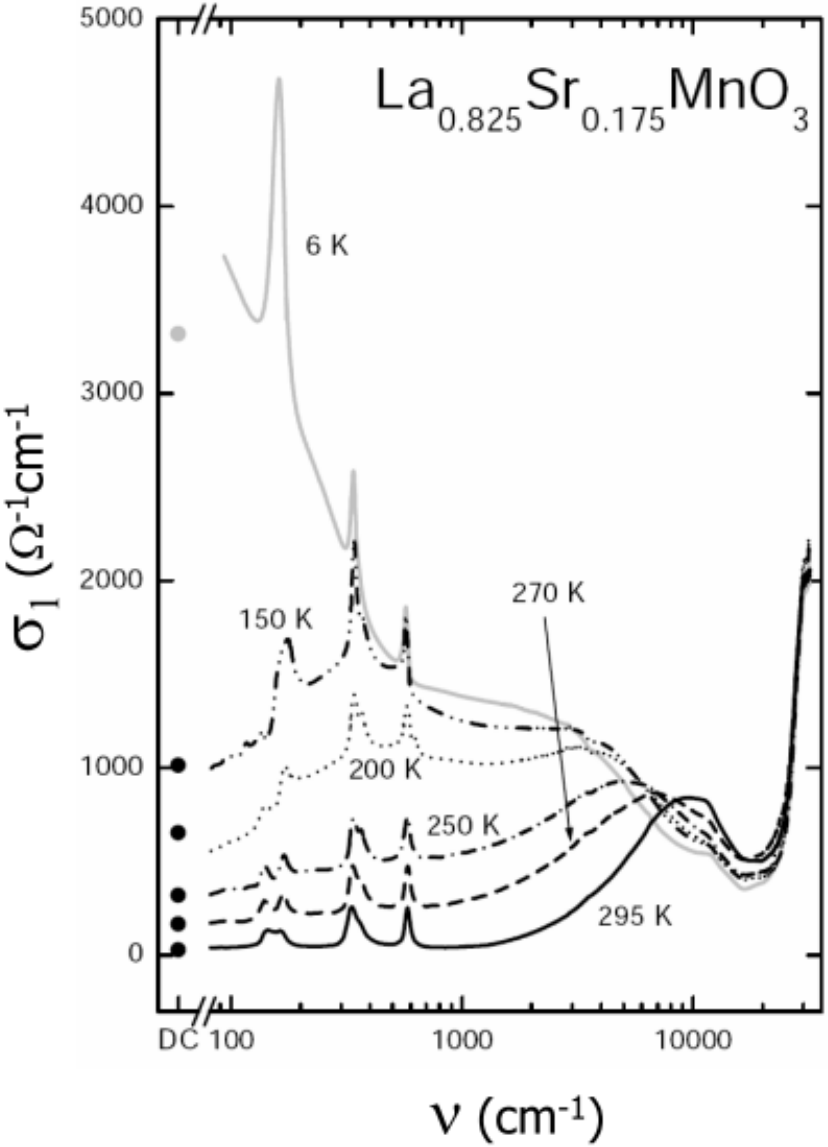

Modell

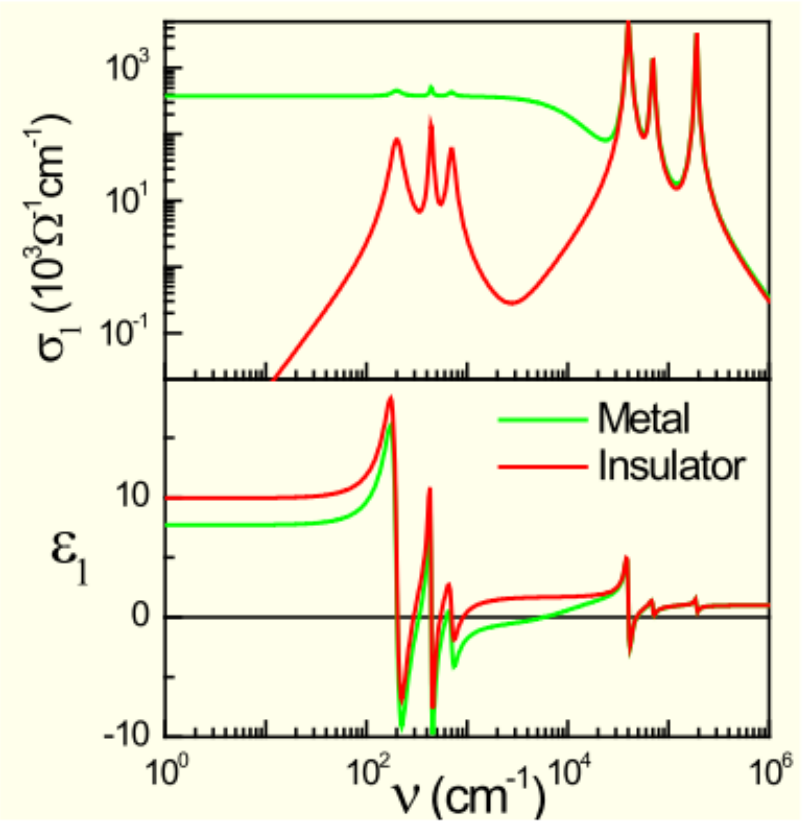

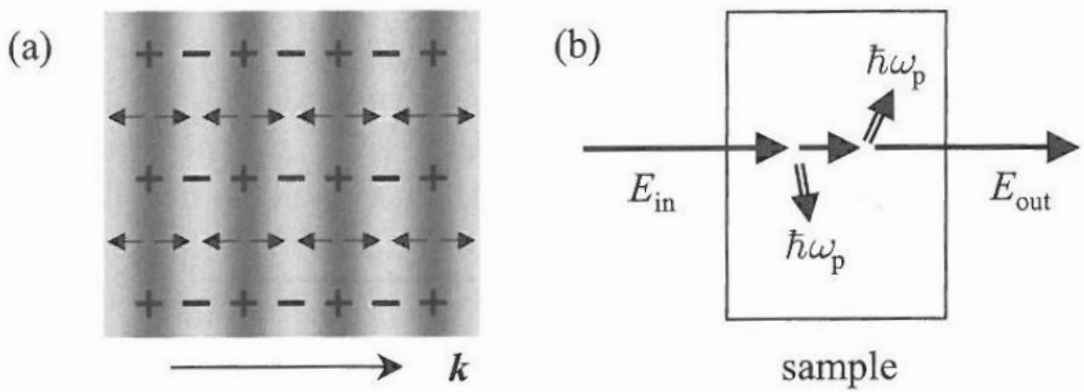

Fig. 7.12 (a) Charge fluctuations in a free carrier plasma oscillation. The lighter regions denote areas with excess electron densities. The small arrows indicate the direction of the electric fields, which are parallel to the direction of propagation of the wave, as indicated by its wave vector $\boldsymbol{k}$. (b) Excitation of plasmons by inelastic scattering of particles. The case in which two plasmons are excited is shown. For metals, electrons with keV energies are used, but for doped semiconductors, optical frequency photons have sufficient energy.

Surface plasmon, localized surface plasmon

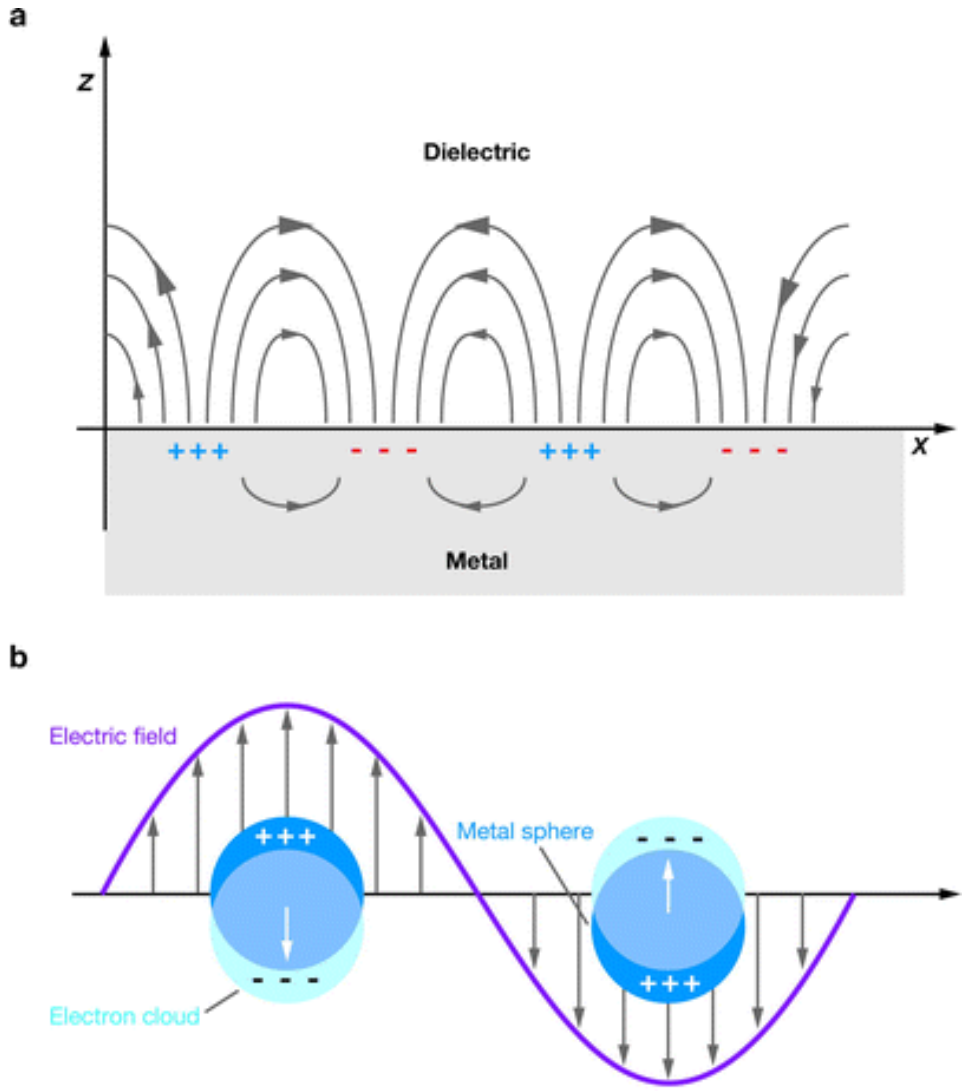

Willets KA, Van Duyne RP. 2007.
Annu. Rev. Phys. Chem. 58:267–97

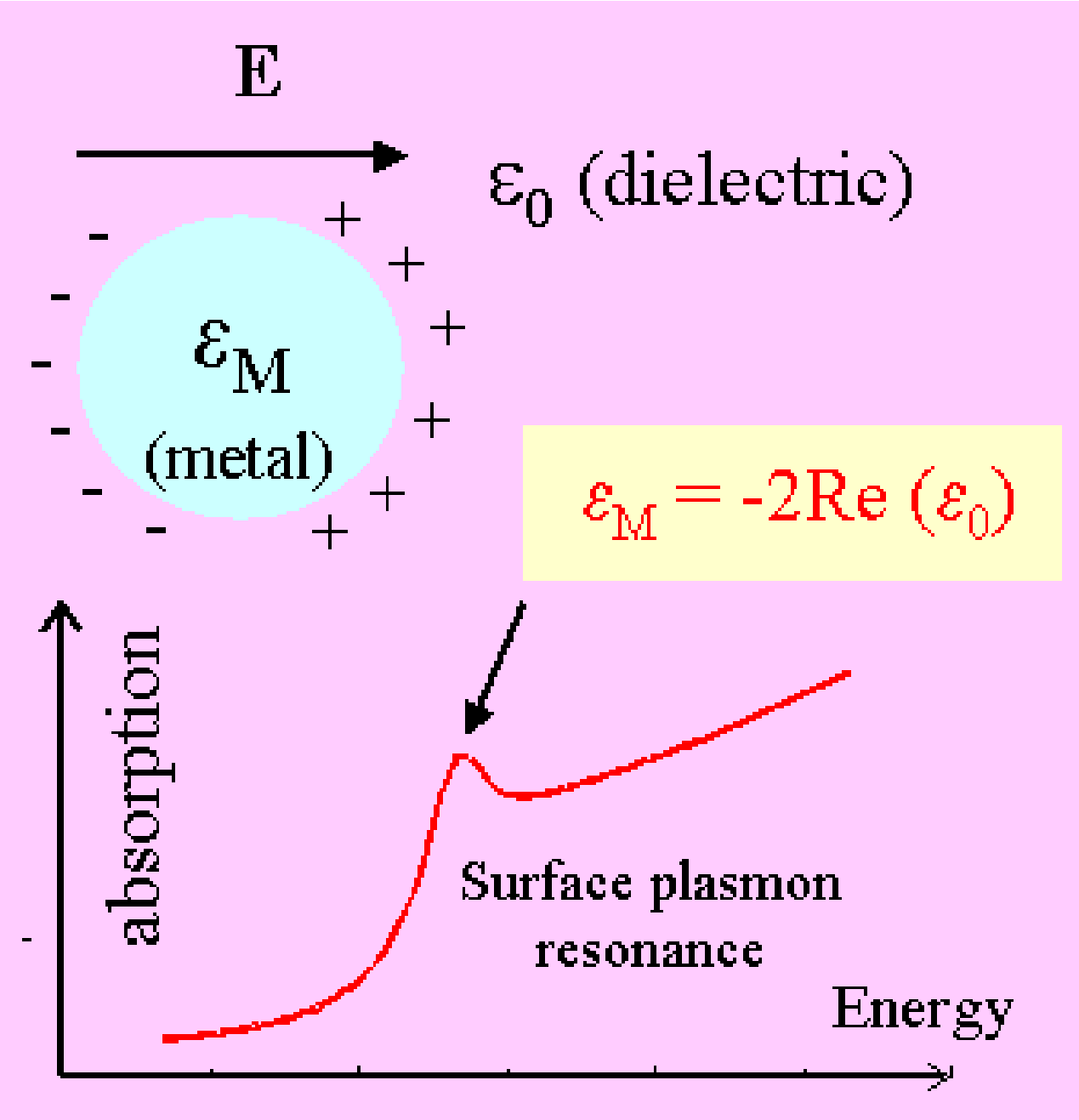
E
ε_0 (dielectric)
ε_M
(metal)
$\varepsilon_M = -2\mathrm{Re}\,(\varepsilon_0)$
absorption
Surface plasmon
resonance
Energy

Surface plasmon resonance

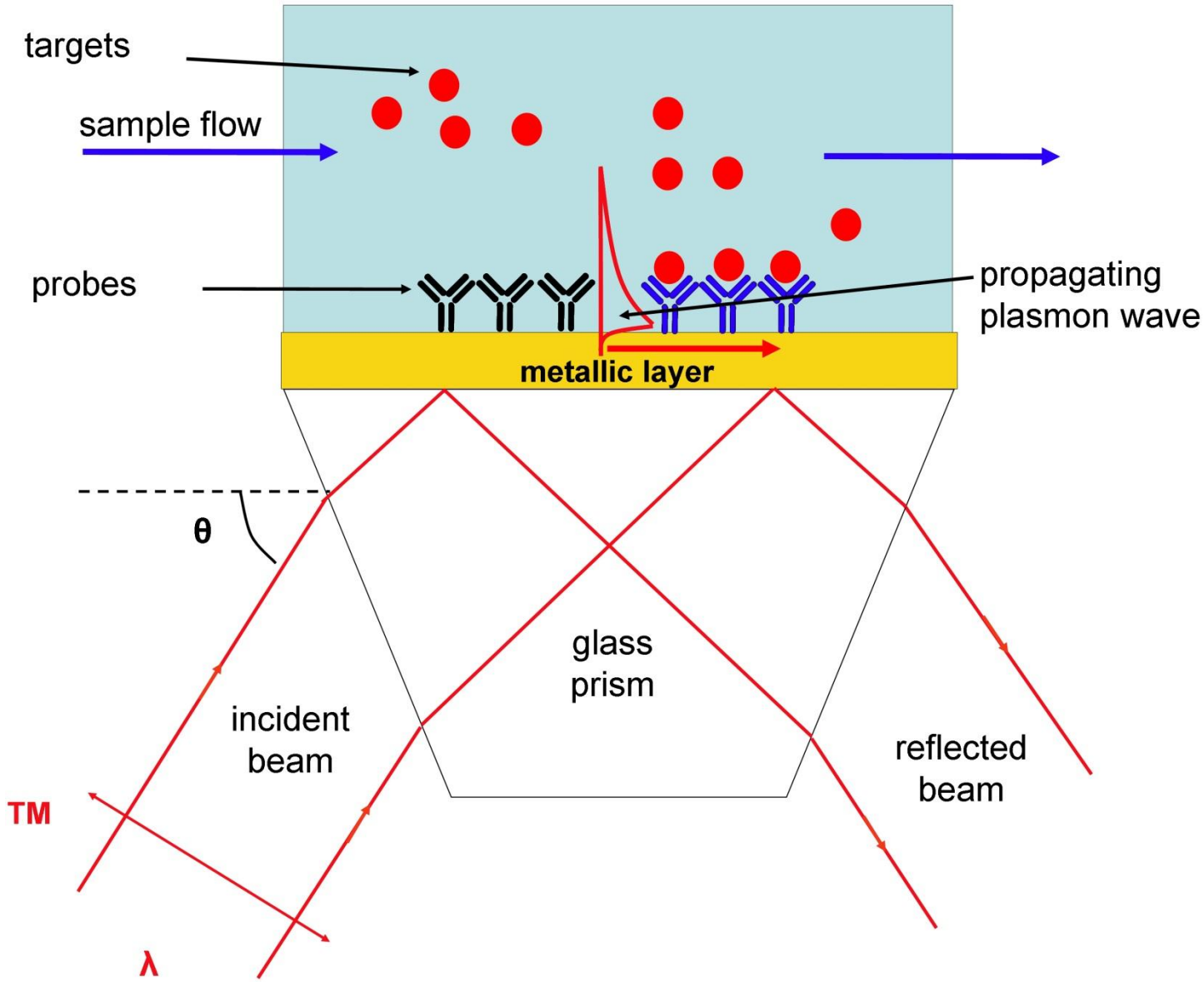

Phonons

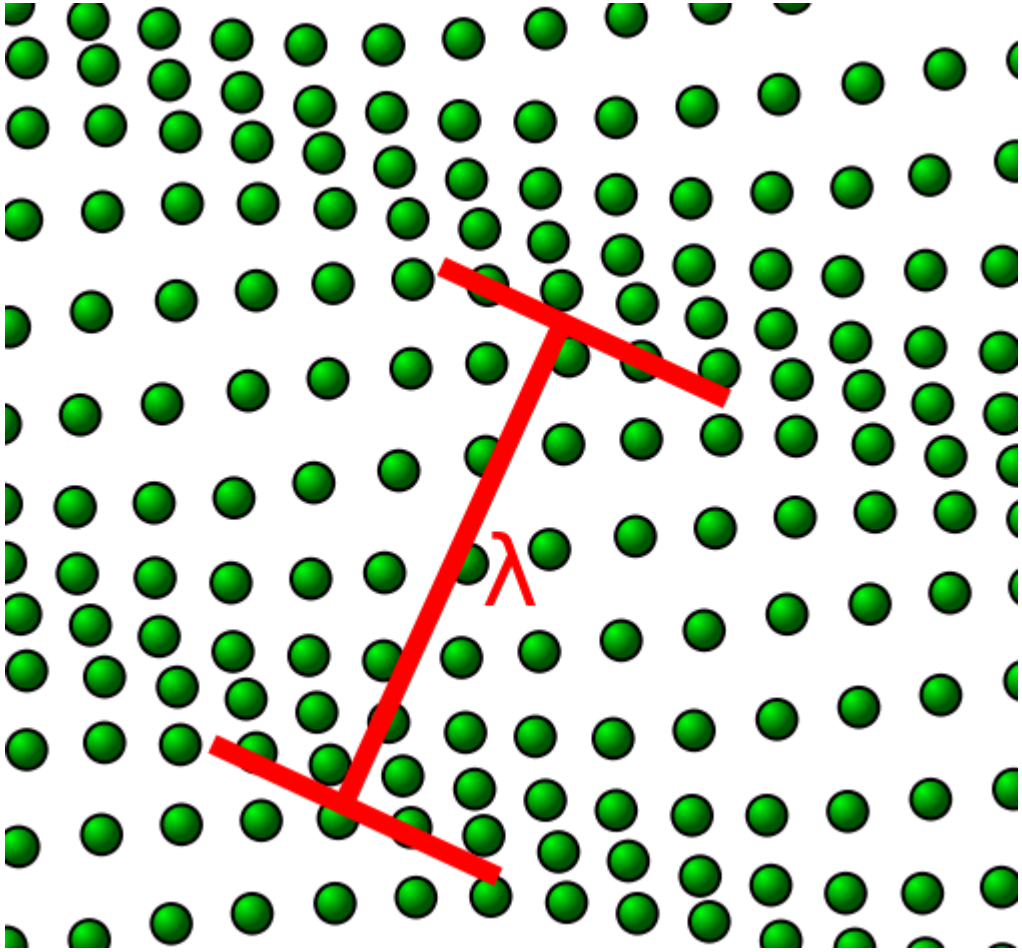

Wavevectors of phonons outside 1BZ are meaningless

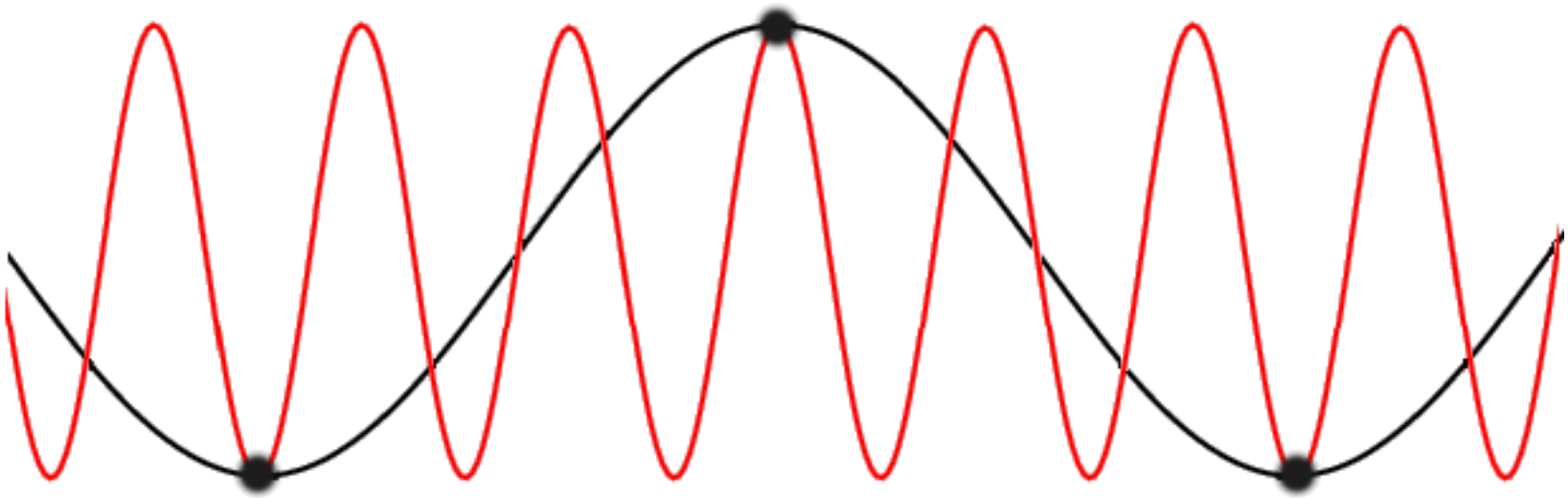

Java Phonon Applet

Transverse Optical and Acoustic Phonon Dispersion

In the graph below, we have calculated the energy of the phonon traveling perpendicular to the lattice planes for a solid with a two-atom basis (like salt).
The vertical green line indicates the atom separation divided by phonon wavelength. Move the bottom slide bar at the right to change the wavelength. Move the top slide bar to vary the relative masses of the atoms.

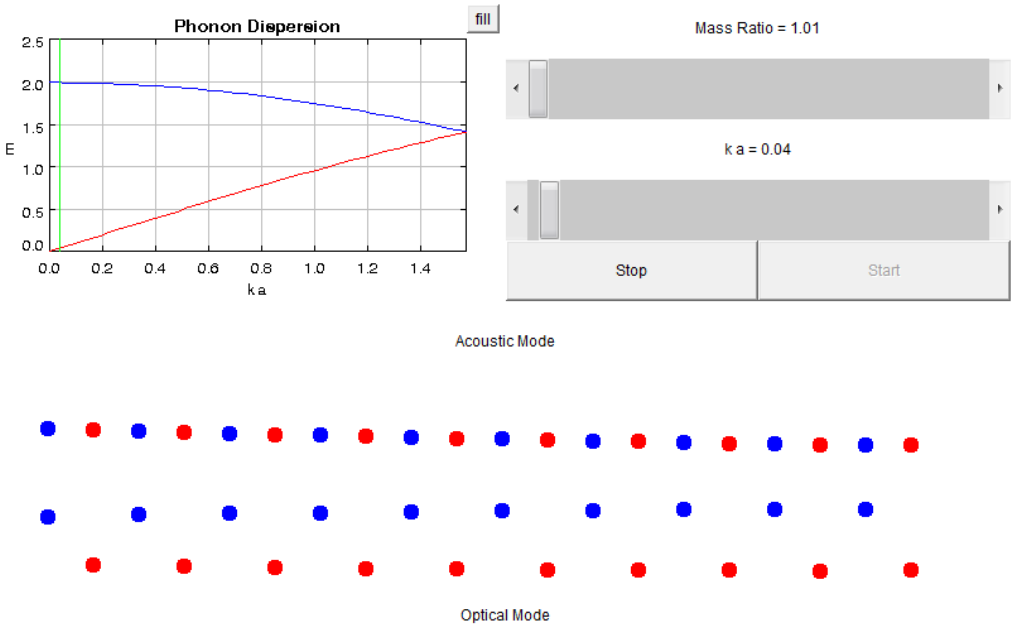

This Applet developed by Michael A. Lee and Kevin E. Schmidt.

Last modified April 13, 2000.

Phonon dispersion of Si (fcc)

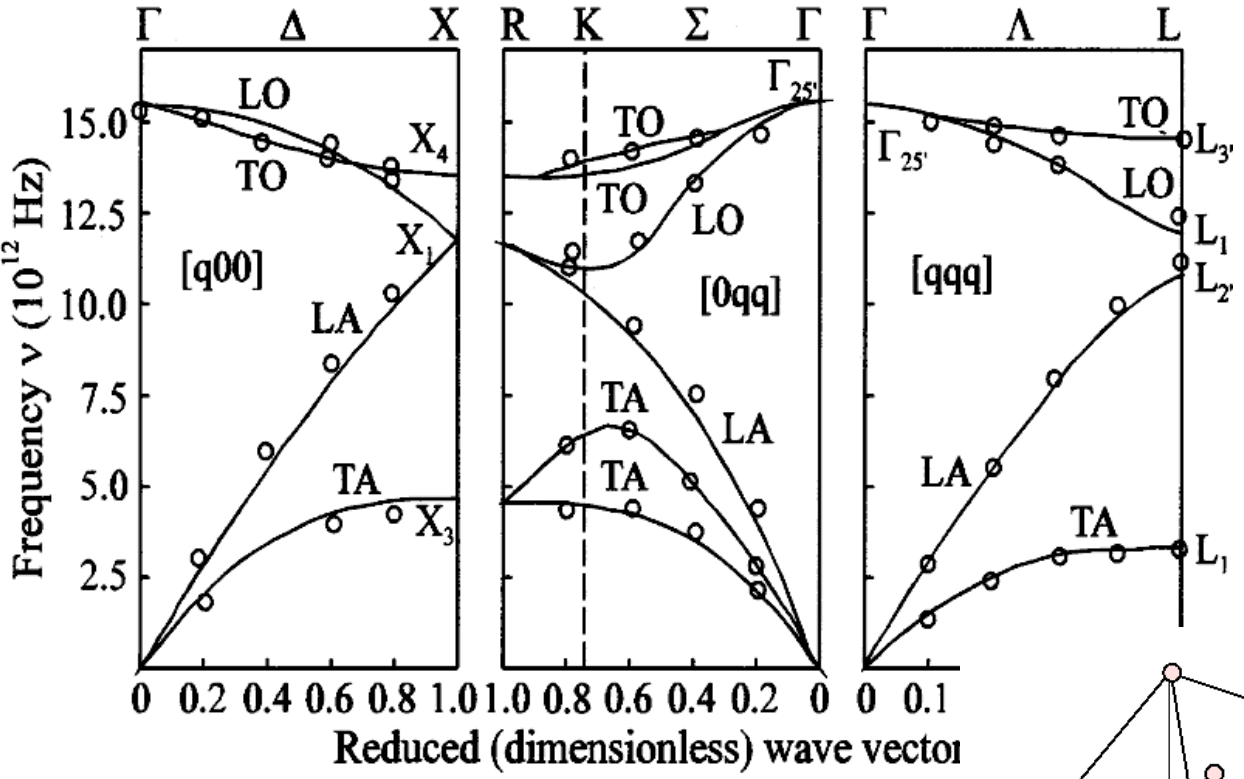

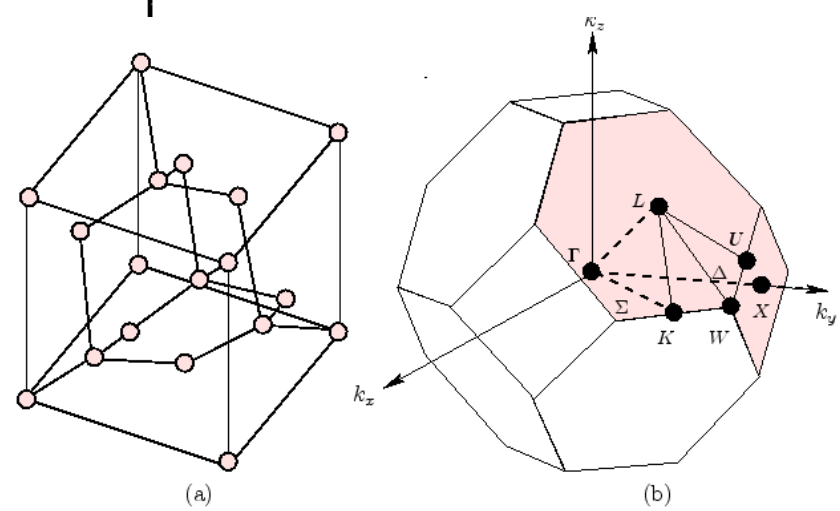

Figure 3.4: (a) Structure of the fcc Si crystal lattice.(b) Brillouin zone of a fcc lattice with the notation for special symmetry direction and points.

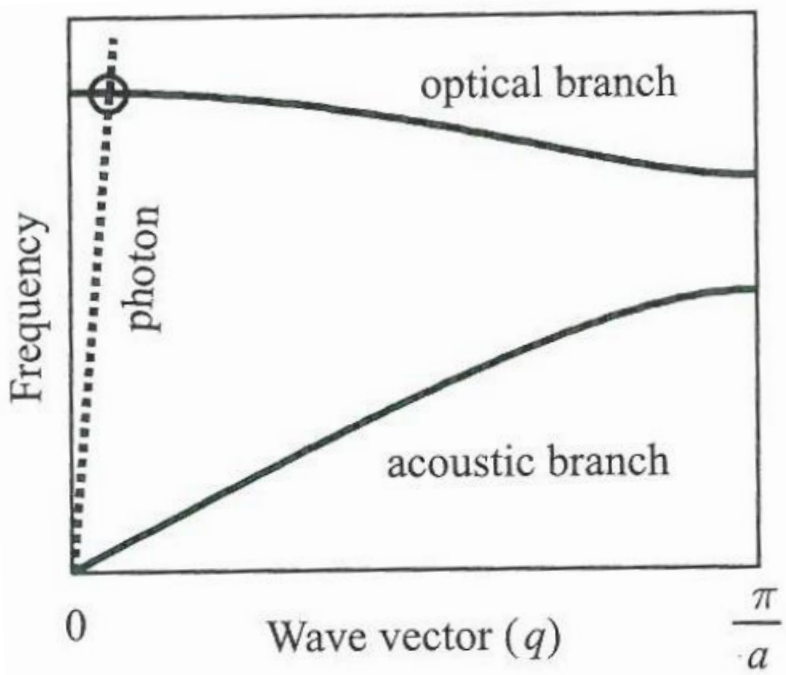

Fig. 10.2 Dispersion curves for the acoustic and optical phonon branches in a typical crystal with a lattice constant of a. The dispersion of the photon modes in the crystal is shown by the dotted line.

Wechselwirkung und Streugesetze

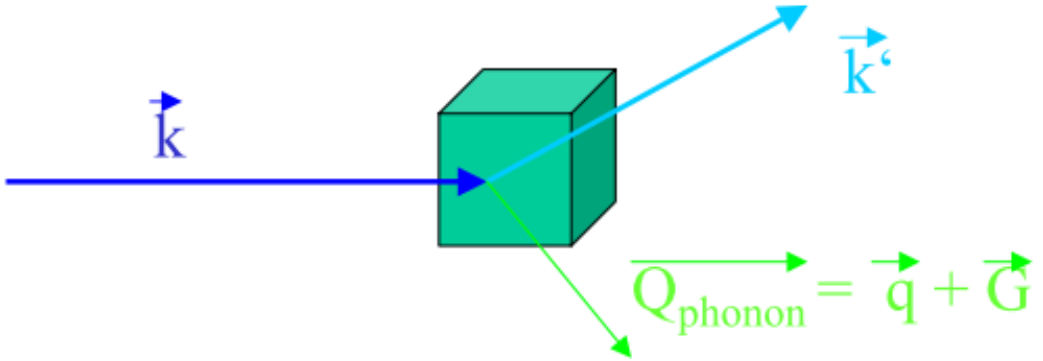

Streudreieck:

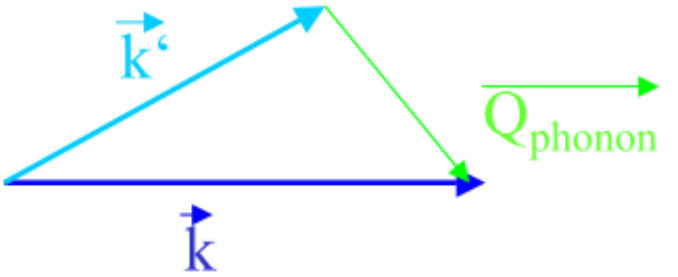

$$\text{Impuls}: \quad \vec{Q} = \vec{k} - \vec{k}'$$

$$E = \frac{\hbar^2 \cdot k^2}{2 \cdot m}$$

$$\text{Energie}: E = E' + E_{Phonon}$$

$$E_{Phonon} = \hbar \cdot \omega = \frac{\hbar^2}{2 \cdot m} \cdot (k^2 - k'^2)$$

$$\text{Spin}: \text{Gesamt-Spin vorher und nachher}$$

Nobel price in physics 1930 " for his work on the scattering of light and for the discovery of the effect named after him"

Raman spectrometer

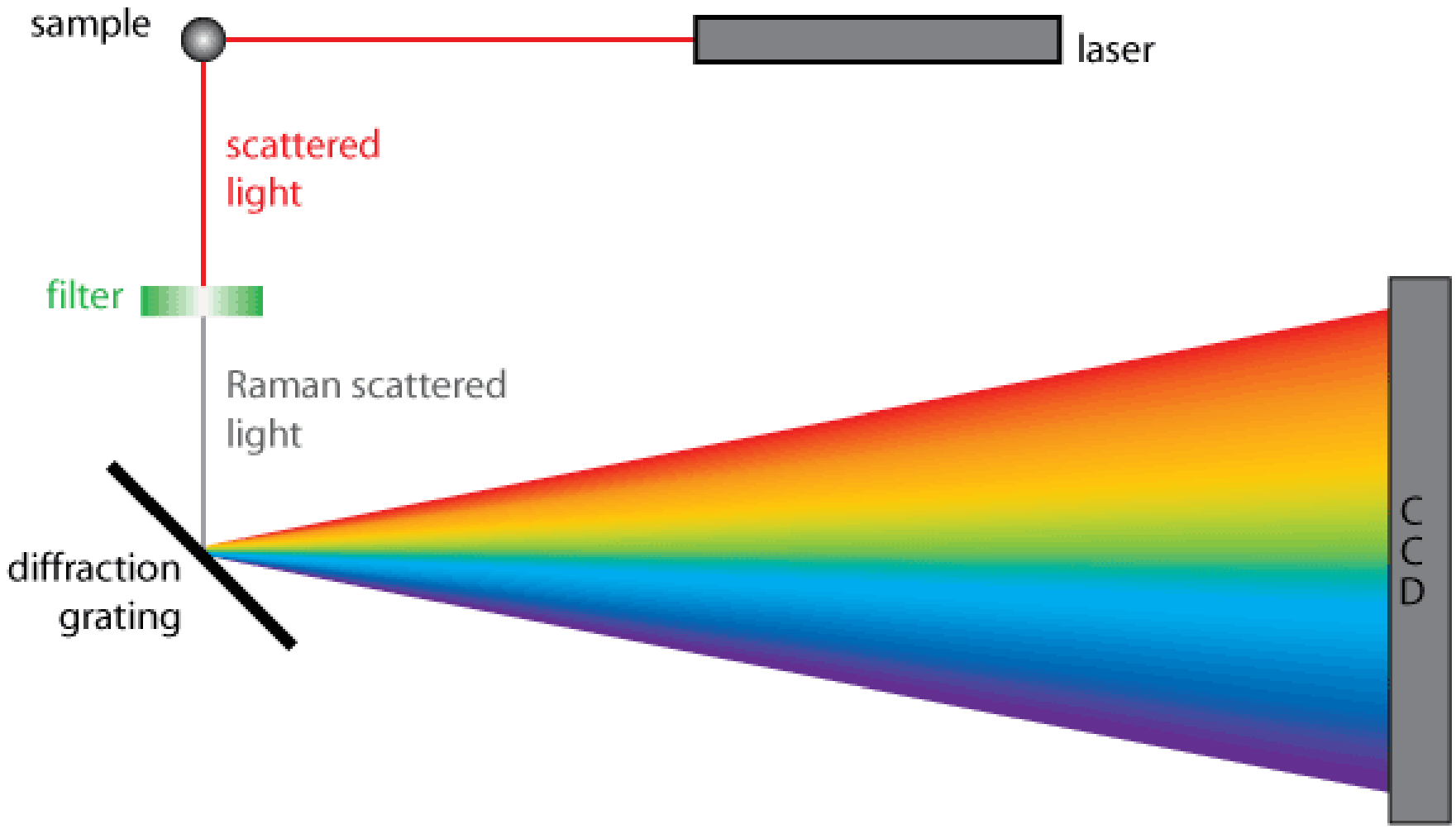

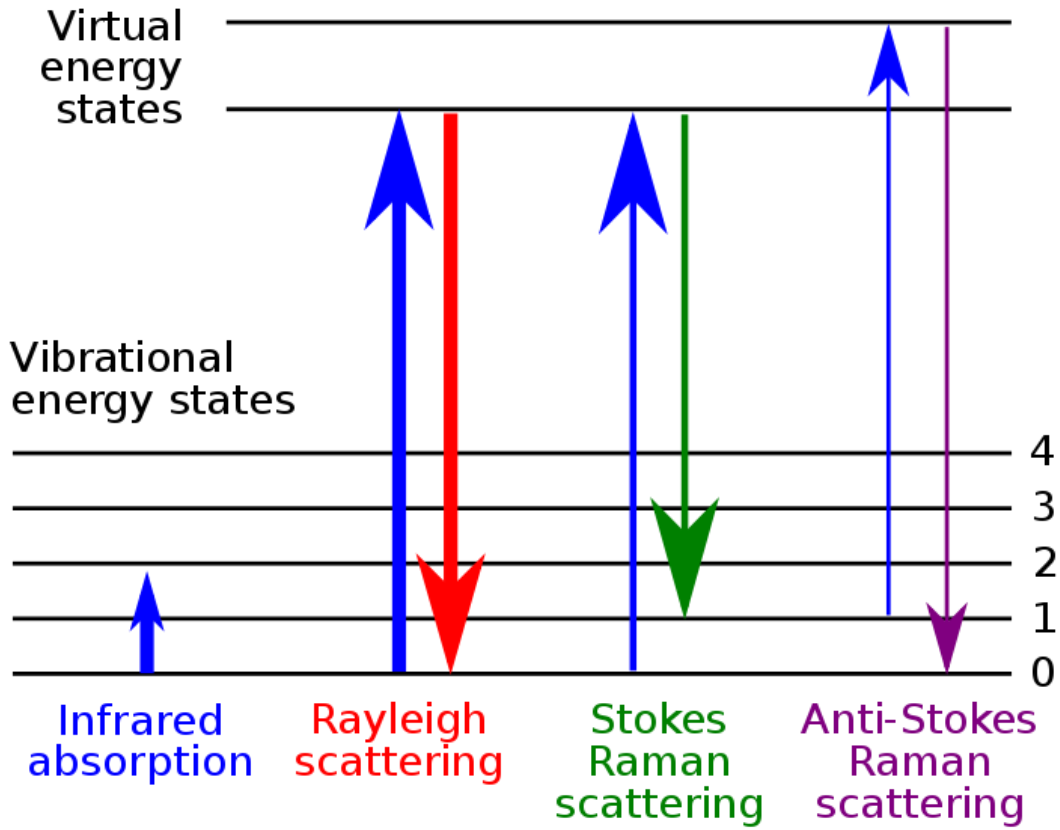
Virtual energy states
Vibrational energy states
4
3
2
1
0
Infrared absorption
Rayleigh scattering
Stokes Raman scattering
Anti-Stokes Raman scattering

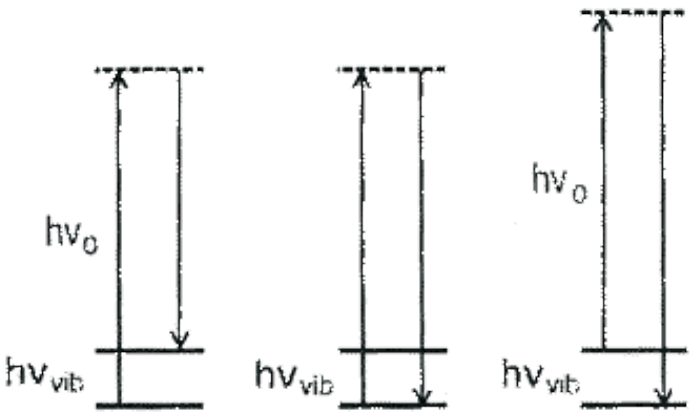
hν0
hνvib
hν0
hνvib
hν0
hνvib

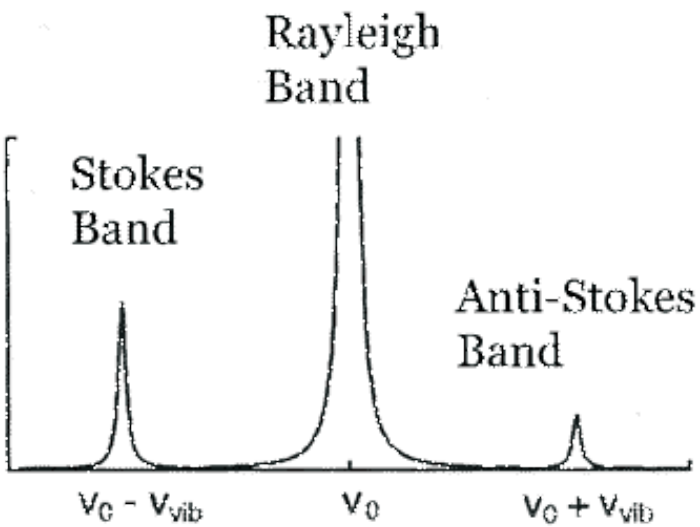
Rayleigh Band
Stokes Band
Anti-Stokes Band
ν0 - νvib
ν0
ν0 + νvib

Stokes / Anti-Stokes

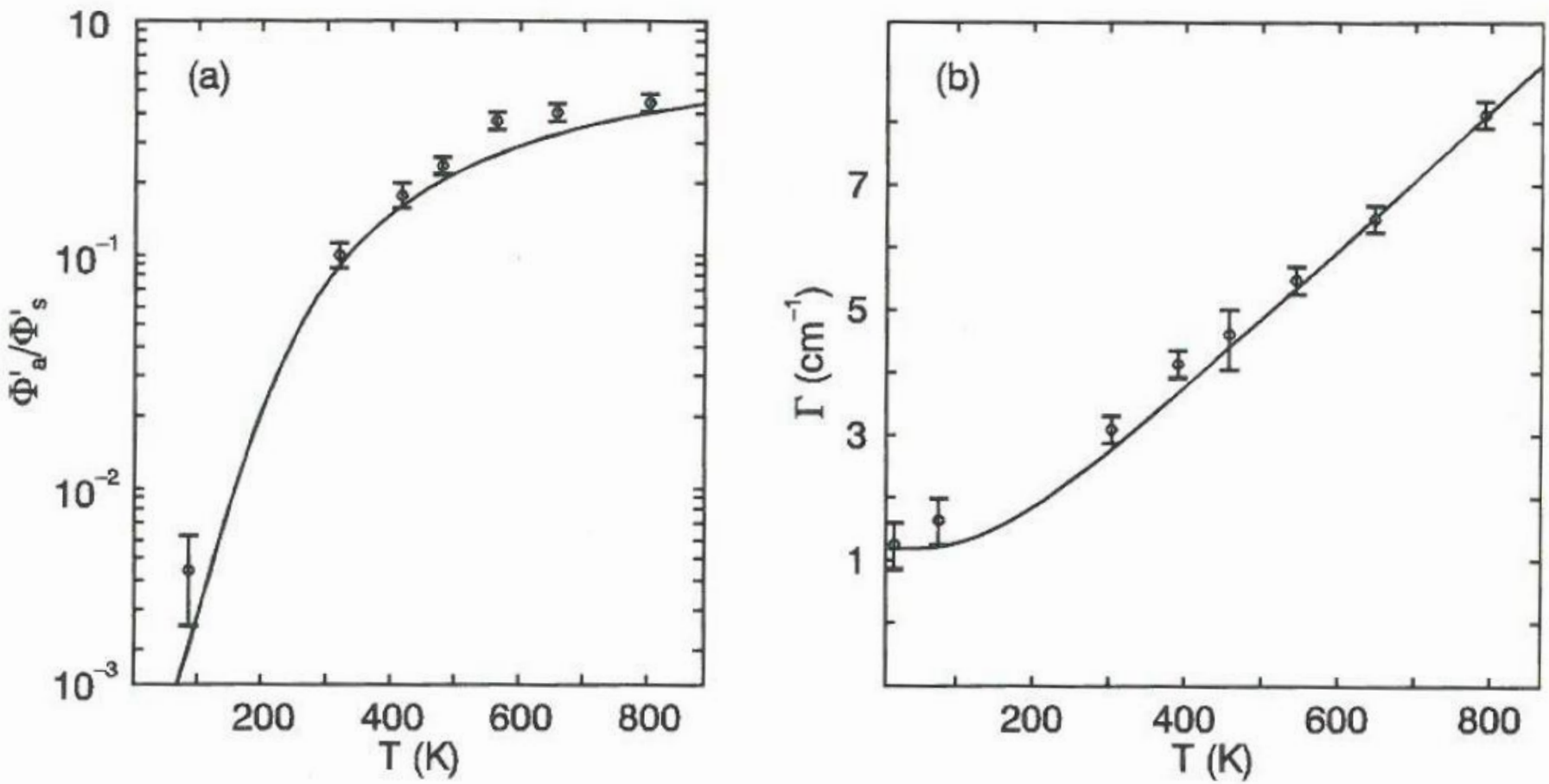

Fig. 9.12. Ratio of antiStokes to Stokes Raman intensities for Si versus temperature; (•): experiment, (—): calculated from (9.34) (**a**), and width of the Raman line in Si versus temperature; (•): experiment, (—): calculated (**b**); after [9.5].

Raman spectrum of GaAs

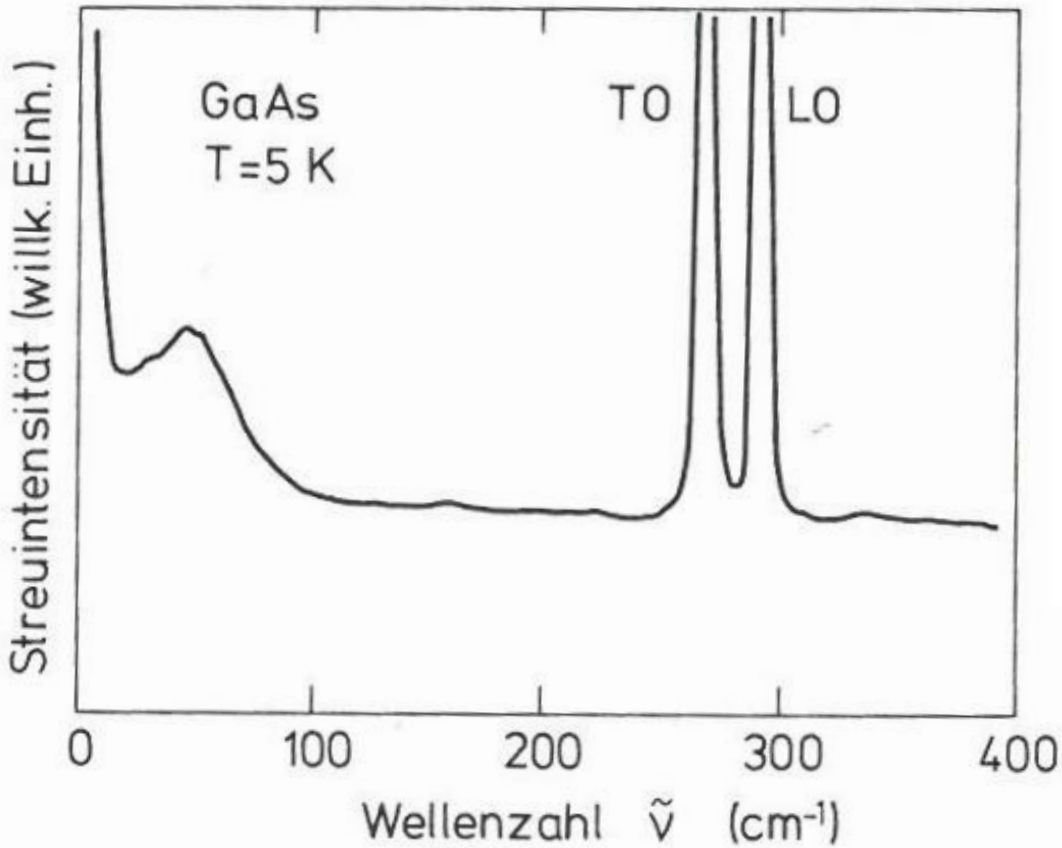

Abb. III.3. Raman-Spektrum, aufgenommen an *n*-dotiertem GaAs bei 5 K Probentemperatur (Konzentration freier Elektronen $n \approx 10^{16}\,\mathrm{cm}^{-3}$); TO und LO bezeichnen transversal bzw. longitudinal optische Phononen. Die Bande bei 40 cm^{-1} rührt im wesentlichen von Plasmon-Anregungen her. (Nach Mooradian [III.3])

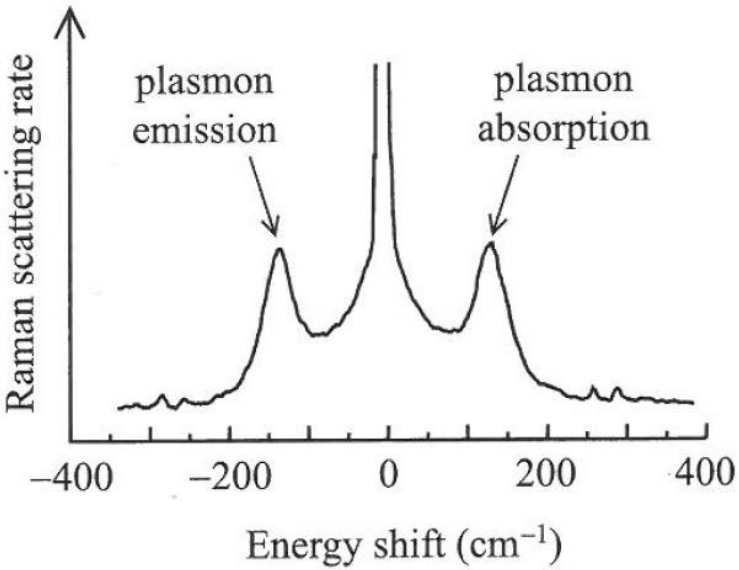

Different plasmon frequency due to different charge carrier concentration (doping)

Raman spectra of graphene

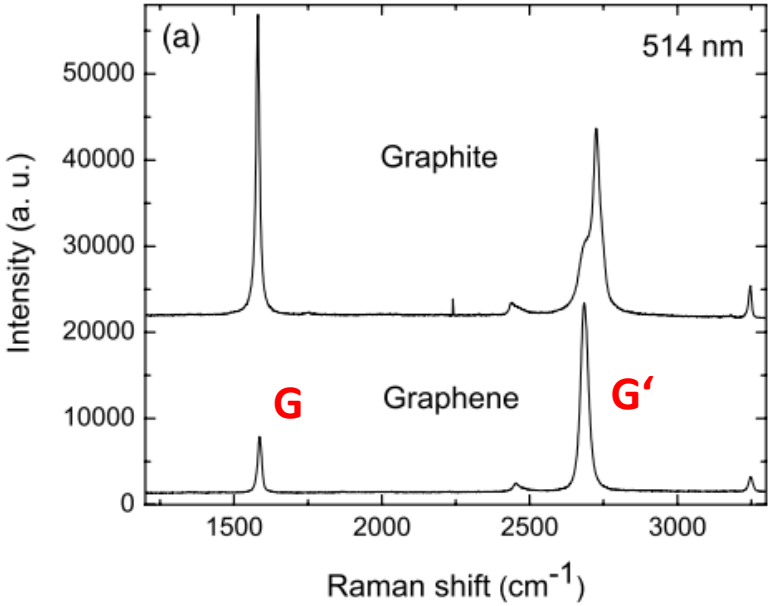

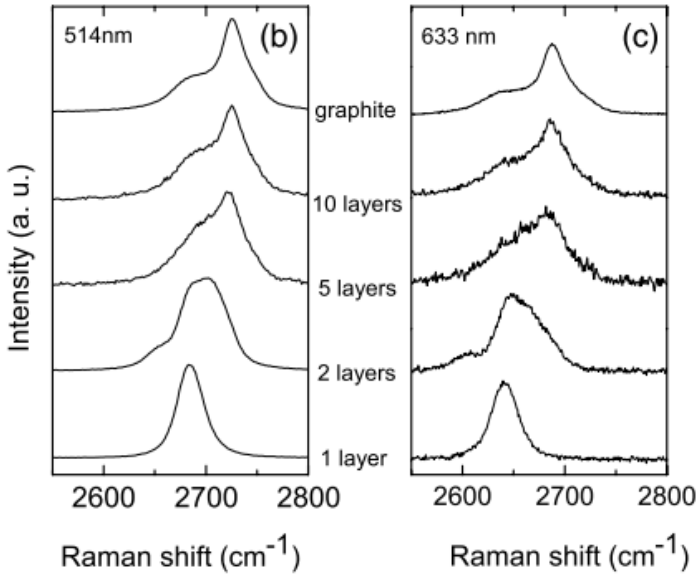

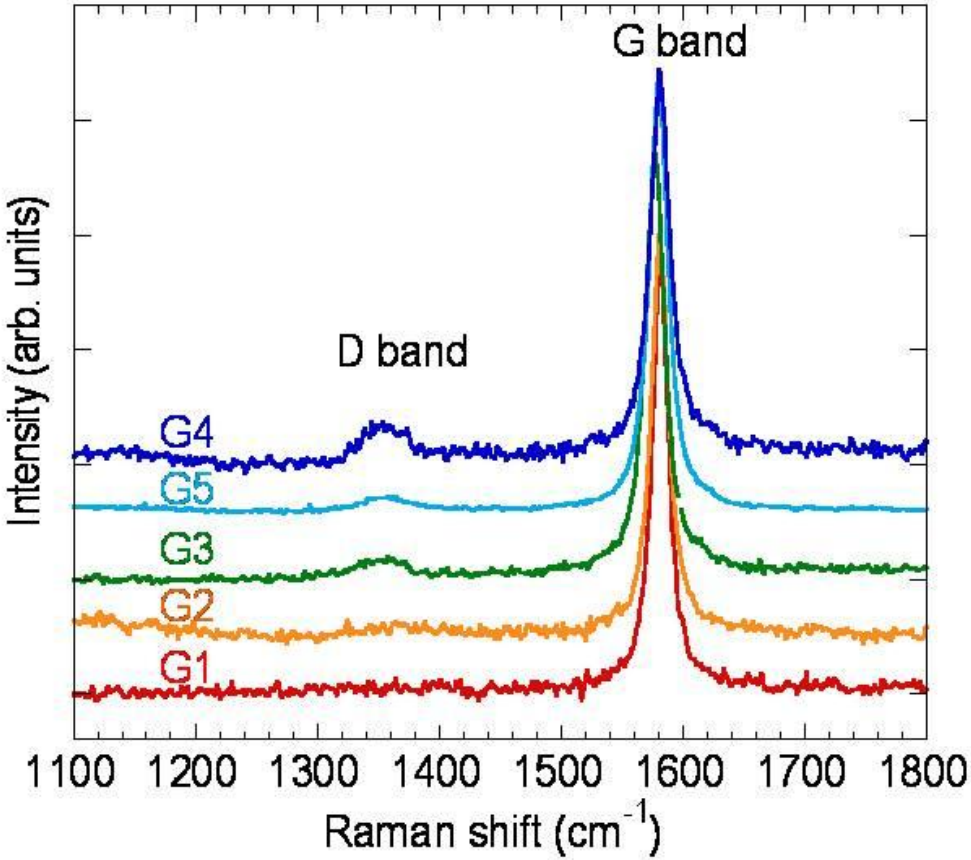

Raman microscope

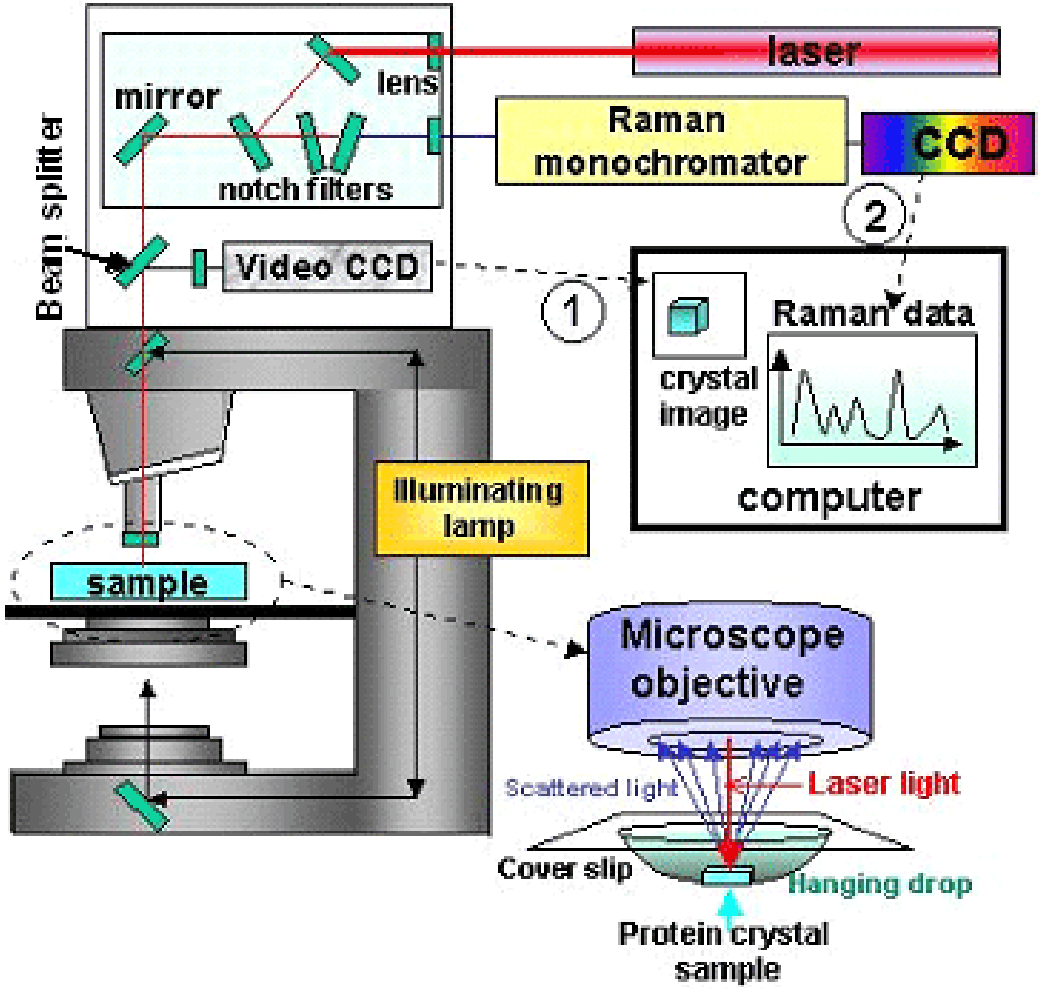

Schematic drawing of a Raman microscope (not to scale) and Raman microscopy of a single protein crystal.

Raman microscopy of graphene

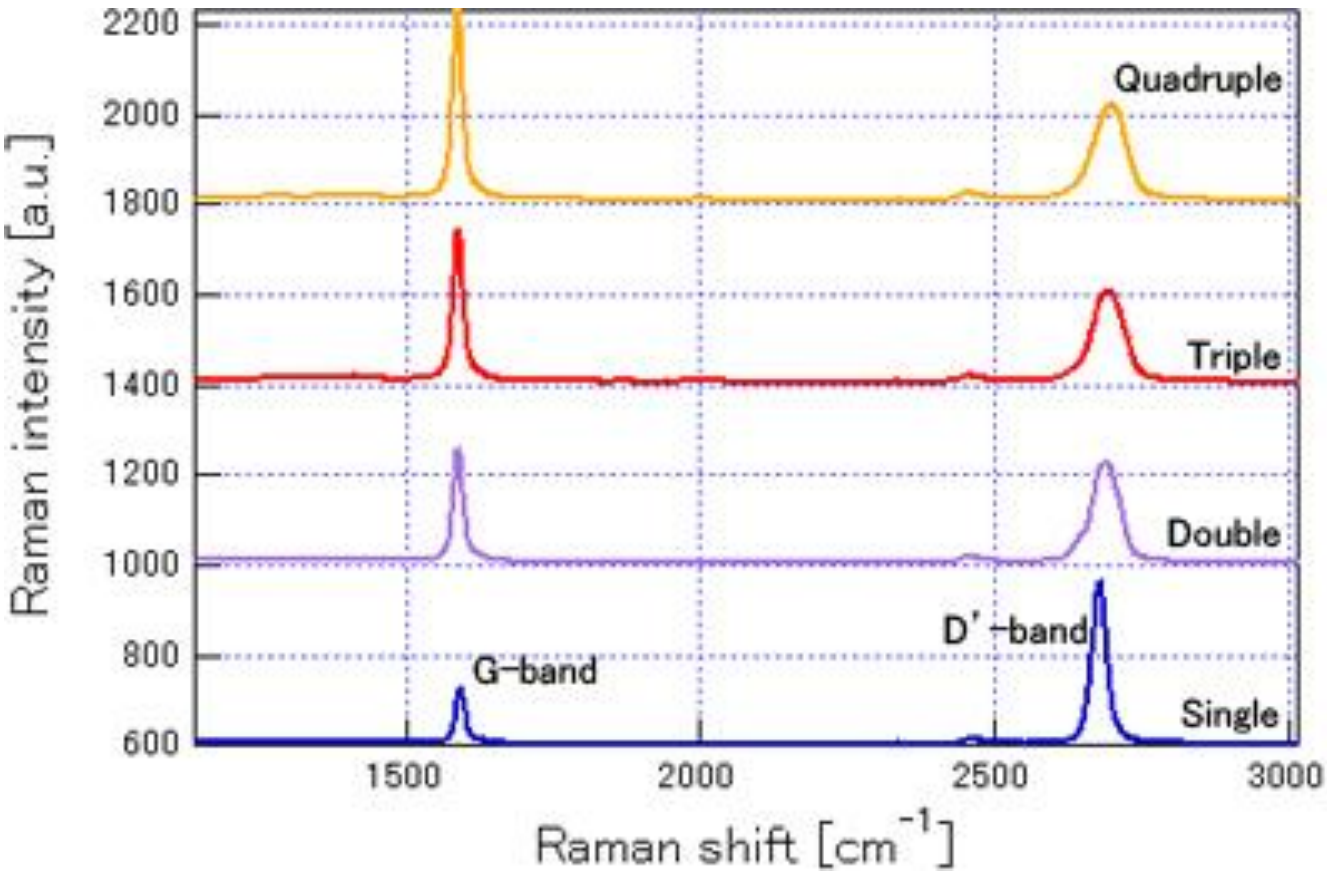

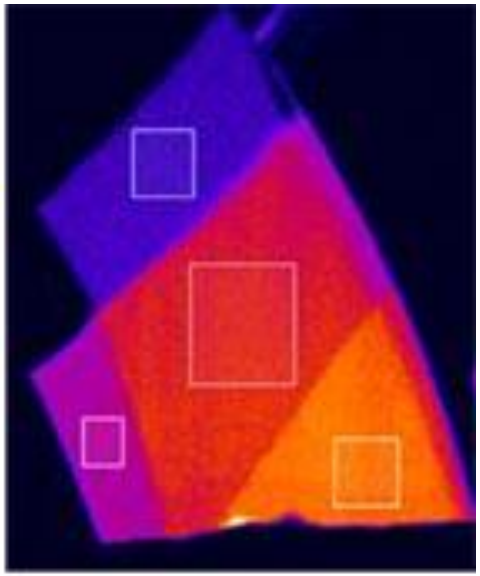

Tip enhanced raman spectroscopy (TERS)

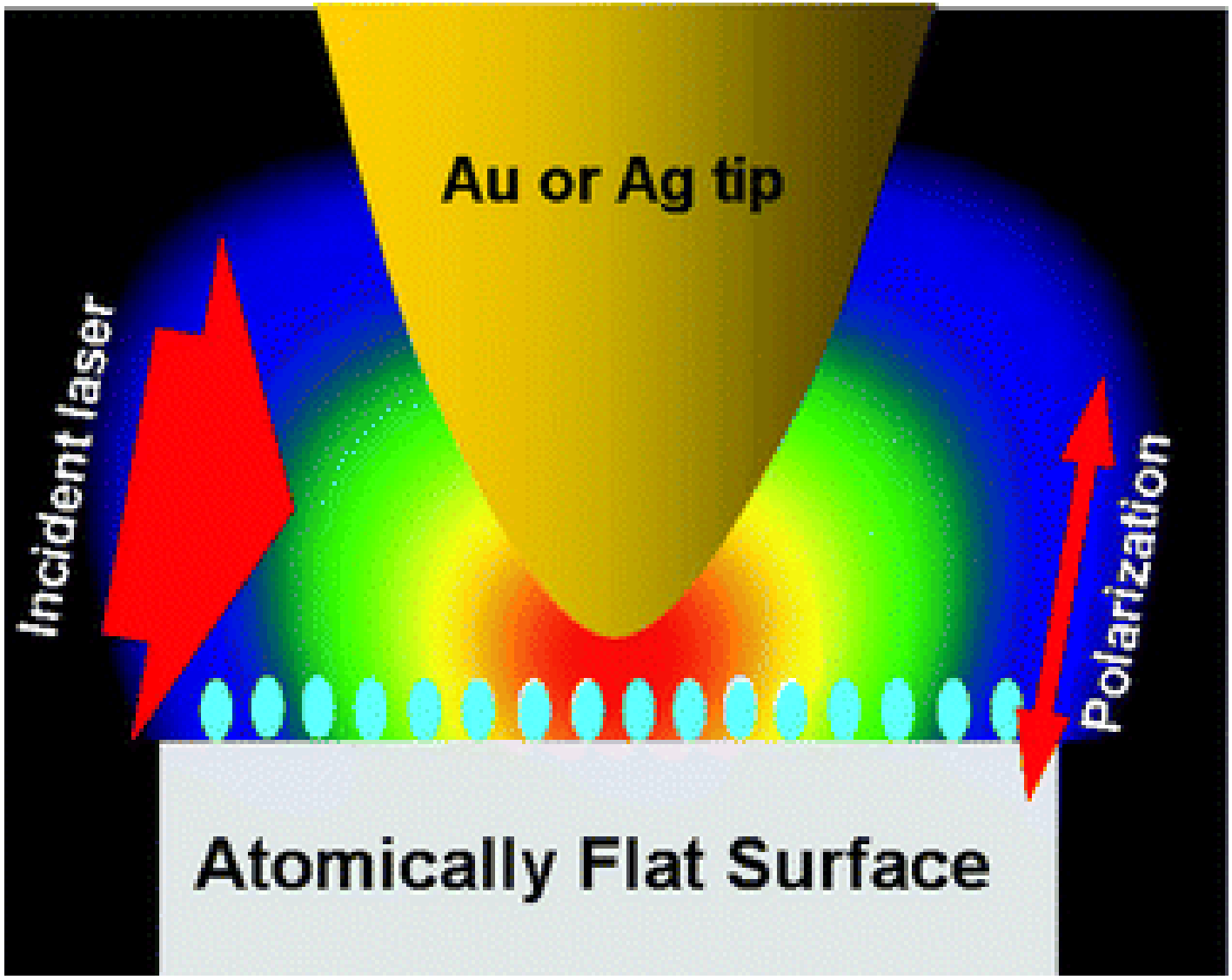

TERS - example

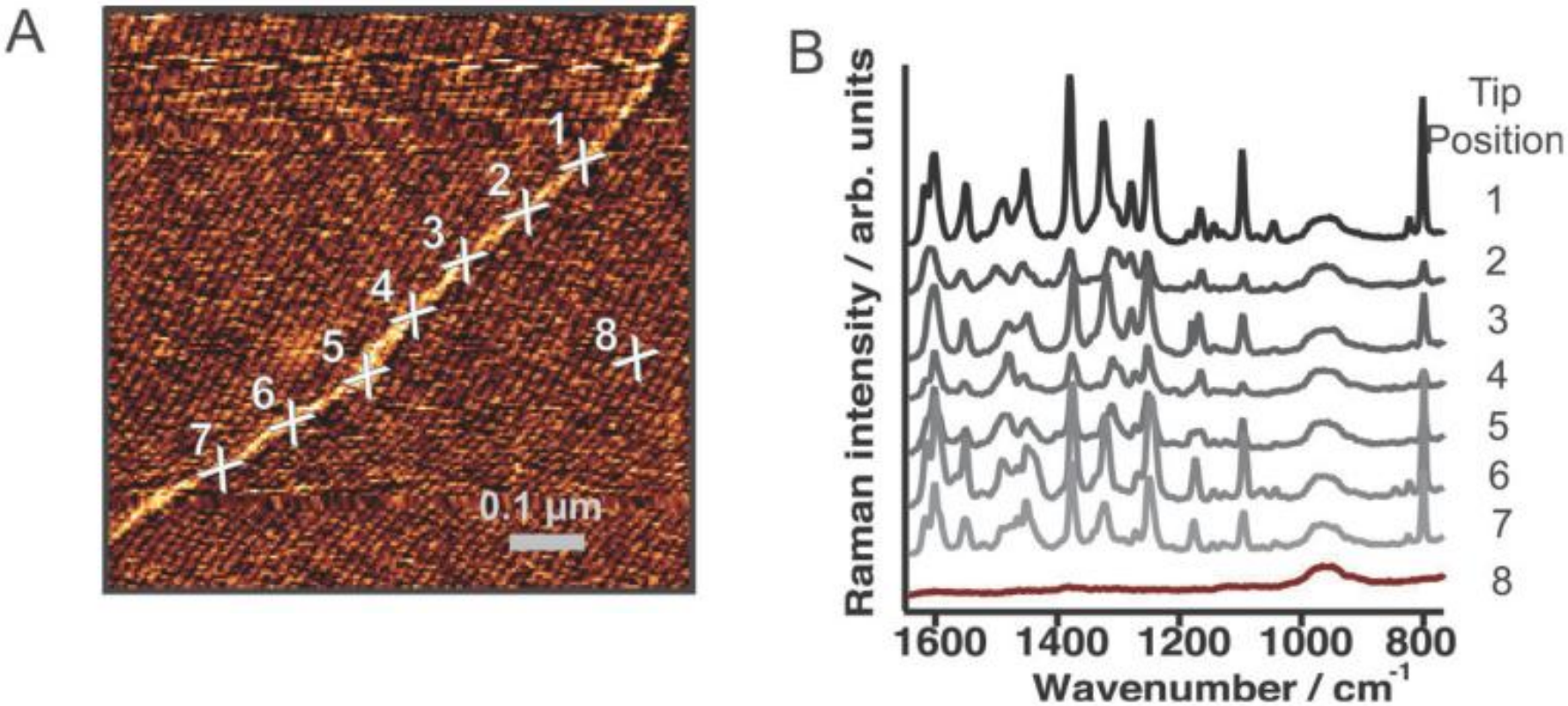

Fig. 14 TERS experiment along a RNA strand. (A) Topographic image (same as Fig. 13A). (B) TERS spectra at the seven adjacent (1–7) spots correspondingly marked in (A), position 8 marks a reference measurement. Adapted from ref. 34.

Polariton in GaP

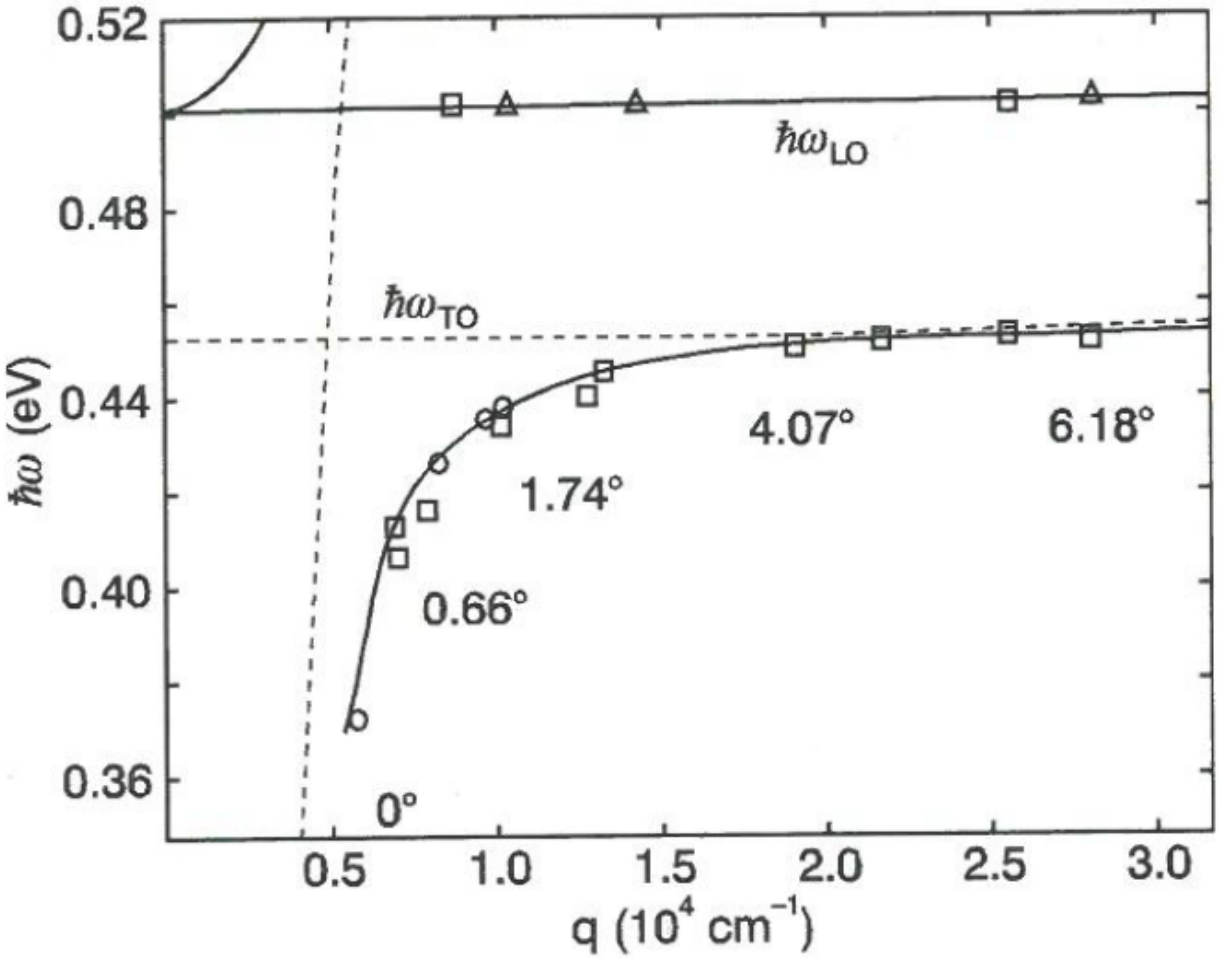

Fig. 9.10. Polariton dispersion of GaP as measured by Raman scattering in the forward direction. The dashed lines give the dispersion for the uncoupled photons and phonons. The angles indicated refer to the scattering geometry; after [9.4].

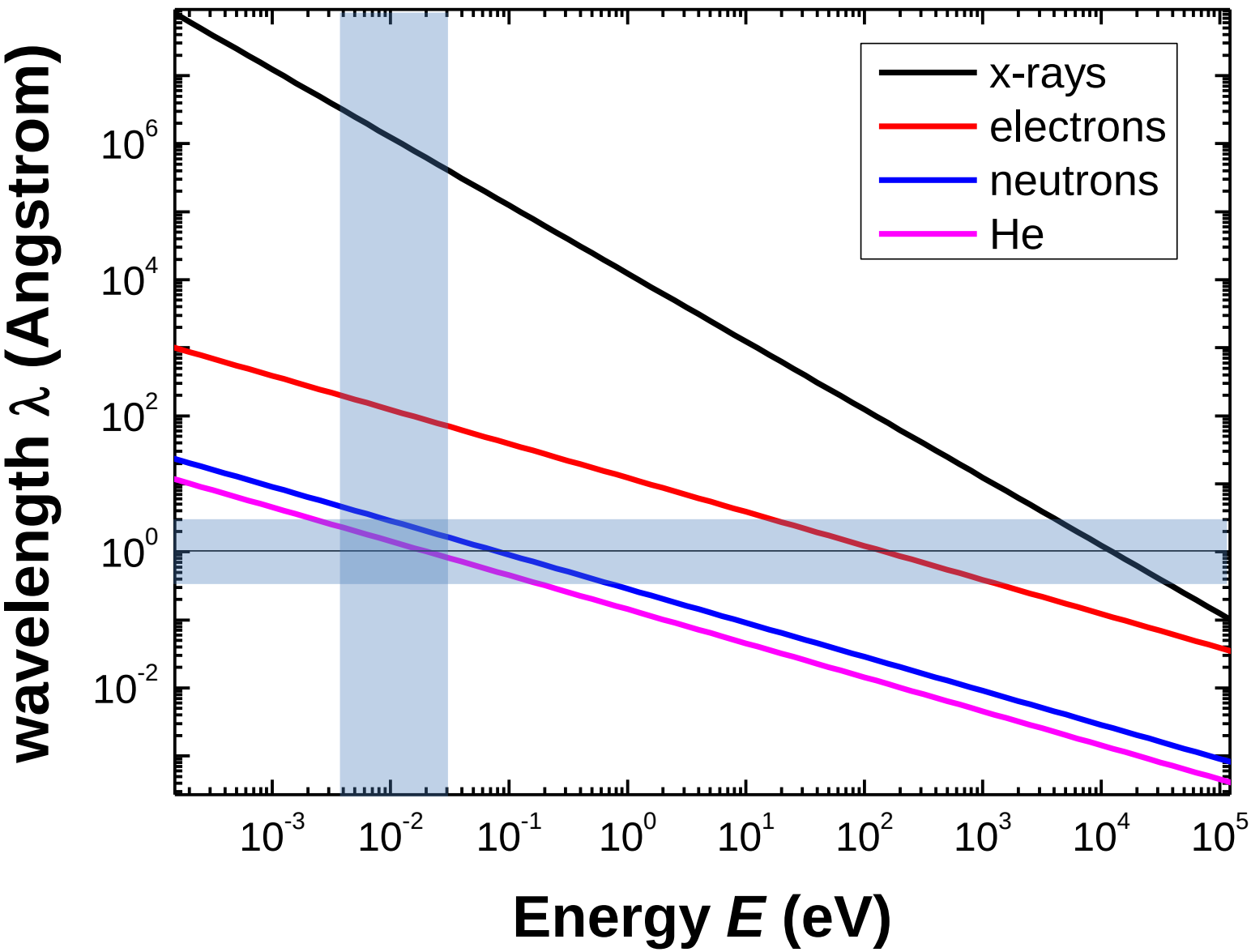
x-rays
electrons
neutrons
He
wavelength λ (Angstrom)
Energy E (eV)
10^6
10^4
10^2
10^0
10^-2
10^-3
10^-2
10^-1
10^0
10^1
10^2
10^3
10^4
10^5

Three axis spectroscopy

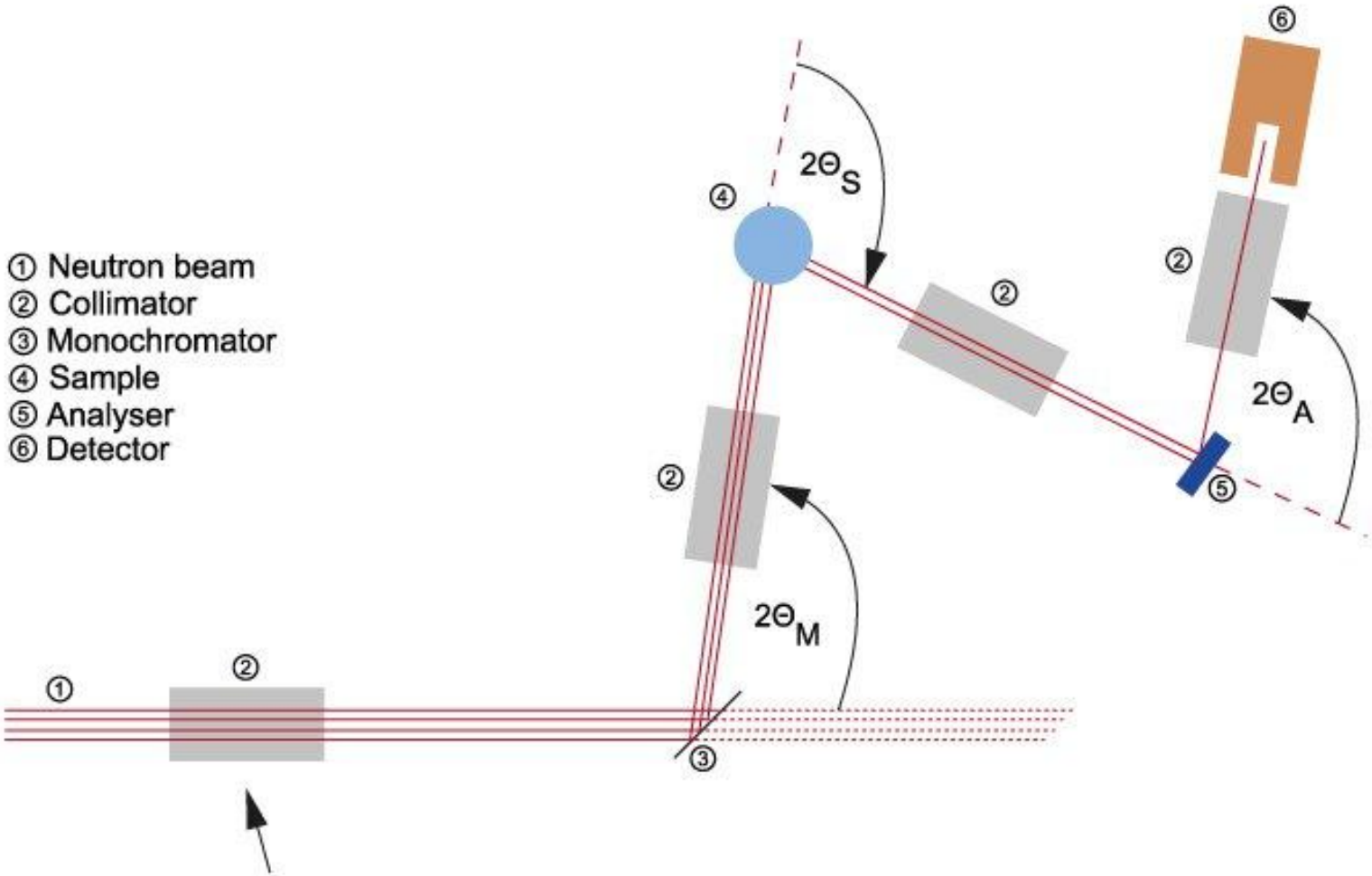

Inelastic neutron scattering

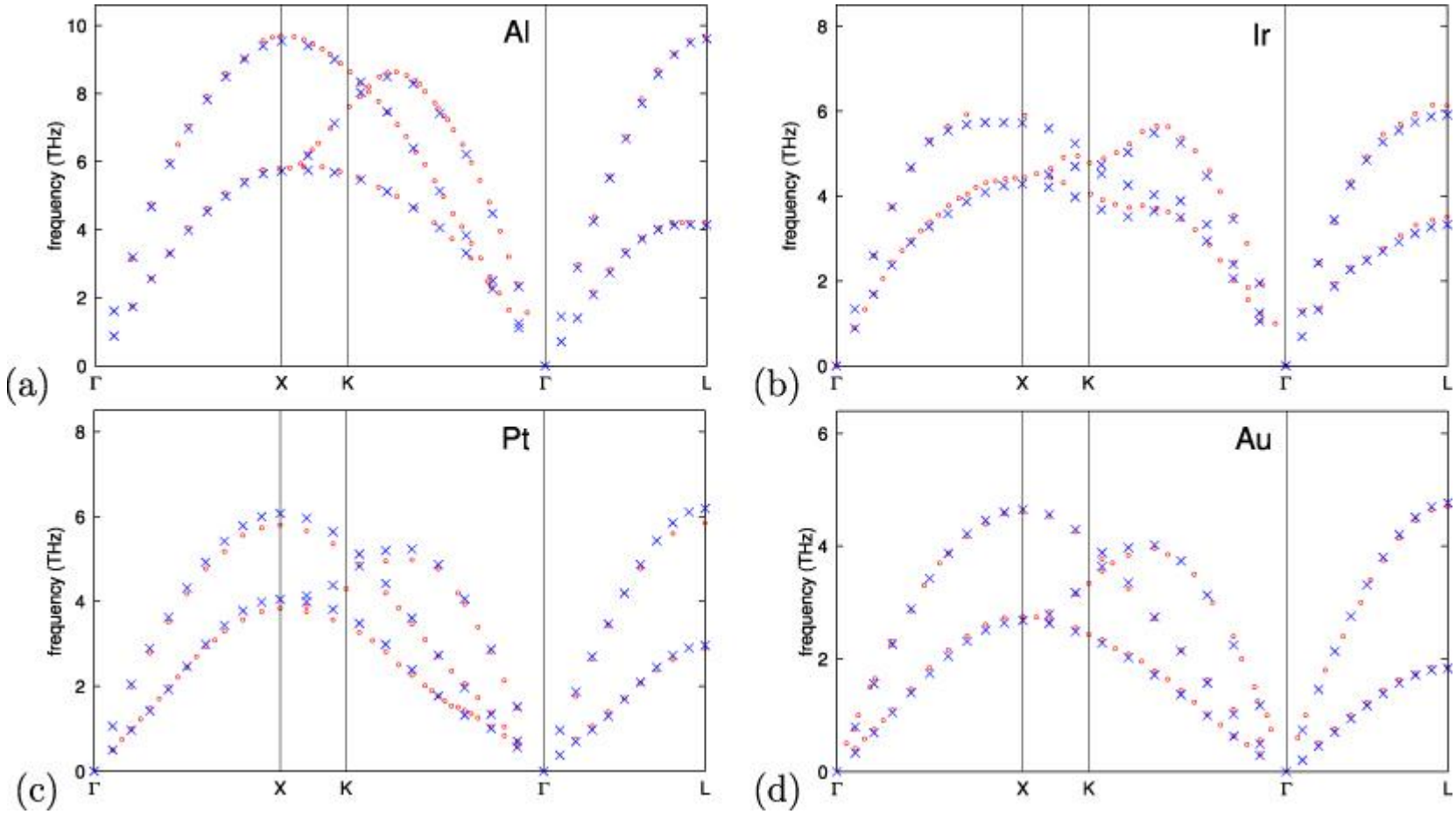

o: experiment
x: theory

Pavol Krivosik

Spin Wave Basics

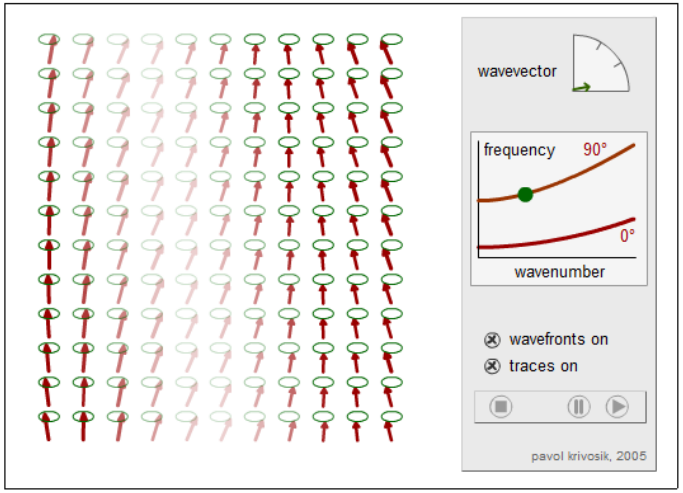

Spin wave is a propagating, wave-like excitation of magnetic moments in a magnetic sample. This animation illustrates the basic concept of this phenomena in an infinite isotropic medium. For a brief introduction and theoretical background see "Magnetic excitations in solids," C. E. Patton, Phys. Rep. 103, 251 (1984), Section 2.1.

Due to various interactions between magnetic moments, the frequency of their precession in an external magnetic field depends on the wavevector of the spin wave. This dependence is called a *spin wave dispersion*. In this example, all moments (dark red arrows) are initially aligned along the magnetic field direction that points "up".

Start animation with a "play" button. Yo can pause ( ) or stop ( ) animation at any time. You can now change the wavevector of the propagating wave by dragging a dark green arrow in the circular sector labeled "wavevector". You can see wavefronts that propagate in the direction of the wavevector (these are nicely visible for a propagation under 45 degrees). The wavelength of the spin wave is inversely proportional to the magnitude of the wavevector (wavenumber). For a zero wavenumber the wavelength is infinite and the spin wave becomes *uniform precession*. Below the wavector sector is a sketch of the spin wave dispersion for an infinite isotropic media. Lines represents limits of the direction of the wavevector propagation with respect to the field. The bottom line represents spin waves that propagate in the direction of the field (at 0° angle). The top line corresponds to spin waves that propagate perpendicularly to the direction of the magnetic field (90°).

Spin wave

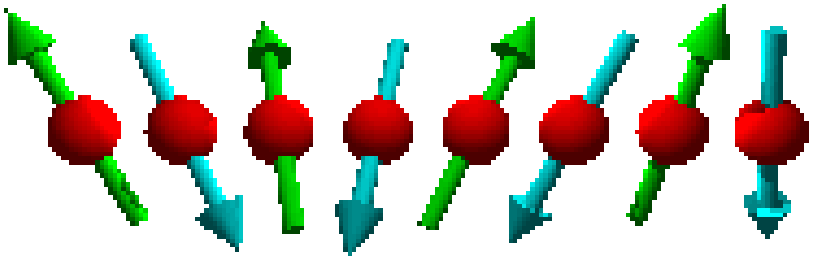

Example: Magnon in Ni

Abb. 8.13. Experimentelle Werte für die Dispersion von Spinwellen an Nickel in [111]-Richtung nach Mook und Paul [8.6]. Die Messungen erfolgten bei $T = 295$ K. Die gestrichelte Linie zeigt eine Abhängigkeit der Quantenenergie proportional zu k^2. Abweichungen davon ergeben sich infolge der Austauschwechselwirkung auch zwischen entfernteren Nachbarn und bei Eintritt in den Bereich der Einelektronenanregungen. Die verkürzte Lebensdauer der Spinwellen führt dann zu einer Lebensdauerverbreiterung der Spektren (*schraffierter Bereich*)

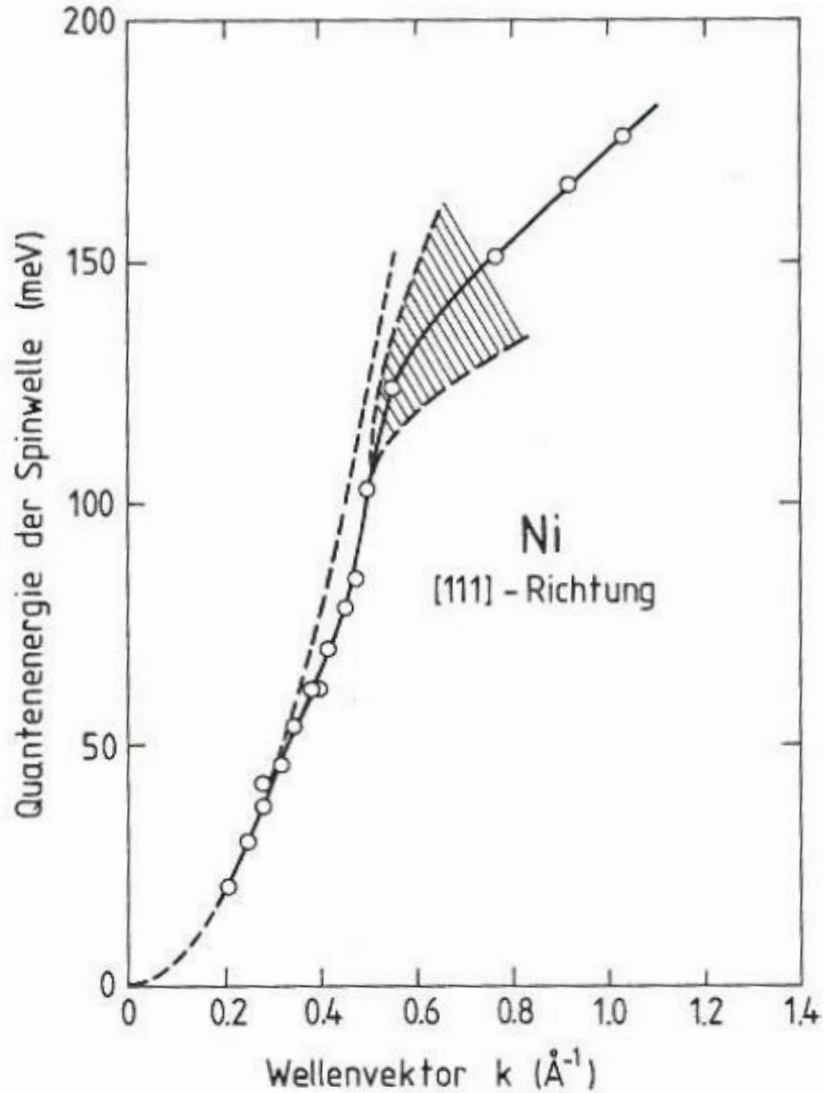

Magnon by inelastic neutrons: α-$MnMoO_4$

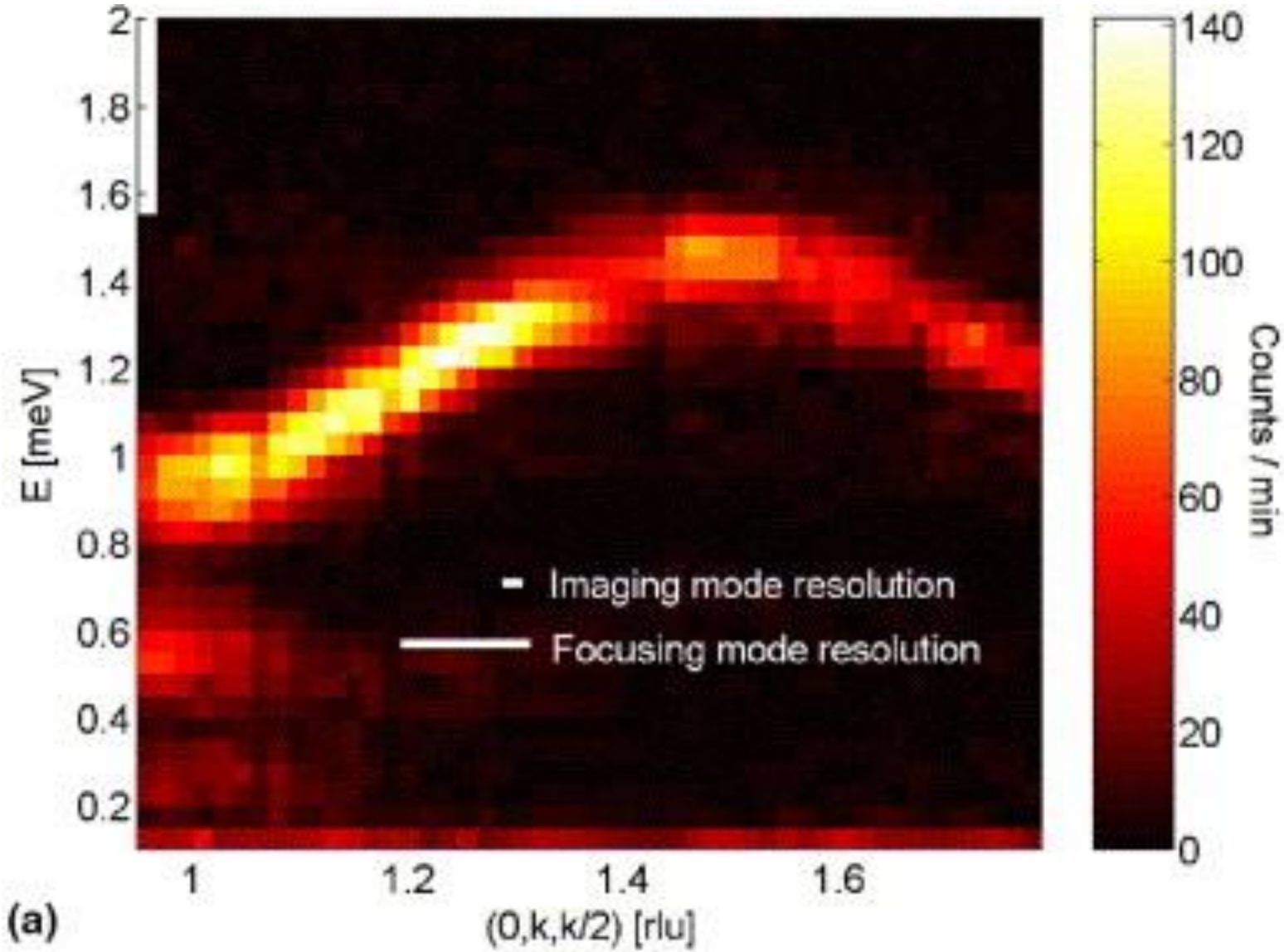

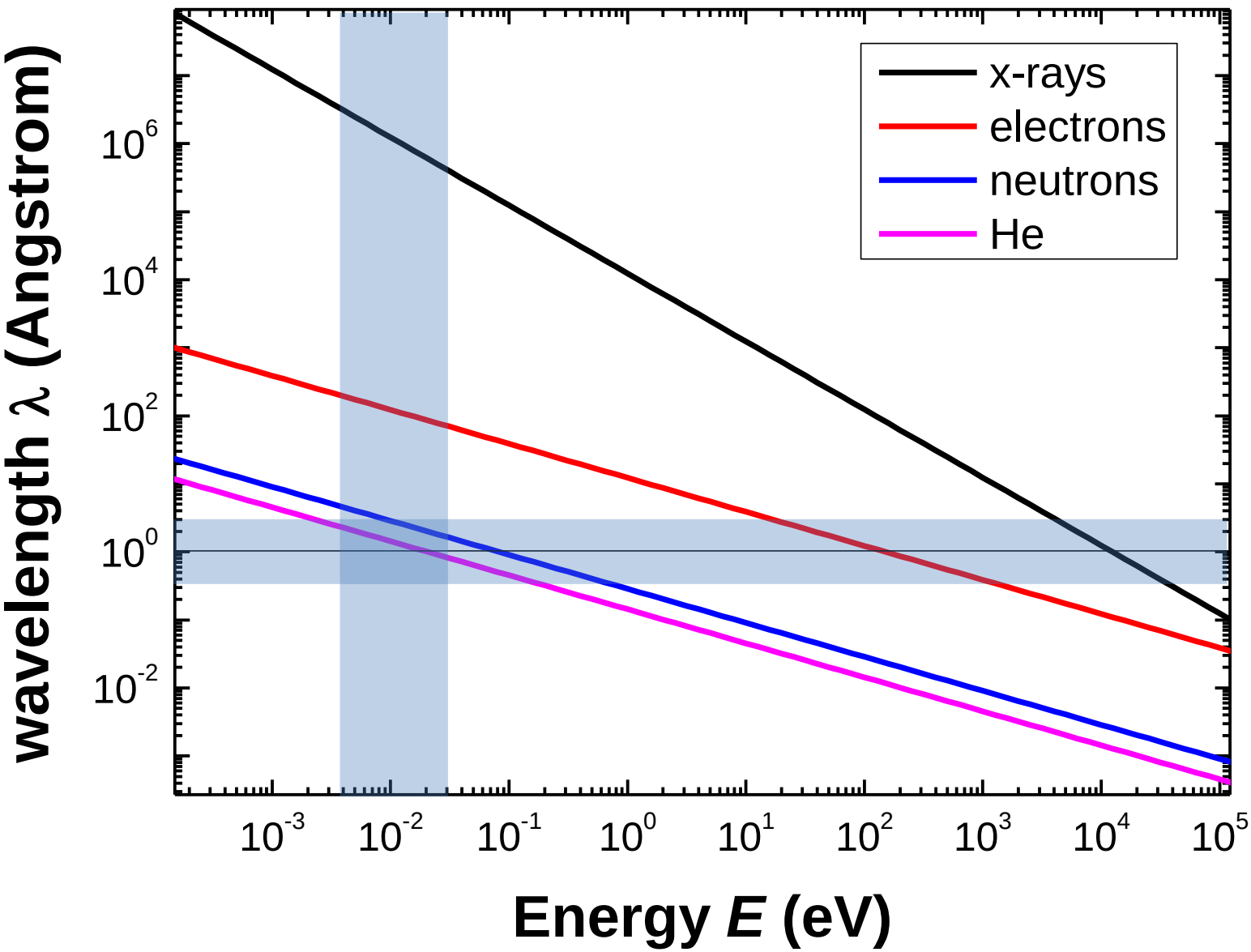
x-rays
electrons
neutrons
He
wavelength λ (Angstrom)
Energy E (eV)
10^6
10^4
10^2
10^0
10^-2
10^-3
10^-2
10^-1
10^0
10^1
10^2
10^3
10^4
10^5

Electron energy loss spectroscopy

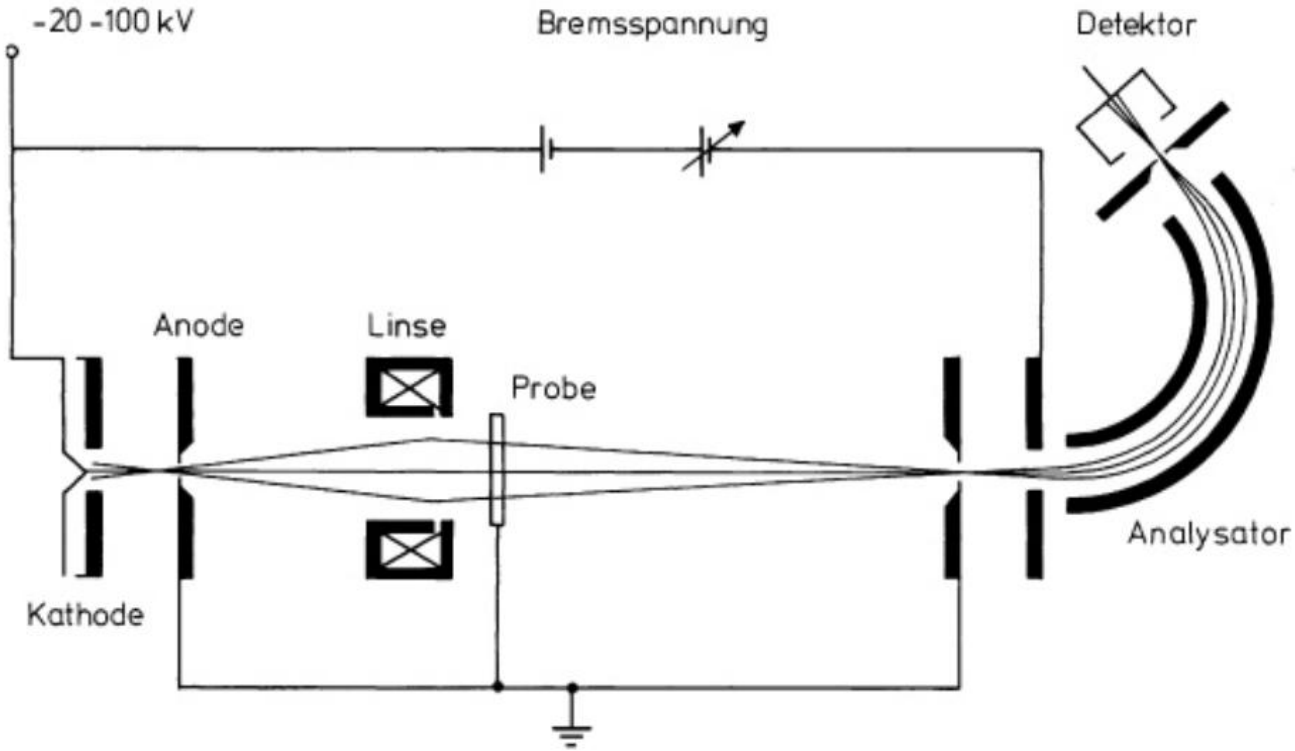

Abb. XI.2. Elektronenspektrometer für die Transmissionsspektroskopie. (Nach Raether [XI.4])

EELS - example

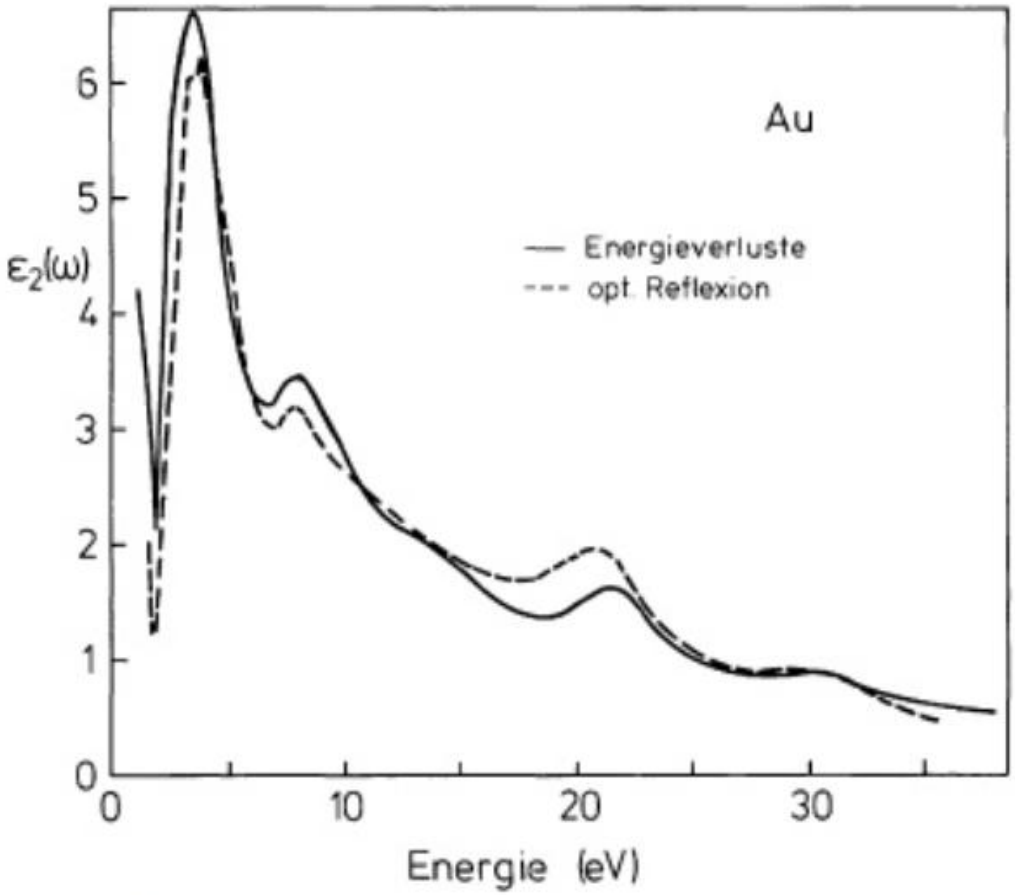

Abb. XI.3. Vergleich von $\varepsilon_2(\omega)$ für Gold aus Elektronenspektroskopie (*ausgezogene Linie*) und aus Messungen des optischen Reflexionsvermögens. (Nach Daniels et al. [XI.5])

EELS on Si(111) 7x7

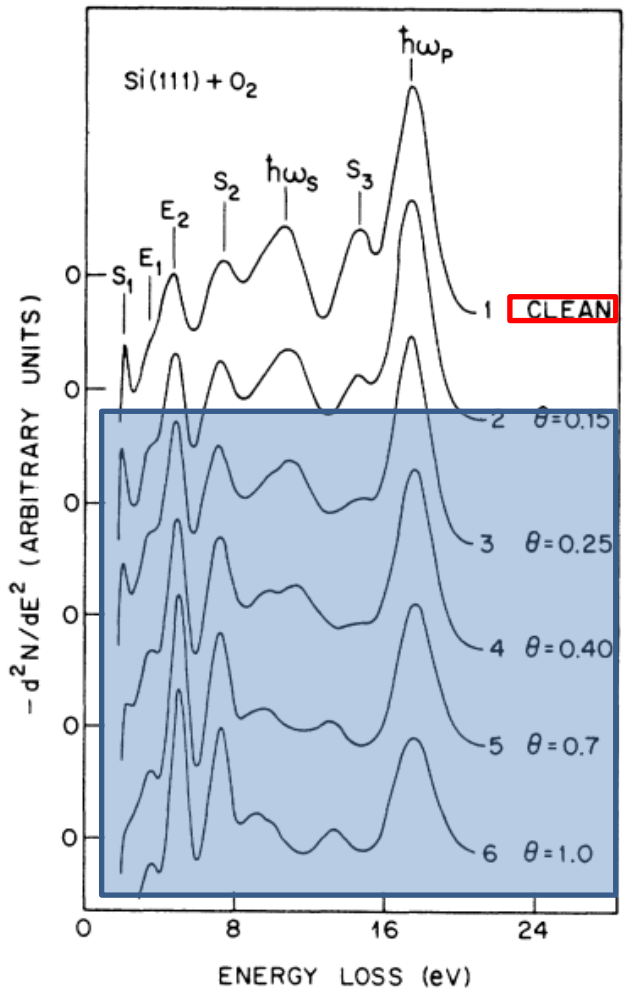

FIG. 2. Negative second derivative of the loss spectrum of a clean silicon (111)7×7 surface (curve 1) and spectra of increasing coverage with oxygen. Primary energy is 100 eV.

$h\omega_p$: bulk plasmon
$h\omega_s$: surface plasmon
E_1,E_2: bulk interband transitions
S_2,S_2,S_3: transitions from occupied surface states

EELS + STEM: atomic chemical contrast

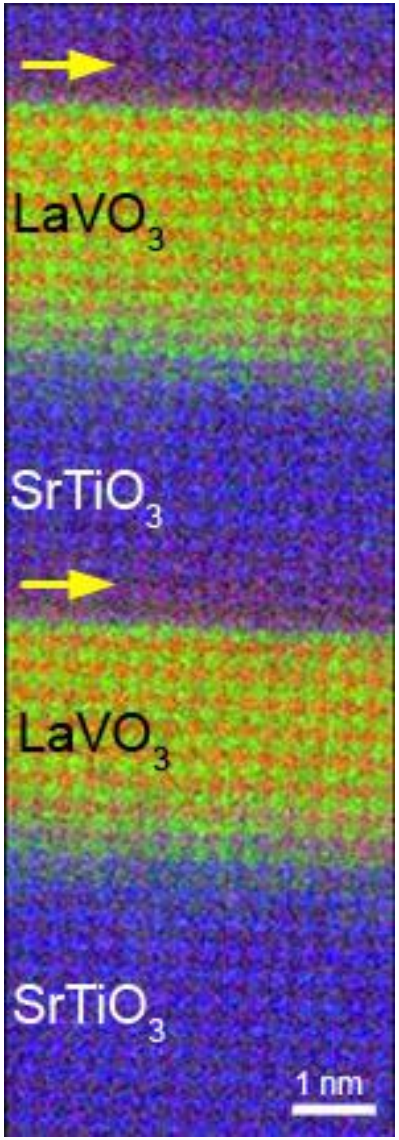

Atomic-resolution EELS chemical composition map taken on the Nion UltraSTEM 100 microscope. V = red, La = green, Ti = blue. Yellow arrows point to purple bands showing V/Ti intermixing. This 128x375 pixel spectrum-image was taken at 10ms/pix (~15 min total acquisition) with no drift compensation. (Courtesy L. Fitting-Kourkoutis & D. Muller). www.nion.com

HREELS

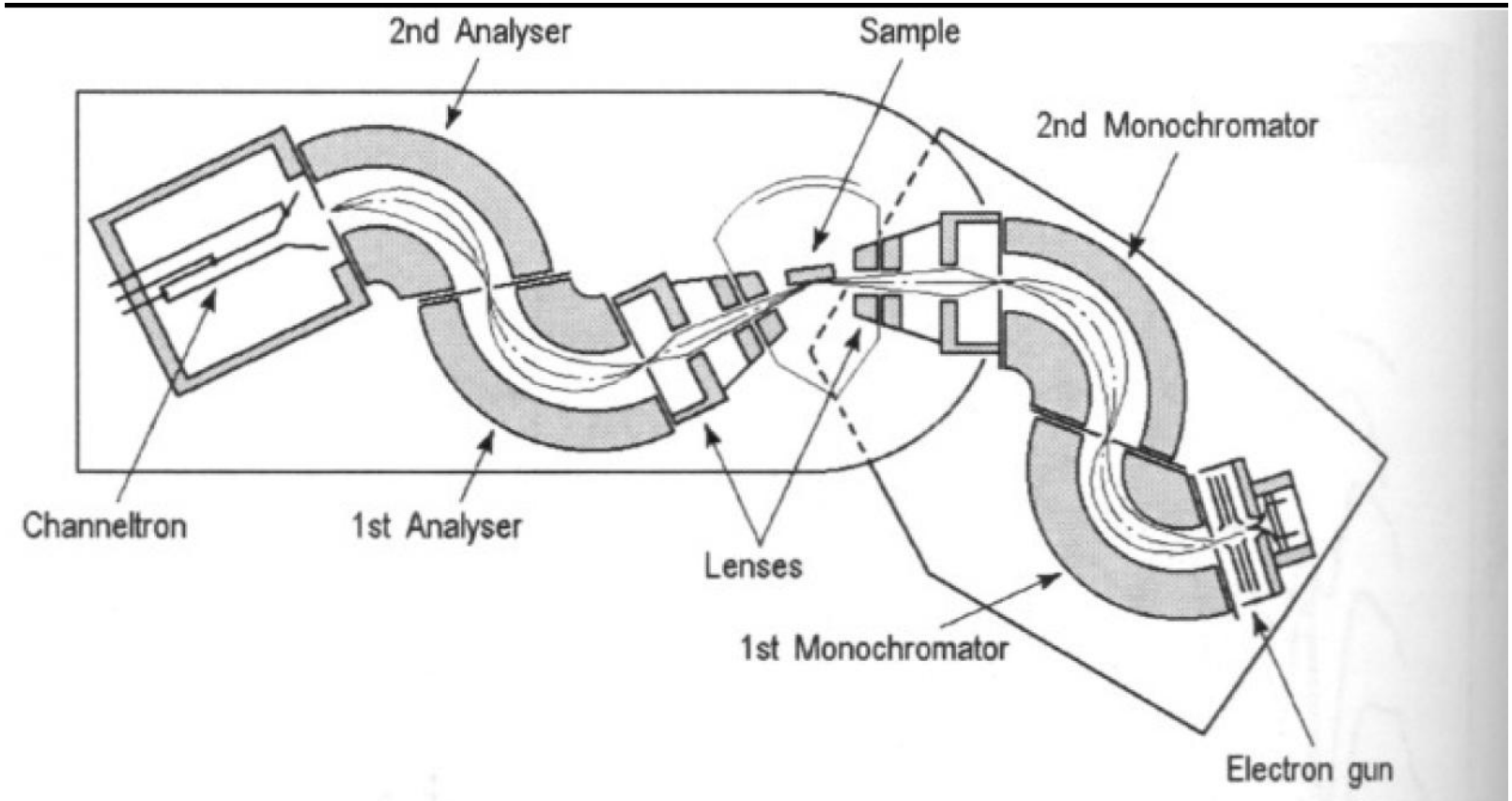

Fig. 5.15. A typical experimental set-up used for high-resolution electron energy loss spectroscopy. It comprises a cathode emission system, a monochromator, two lens systems, an analyzer, and an electron detector. Both analyzer and monochromator utilize 127°-angle cylindrical sector deflectors as the energy dispersive elements (after Ibach [5.11])

HREELS

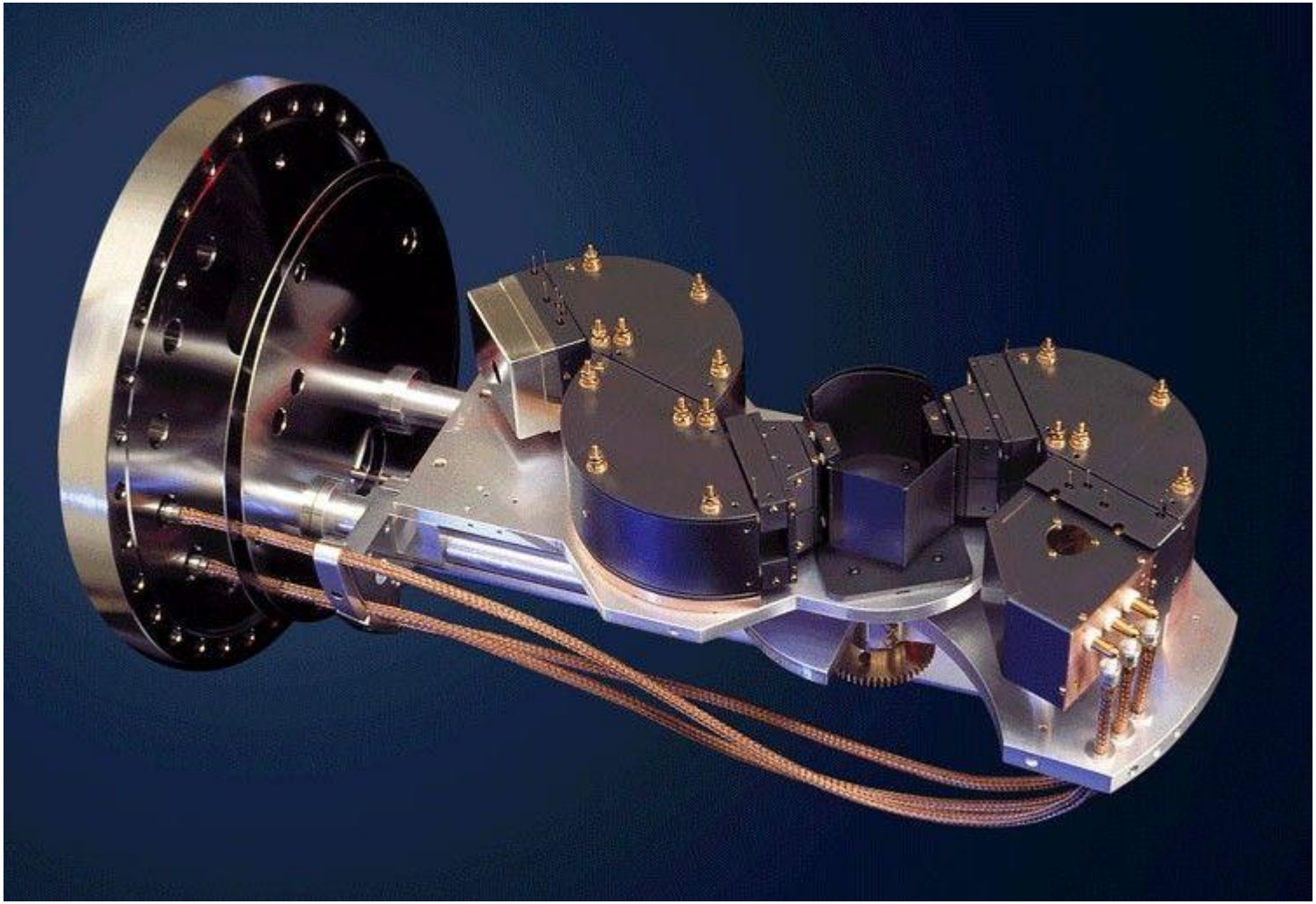

HREELS example: graphene

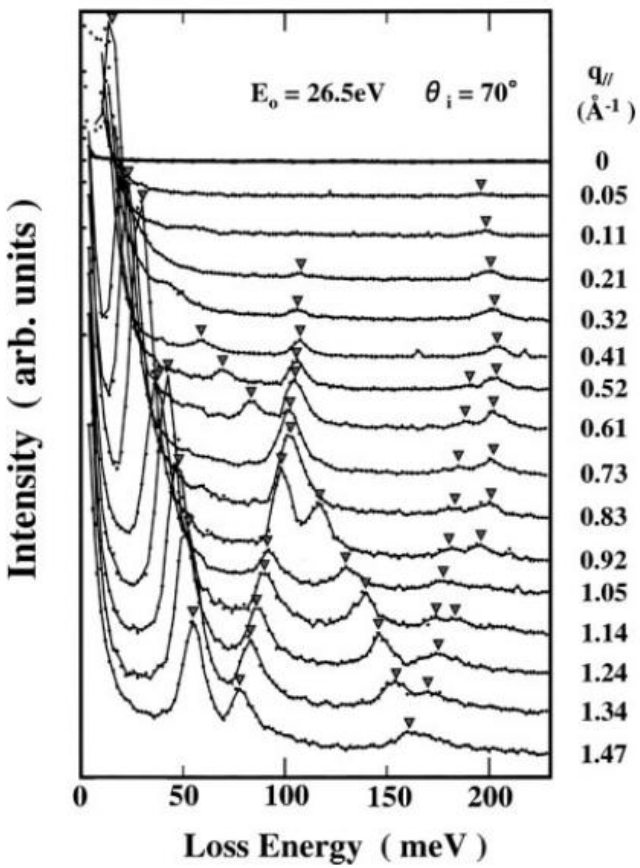

Figure 3. The HREEL spectra of graphene sheets on $BC_3/NbB_2(0001)$ measured along the $\Gamma - M$ direction in the surface Brillouin zone.

G-mode

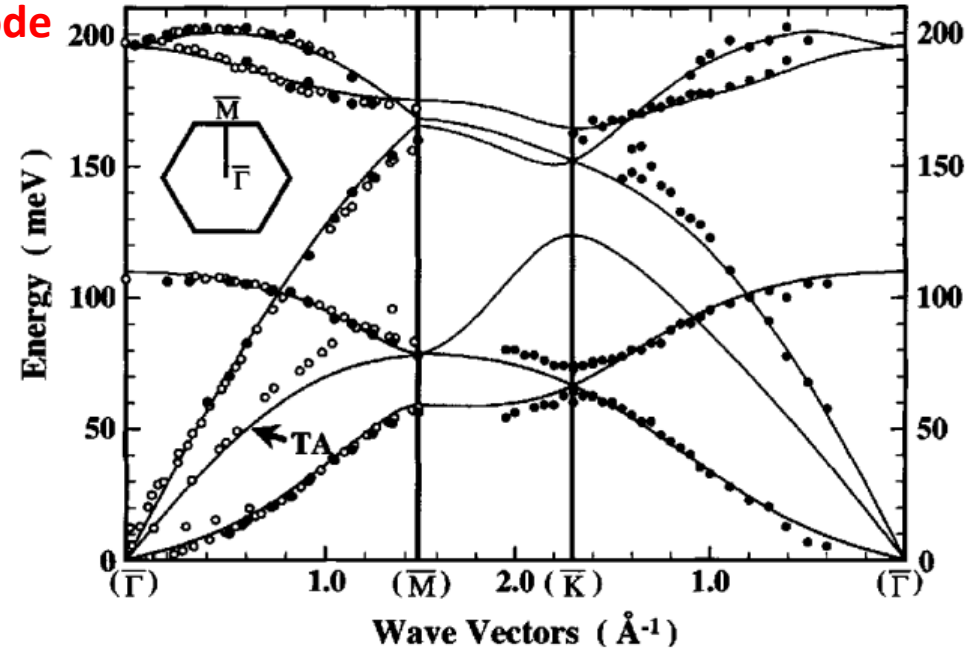

Figure 4. Phonon energy dispersion curves of the graphene sheets determined experimentally (solid circles) and theoretically (solid curves). Phonons in the bulk graphite surfaces are also shown for comparison (open circles).

Types of magnetic order

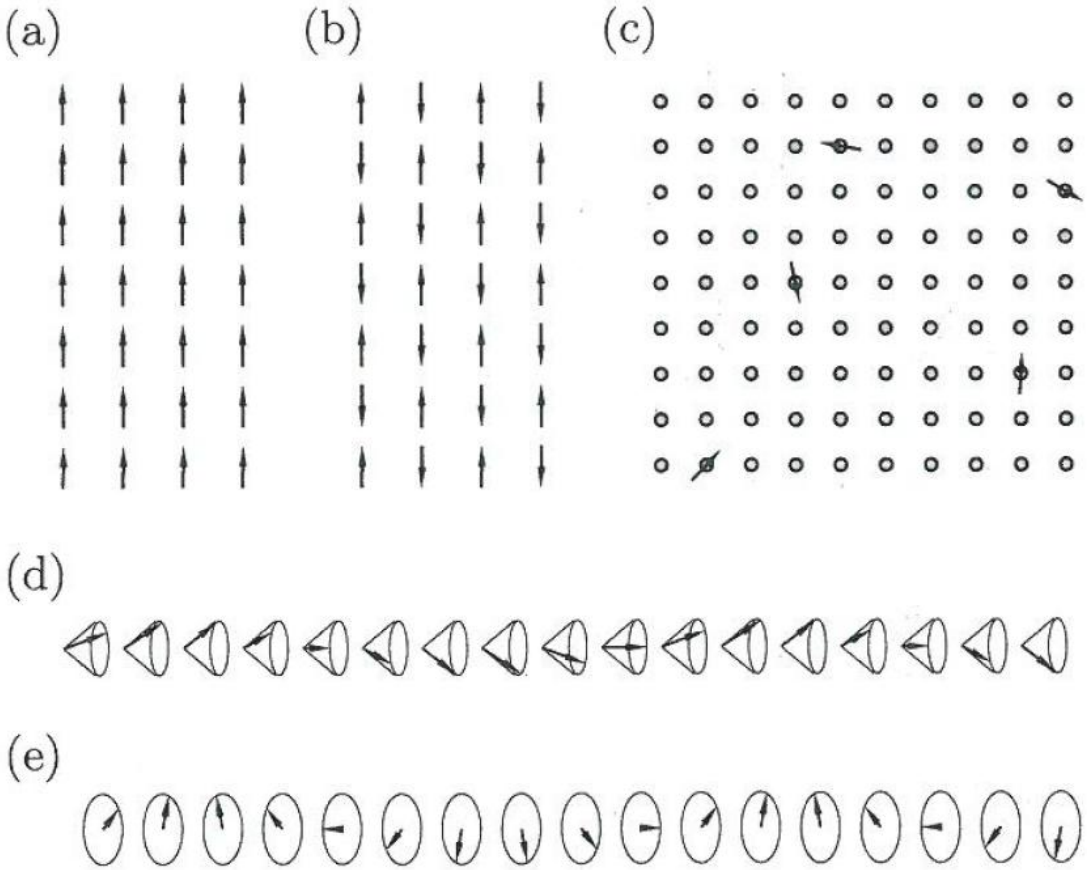

Fig. 5.1 Various spin arrangements in ordered systems: (a) ferromagnets, (b) antiferromagnets, (c) spin glasses and (d) spiral and (e) helical structures.

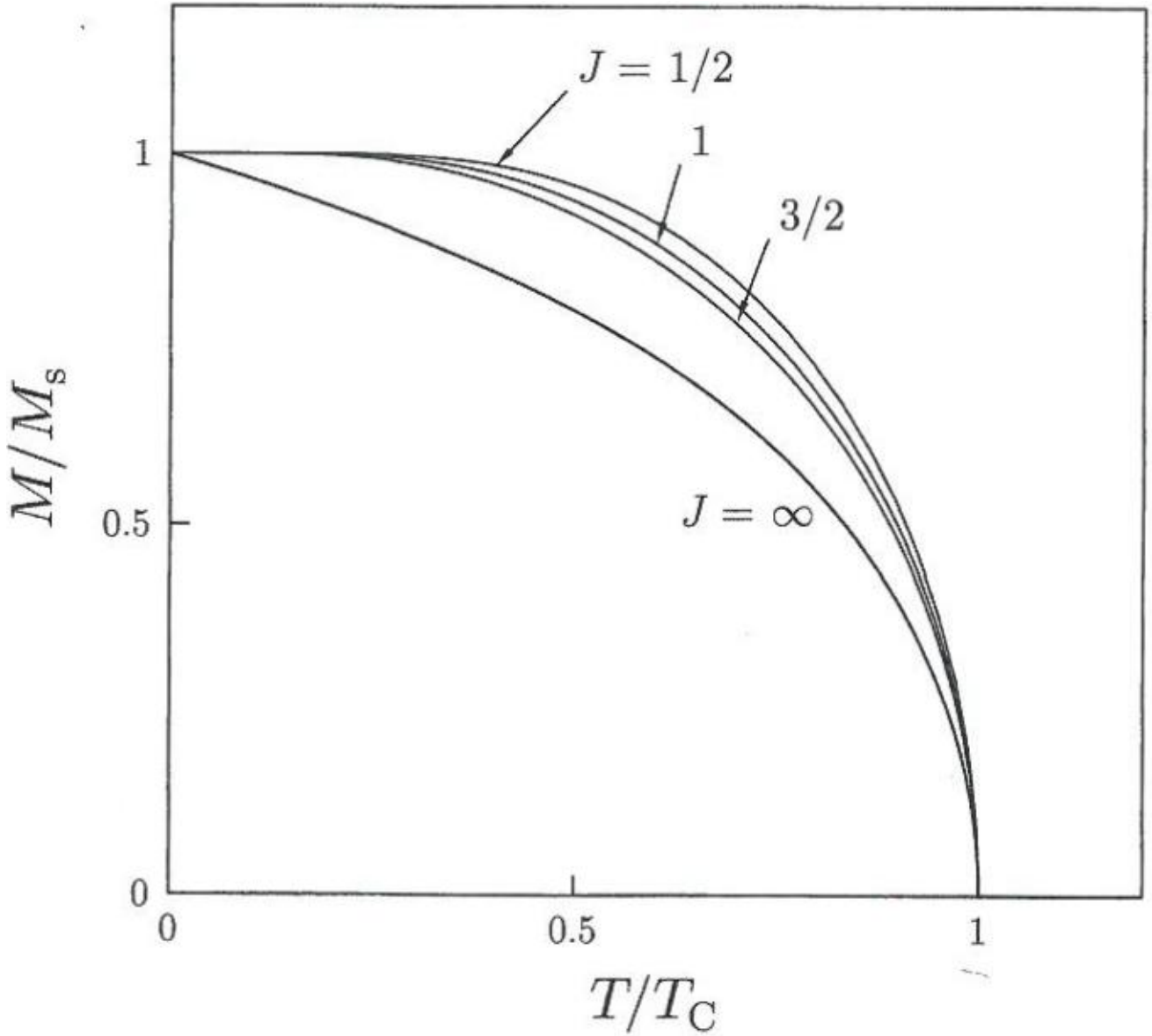

Fig. 5.3 The mean-field magnetization as a function of temperature, deduced for different values of J.

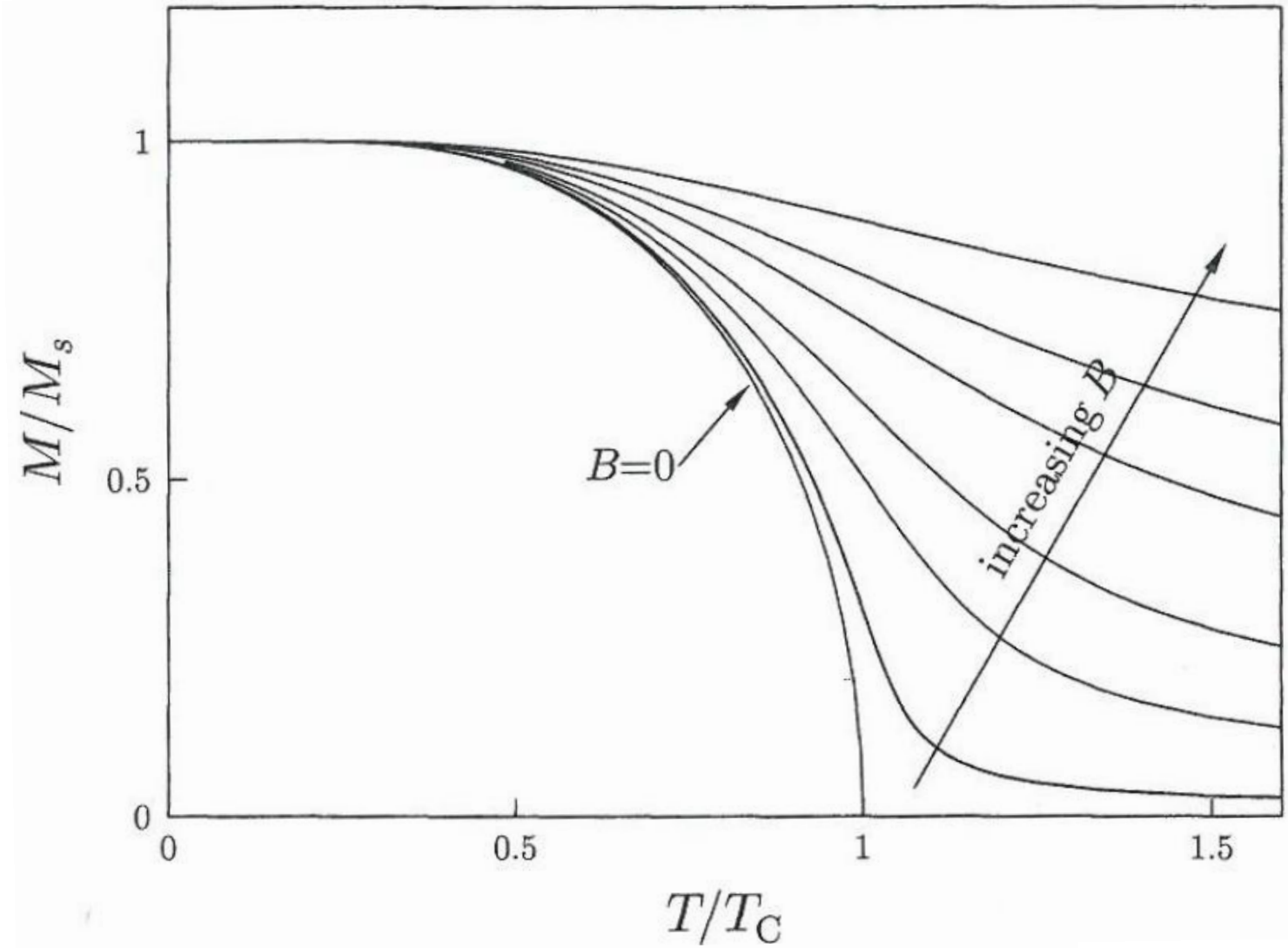

Fig. 5.5 The mean-field magnetization as a function of temperature for $J = \frac{1}{2}$, calculated for different values of the applied field B. The phase transition is only present when $B = 0$.

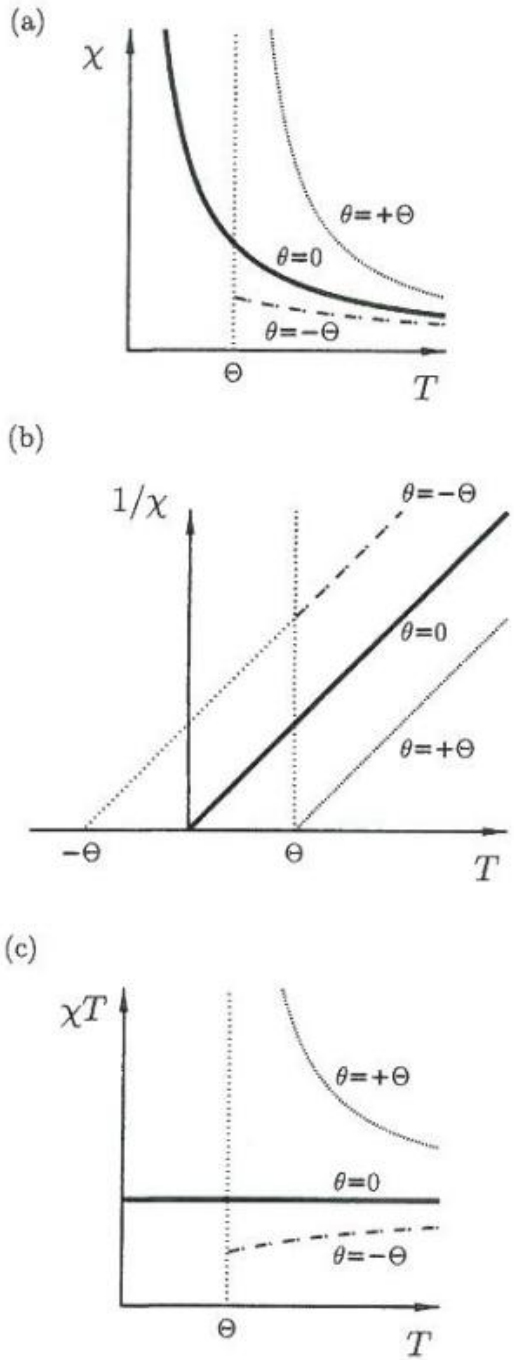

Fig. 5.7 The Curie Weiss law states that χ
$1/(T-\theta)$ for $T > \theta$. This is shown in (a) f
three cases: $\theta = 0$ (paramagnet), $\theta = \Theta >$
(ferromagnet) and $\theta = -\Theta < 0$ (antiferr
magnet). Straight-line graphs are obtained l
plotting $1/\chi$ against T as shown in (b) wi
the intercept on the temperature axis yieldi
θ. A graph of χT against T can be consta
($\theta = 0$), increasing for decreasing T ($\theta >$
or decreasing for decreasing T ($\theta < 0$),
shown in (c).

Susceptibility of an antiferromagnet

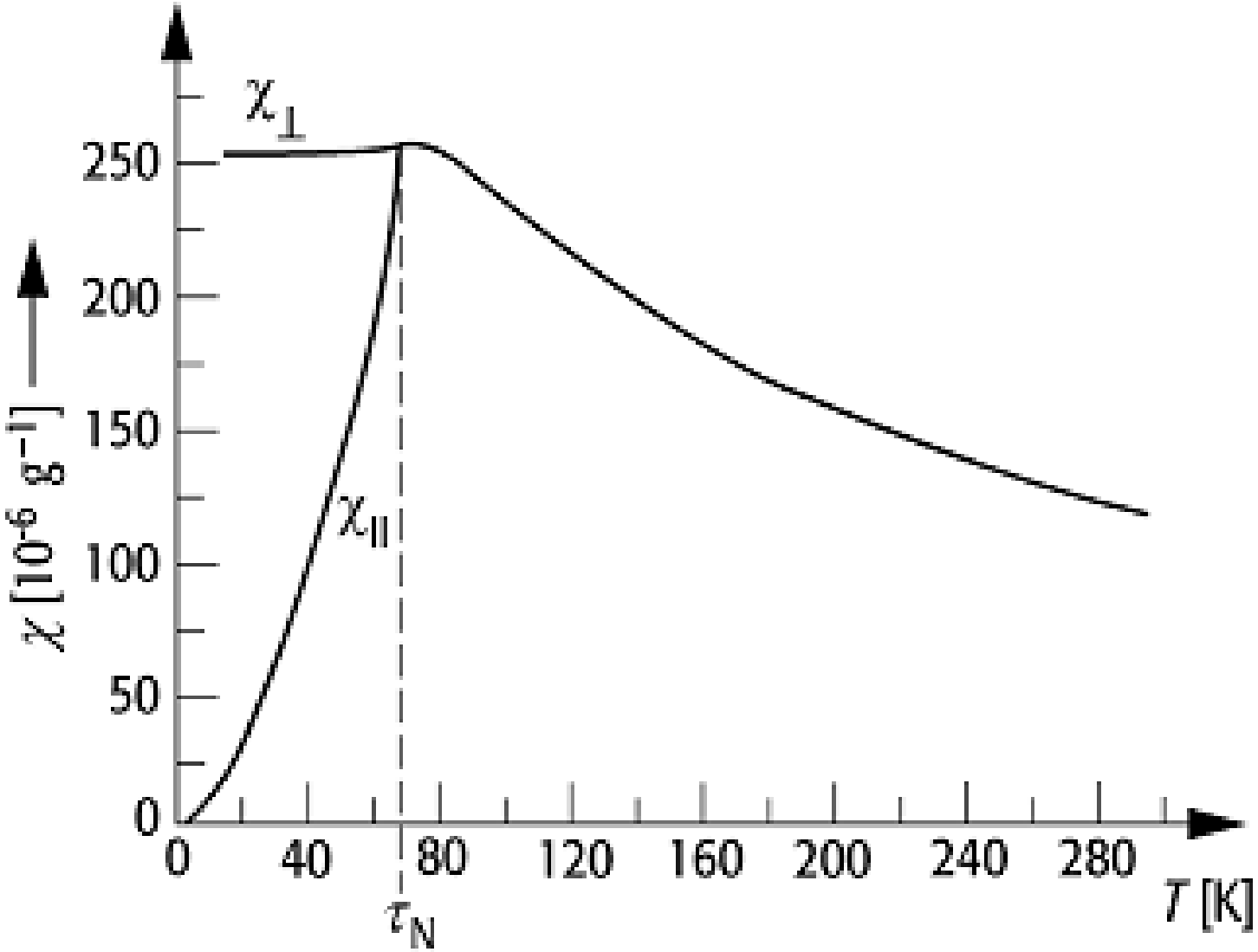

χ(T) – example: spin ladder

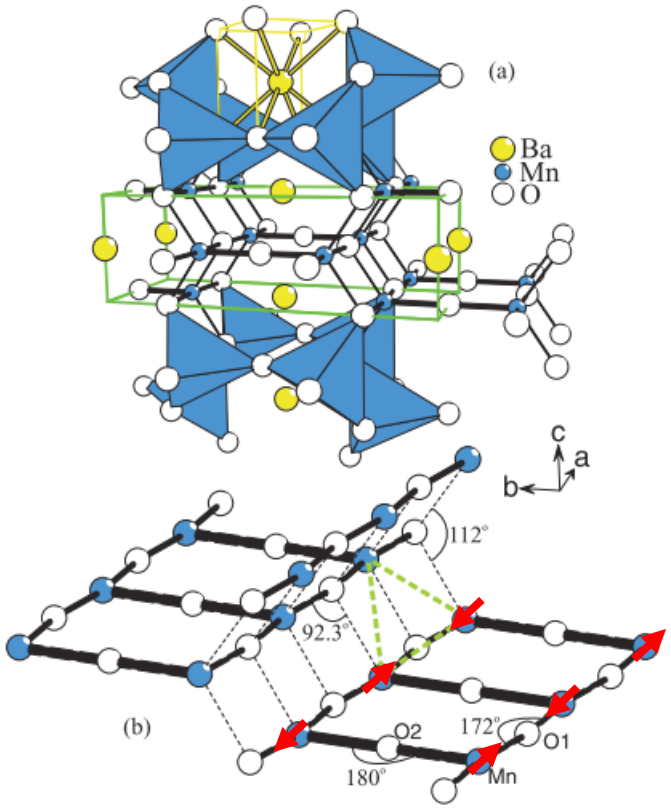

FIG. 1. (Color online) (a) Room-temperature structure of $BaMn_2O_3$. The open balls at the corners of the Mn-containing polyhedra are oxygen atoms; the closed large and small balls represent Mn and Ba ions, respectively. In addition, the unit cell is displayed by lines. (b) A selected part of the structure showing the Mn-O substructure with Mn–O–Mn bond angles. The thick dashed lines indicate the geometrical frustration, as discussed in the text.

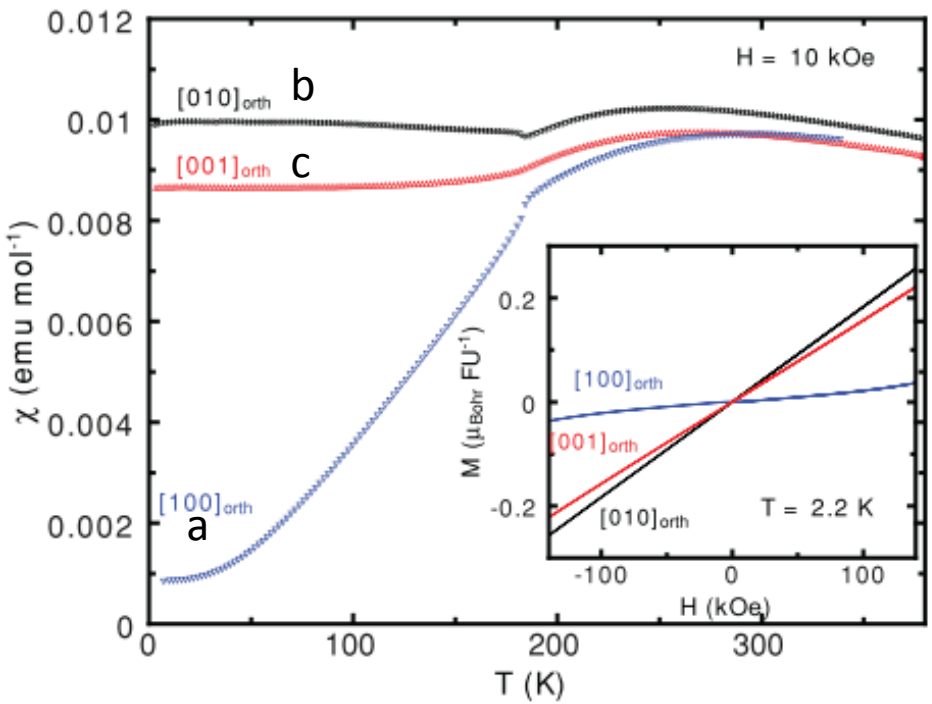

FIG. 2. (Color online) Magnetic susceptibility as a function of temperature measured in magnetic fields of 1 T applied along all three orthorhombic crystallographic directions of $BaMn_2O_3$. The inset displays magnetization curves measured at 2.2 K as a function of the magnetic field up to 14 T applied along the orthorhombic axes.

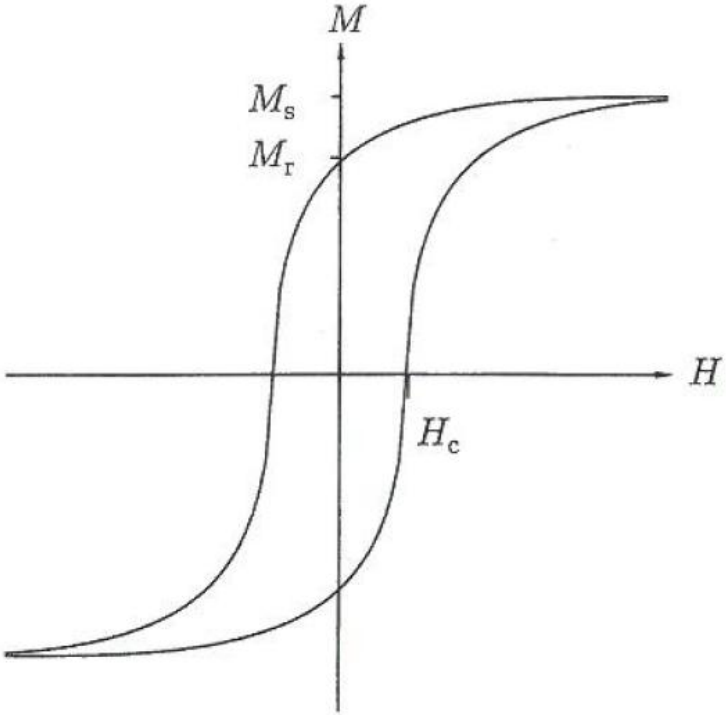

Fig. 6.24 A hysteresis loop showing the saturation magnetization M_s, the remanent magnetization M_r and the coercive field H_c.

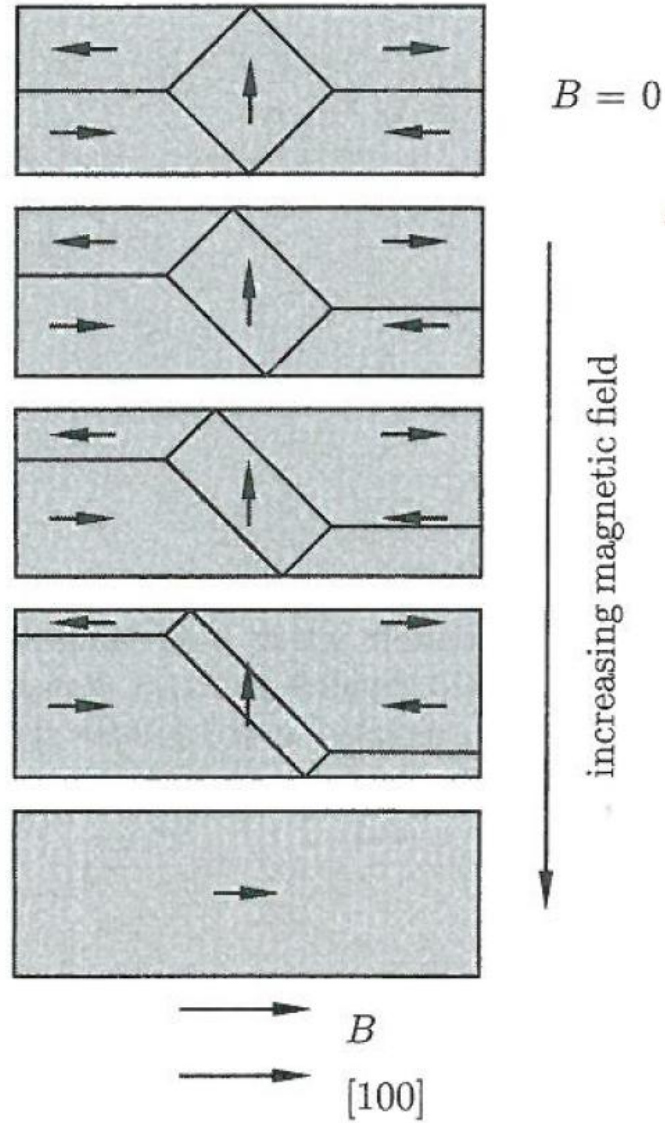

Fig. 6.25 Effect of an applied field on the domain pattern on the surface of a single crystal iron whisker showing domain wall displacement, as the applied B field increases from 0 up to a maximum value.

Vibrating sample magnetometer (VSM)

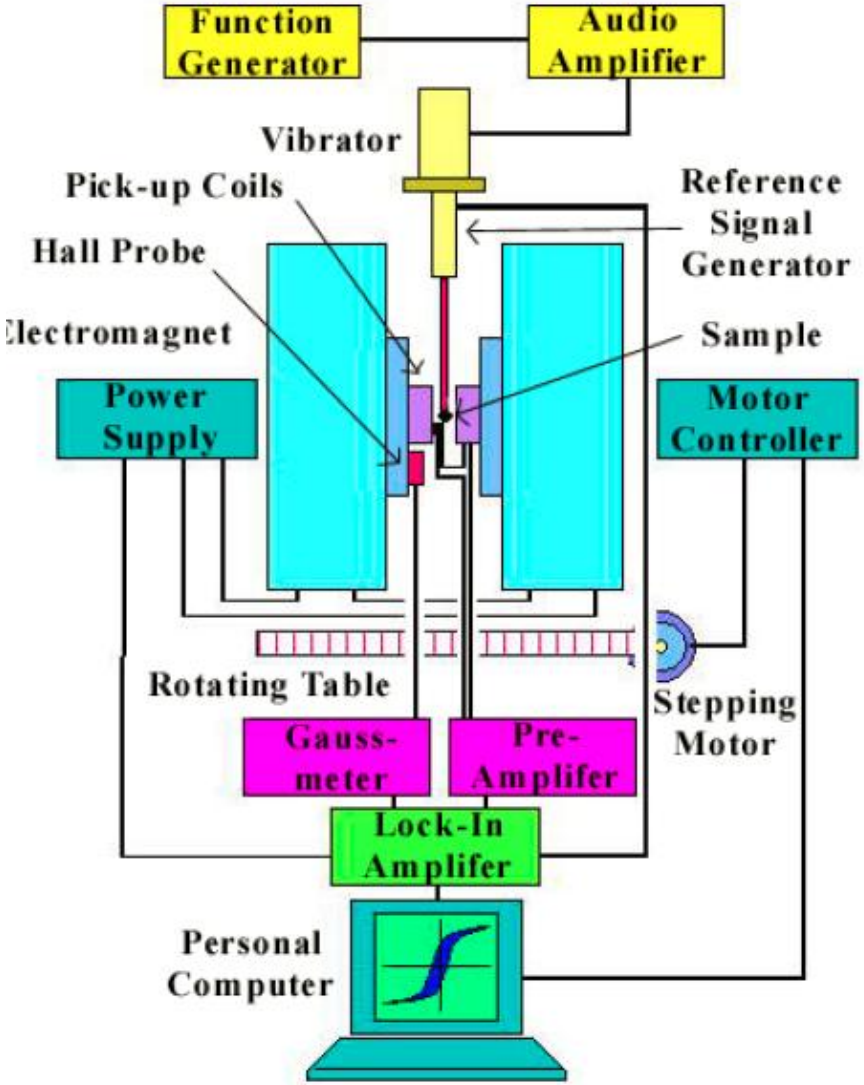

System diagram of Vibrating Sample Magnetometer

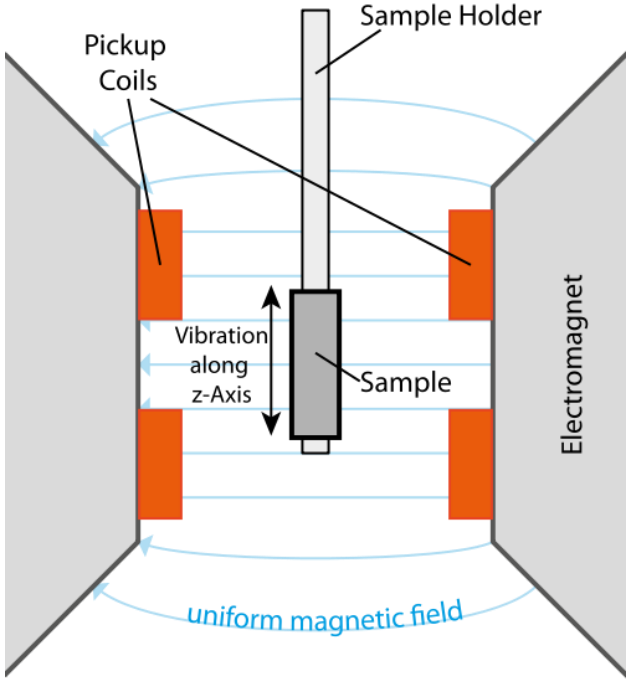

$$U = -N\dot{\Phi} \propto MV\dot{x}$$

SQUID

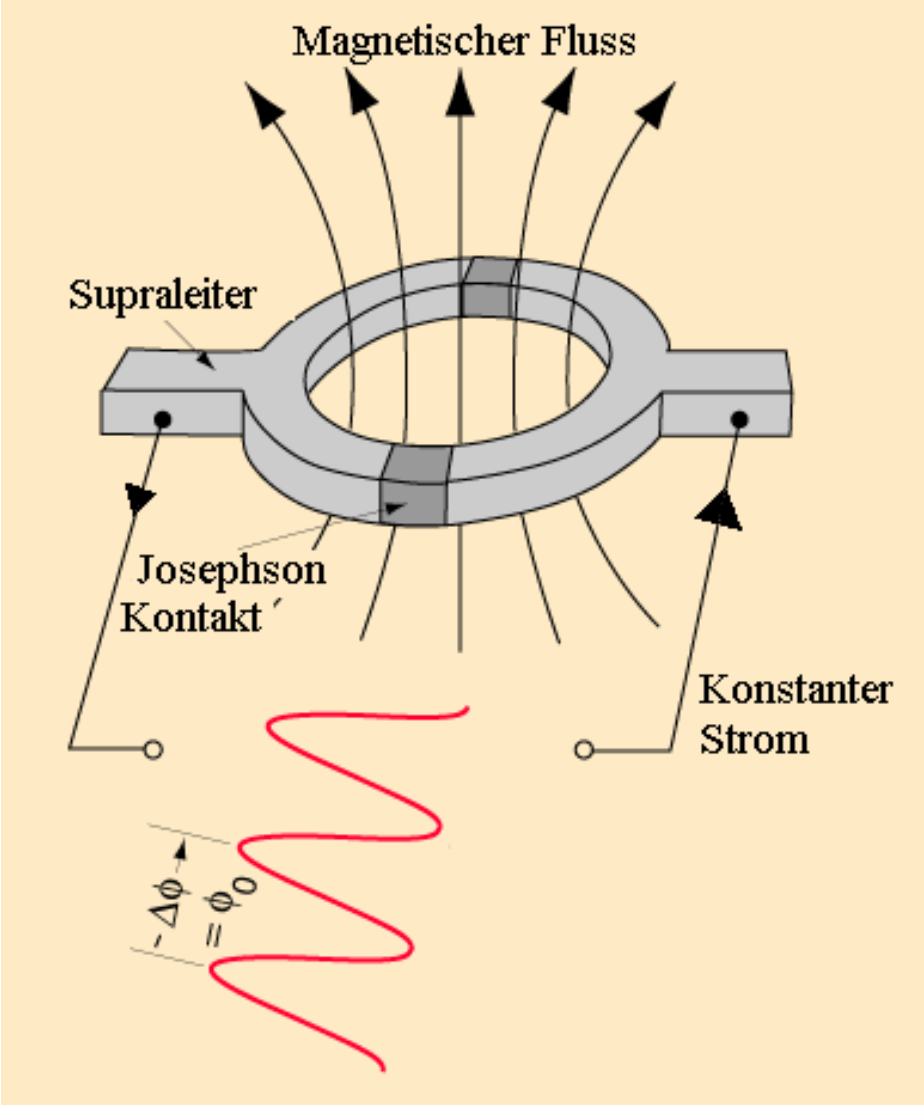
Magnetischer Fluss
Supraleiter
Josephson
Kontakt
Konstanter
Strom
$\Delta\phi = \phi_0$

EuO facts

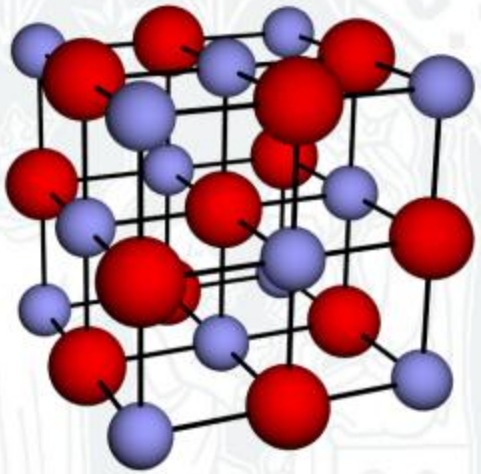

- Ionic rocksalt structure
- Ferromagnetic semiconductor, T_C = 69 K
- T_C increased up to 125 K by doping with Gd
- Colossal magnetoresistance (CMR)
- Photoconductivity
- Large magneto-optical Kerr effect (MOKE): Kerr rotation 7.1°
- Almost 100 % spin polarisation of the charge carriers [1]
- **Metal insulator transition (MIT) in EuO_{1-x} with $\Delta R/R$ up to 1000**

[1] H. Ott, S. J. Heise, R. Sutarto, Z. Hu, C. F. Chang, H. H. Hsieh, H.-J. Lin, C. T. Chen, and L. H. Tjeng
Phys. Rev. B **73**, 094407 (2006)

SQUID-example: EuO

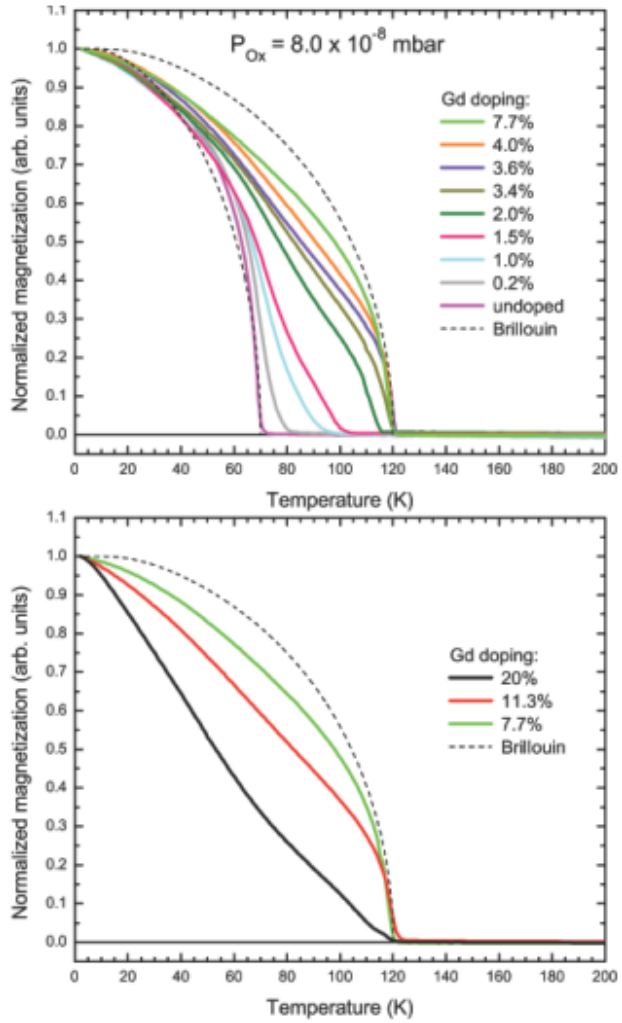

Figure 5.2: Temperature dependence of the normalized magnetization of epitaxial Gd-doped EuO films on YSZ (001) for various Gd concentrations from undoped to 7.7 % (*top panel*) and from 7.7 % to 20 % (*bottom panel*). The SQUID measurements were performed at applied magnetic field of 10 G. Taken from [17].

Neutron collimation (Söller)

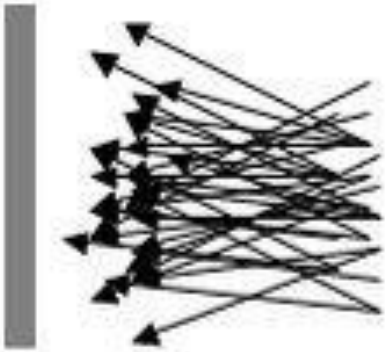

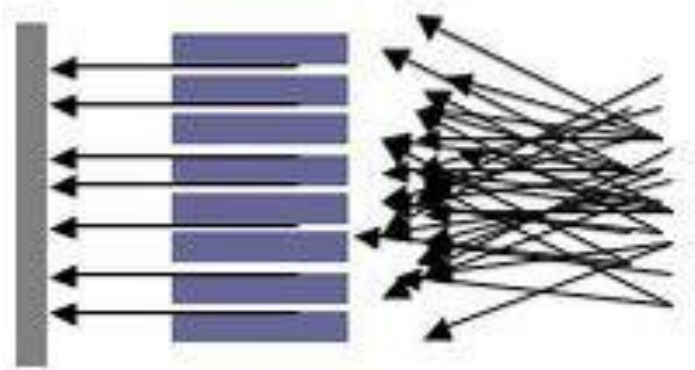

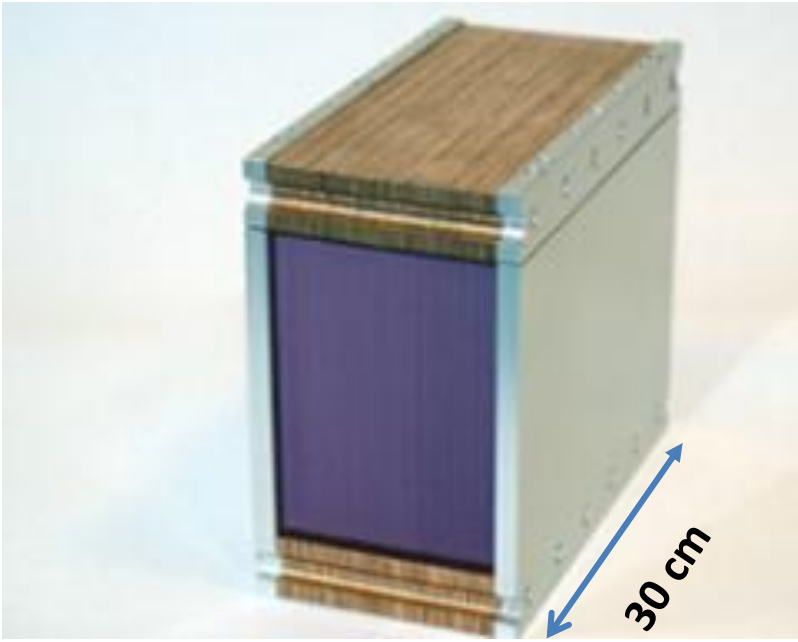

Magneto-optical effects

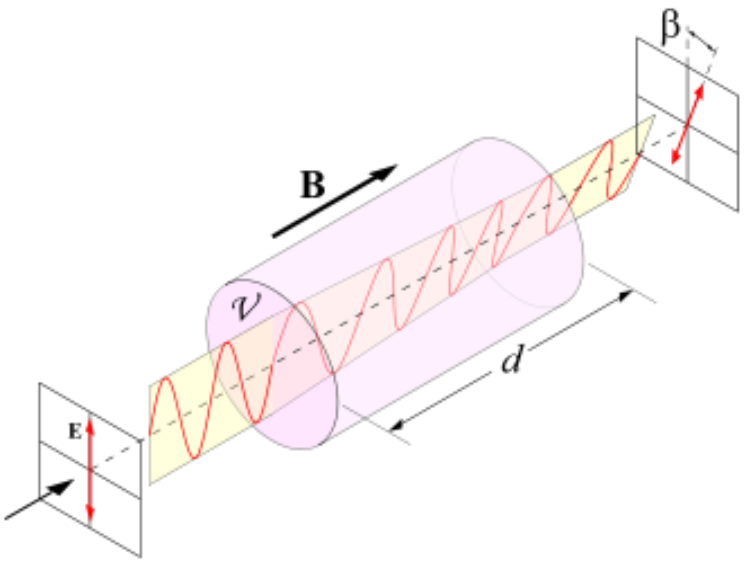

Faraday-effect

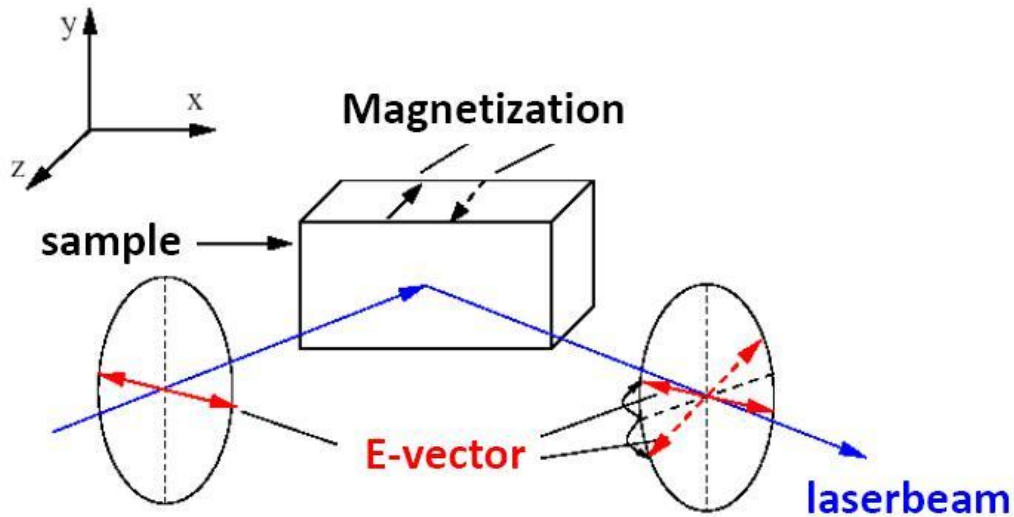

Kerr-effect

MOKE: Experimental setup

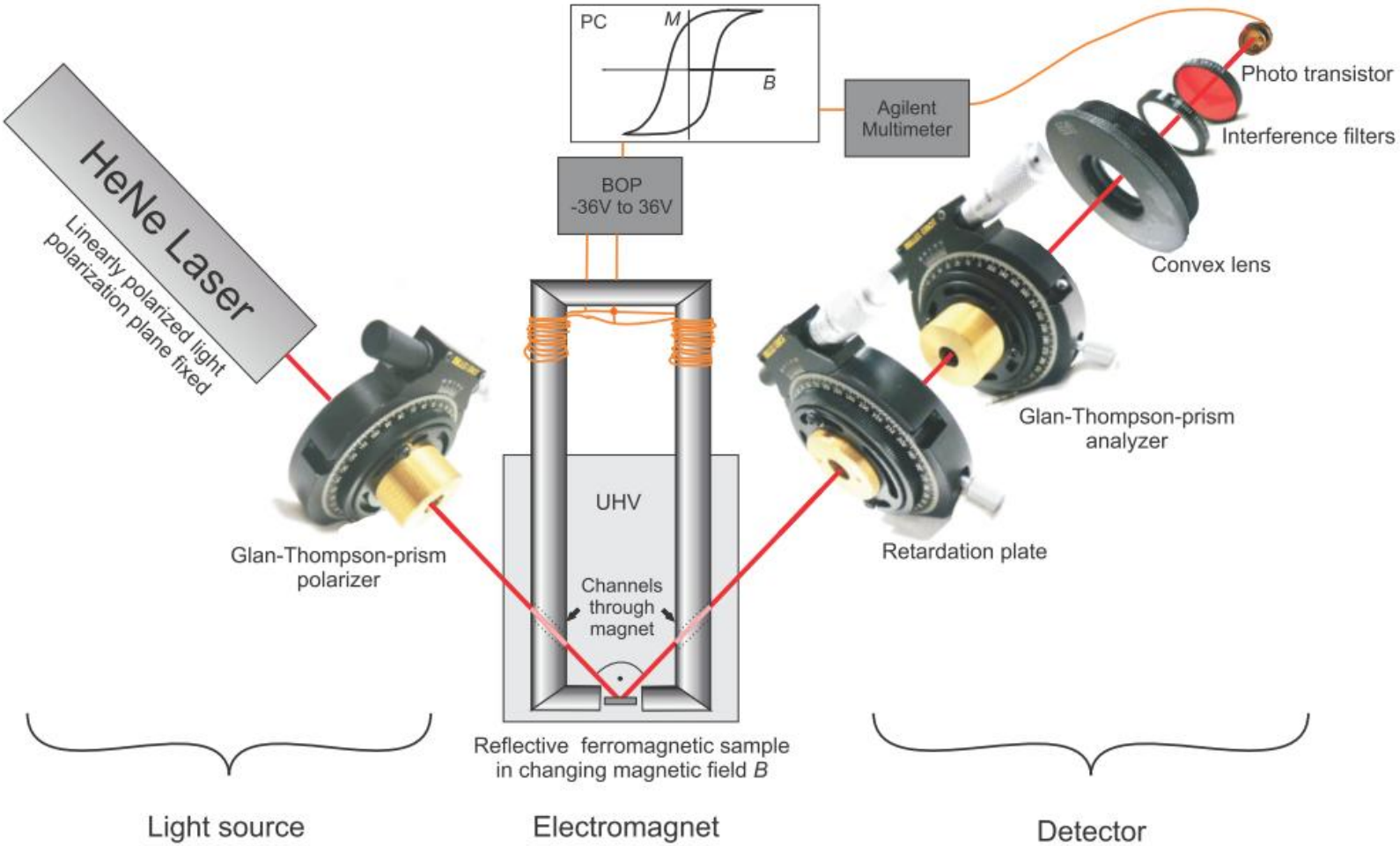

Figure 4.1: Arrangement of the longitudinal MOKE setup. The figure is assembled with drawings and with photographs of the used optical components in their mechanical mountings. The construction aims on the determination of a samples magnetic properties under UHV conditions.

PhD-thesis J.Klinkhammer, Universität zu Köln, 2013

MOKE: Geometries

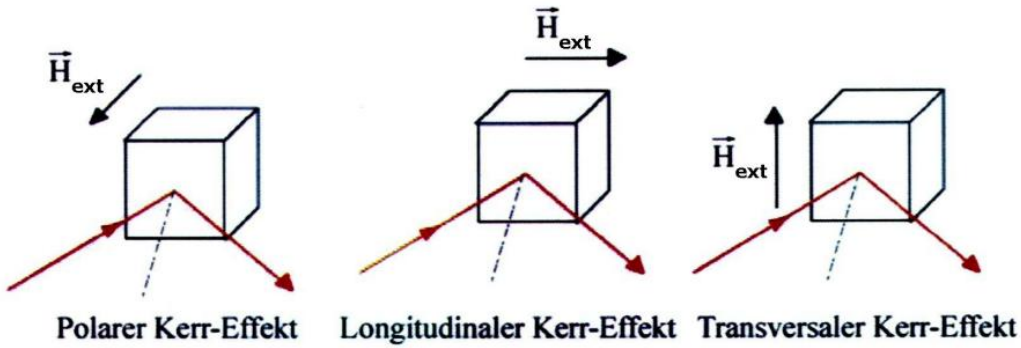

Abbildung 1.3.2: Polare, longitudinale und transversale MOKE-Geometrie [Rod09]

BSc-thesis A. Jacobi, Universität zu Köln, 2010

Moke: Ellipticity

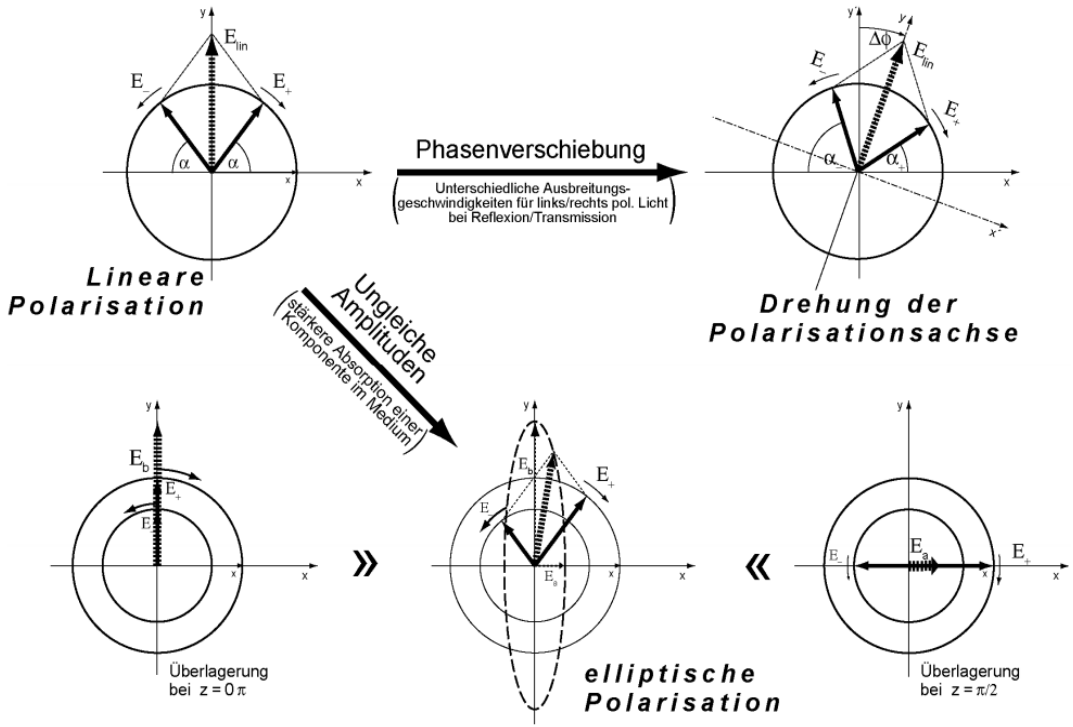

Abb. 10: Auswirkung der Reflexionseigenschaften magnetischer Materialien auf einfallendes linear polarisiertes Licht

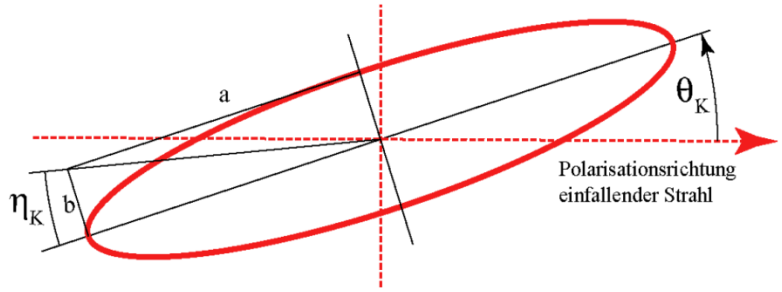

Abb. 9: Kerrdrehung der Polarisationsrichtung um Θ_K und Polarisationsänderung von linear polarisiert zu elliptisch polarisiert. Die Elliptizität der reflektierten Strahlung ist bestimmt über η_K.

Rodenbücher, C. Magnetooptischer Kerr-Eekt (MOKE). Versuchsanleitung zum Physikalischen Praktikum, RWTH Aachen, 2009

MOKE: sketch of measurement

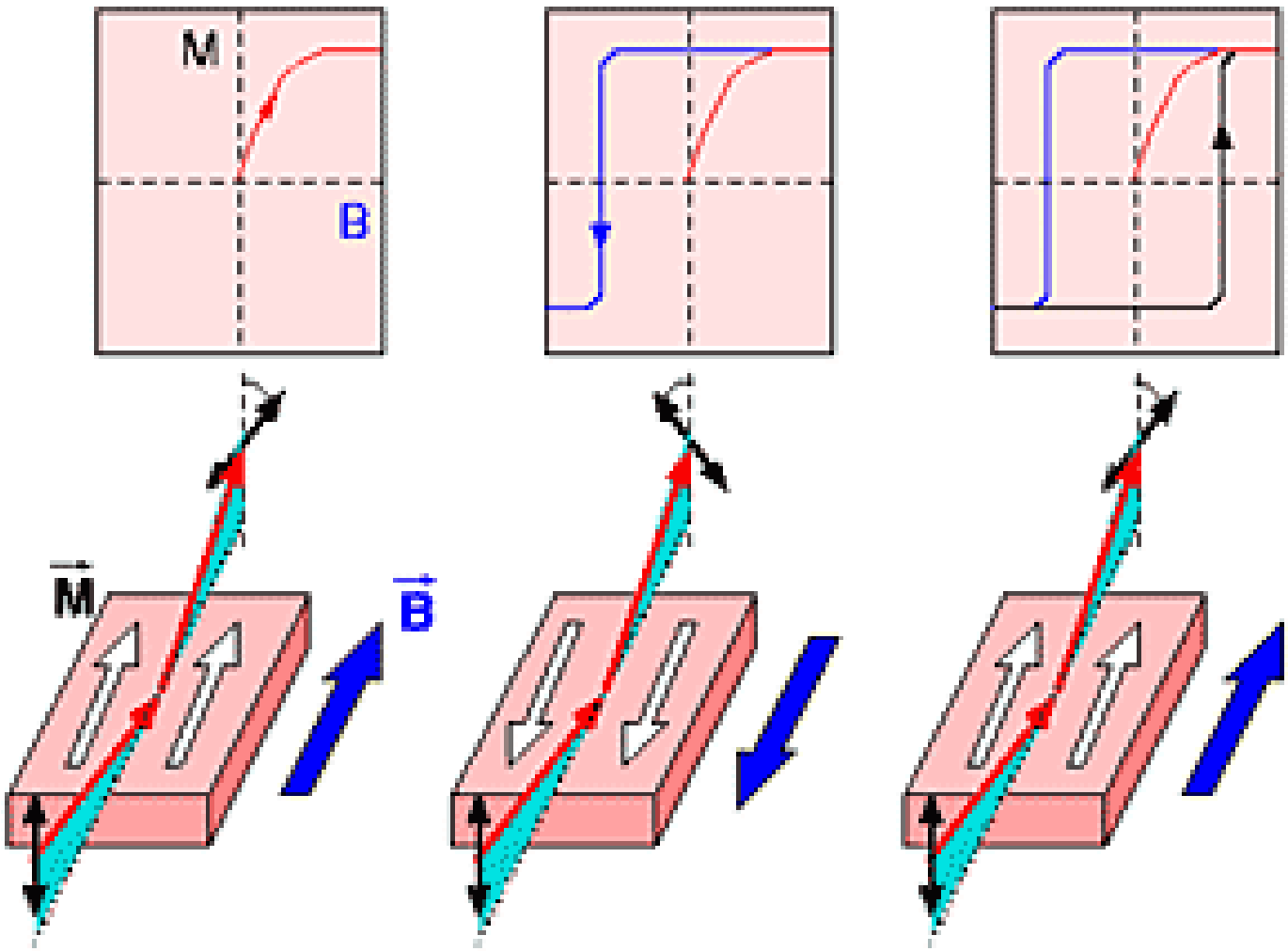

Example: MOKE on EuO

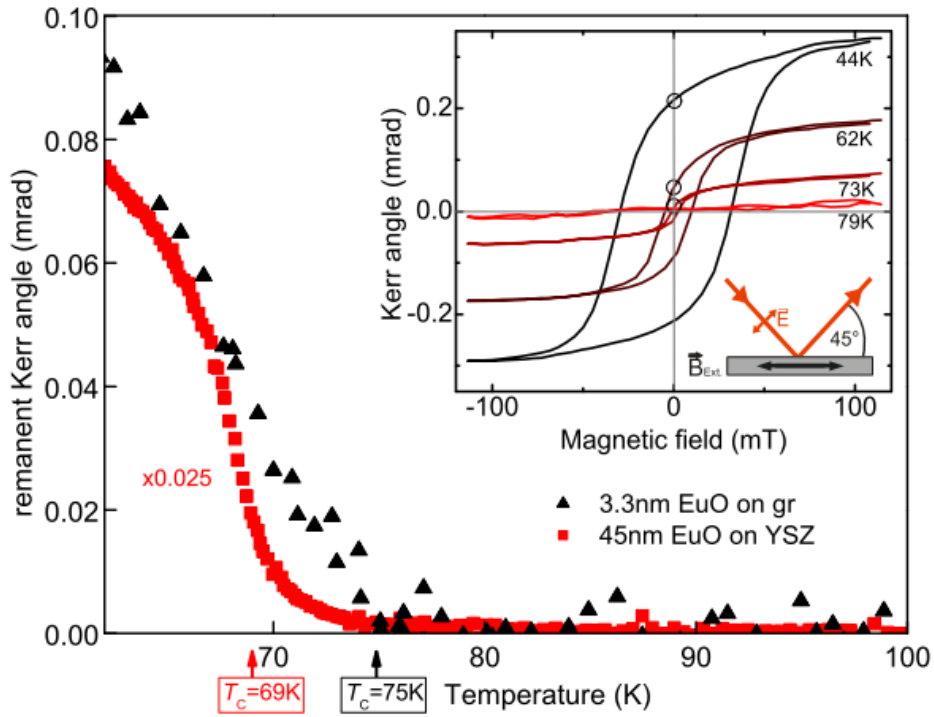

FIG. 3. (Color online) Longitudinal MOKE measurement for a 3.3 nm thin EuO(100) film as presented in Fig. 2 (b). Main plot: Triangular data points: Remanent Kerr rotation (in small residual field) vs. temperature T. The data reveal $T_C \approx$ 75 K. Square data points: Reference measurements on *ex situ* grown 45 nm thin Al capped EuO film on YSZ with T_C = 69 K. Inset: Hysteresis loops of the 3.3 nm thin EuO film on graphene at the indicated temperatures. Circles indicate the remanent Kerr rotation.

MOKE microscope

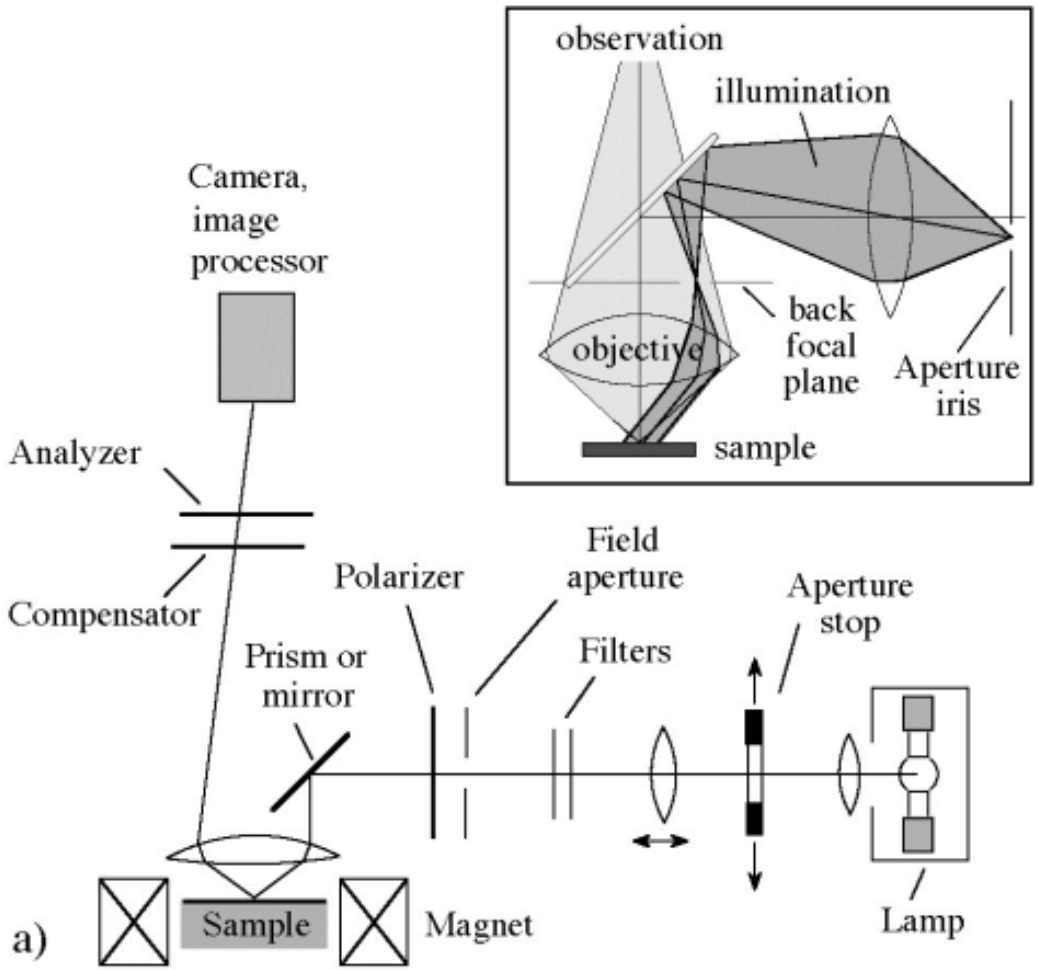

Fig. 6 Schematic representation of the main components of a magneto-optical Kerr microscope. The inset shows the beam path of an optical reflected light microscope. The aperture iris is displaced from the optical axis to generate oblique incidence of light.

$Nd_2Fe_{14}B$

MOKE microscope

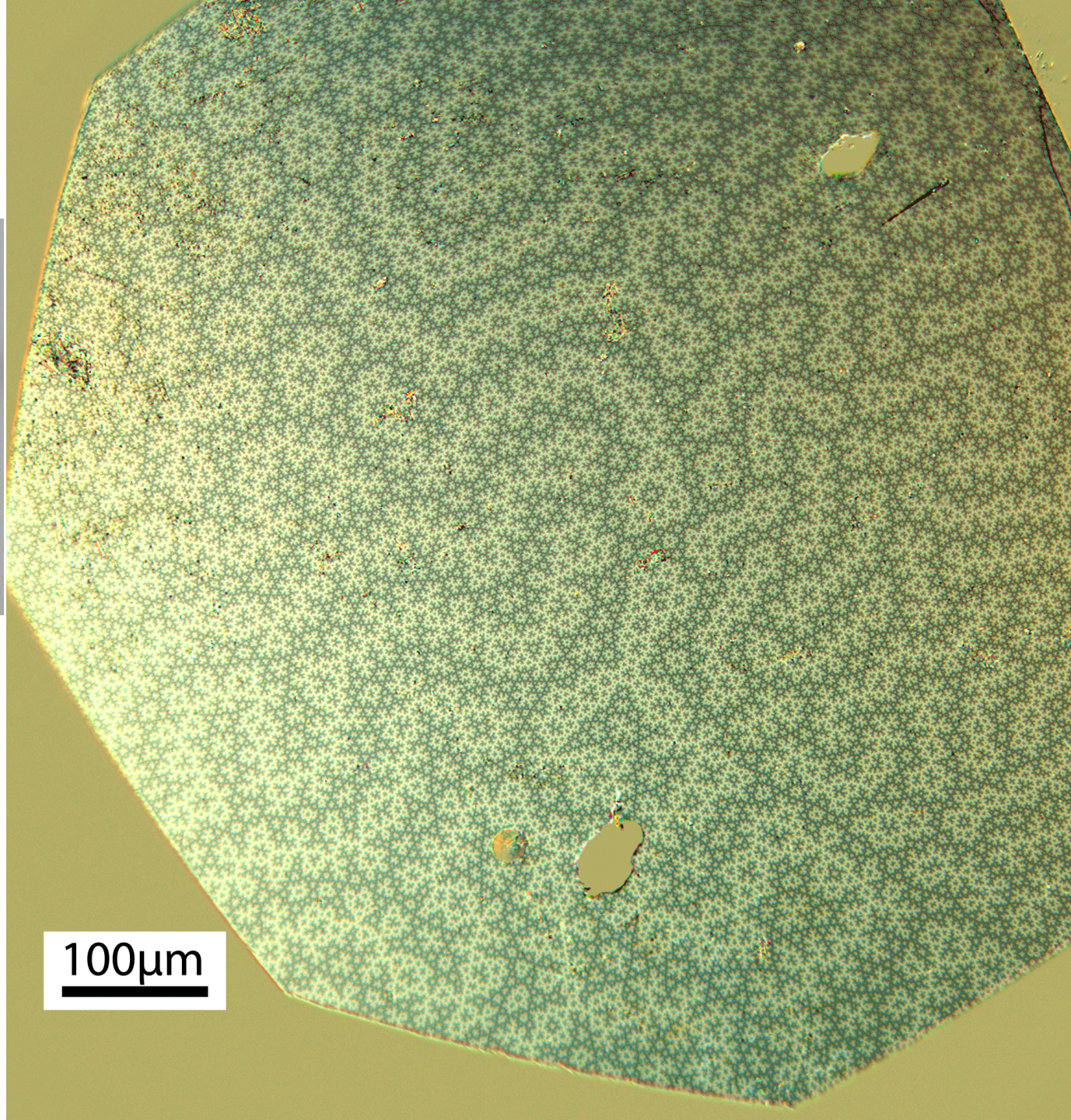

Magnetic cicular dichroism

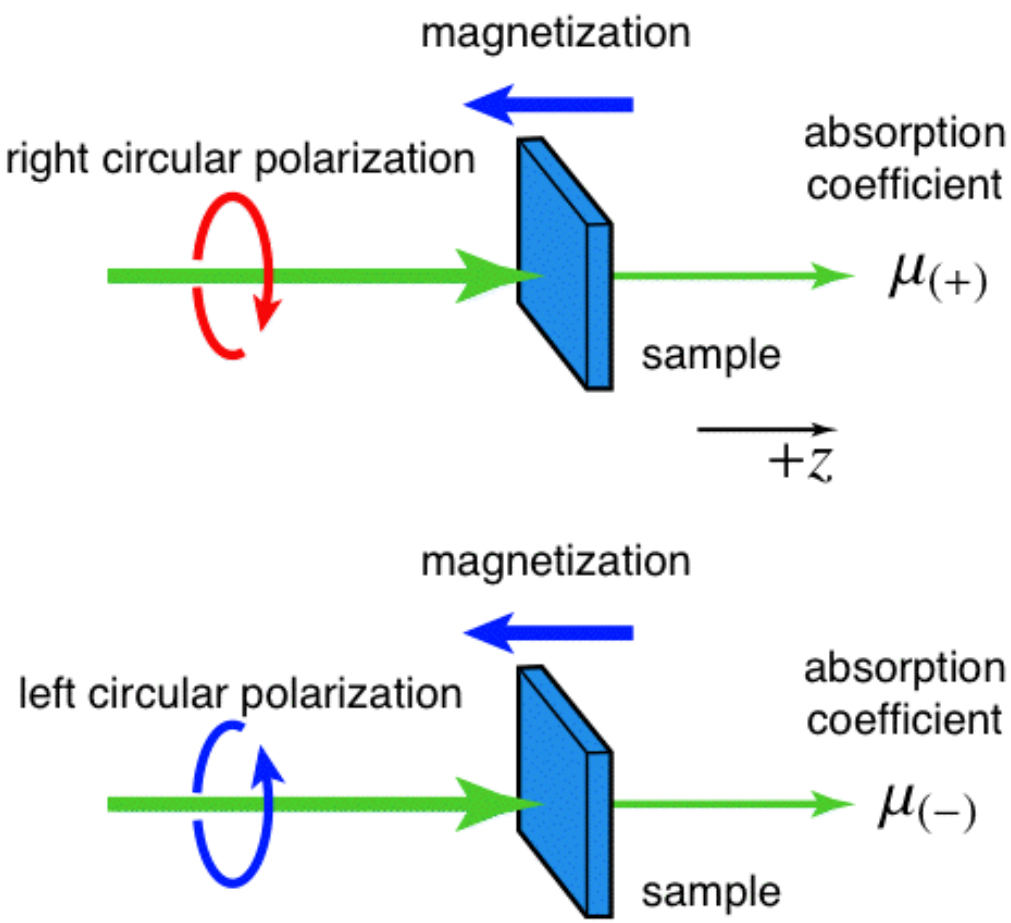

X-ray magnetic circular dichroism (XMCD)

$$\Delta\mu = \mu_{(+)} - \mu_{(-)}$$

XMCD-example

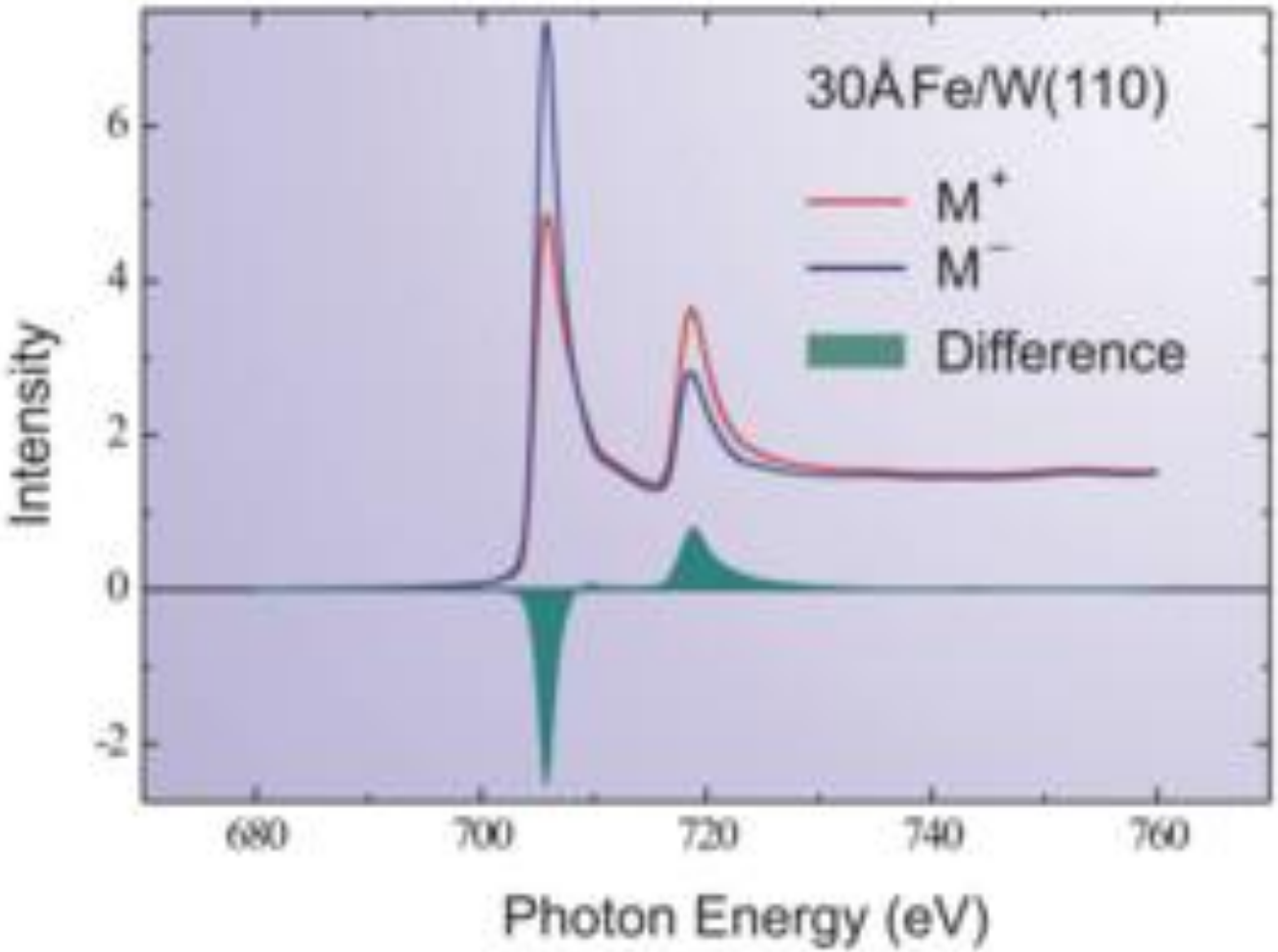

Mott detector

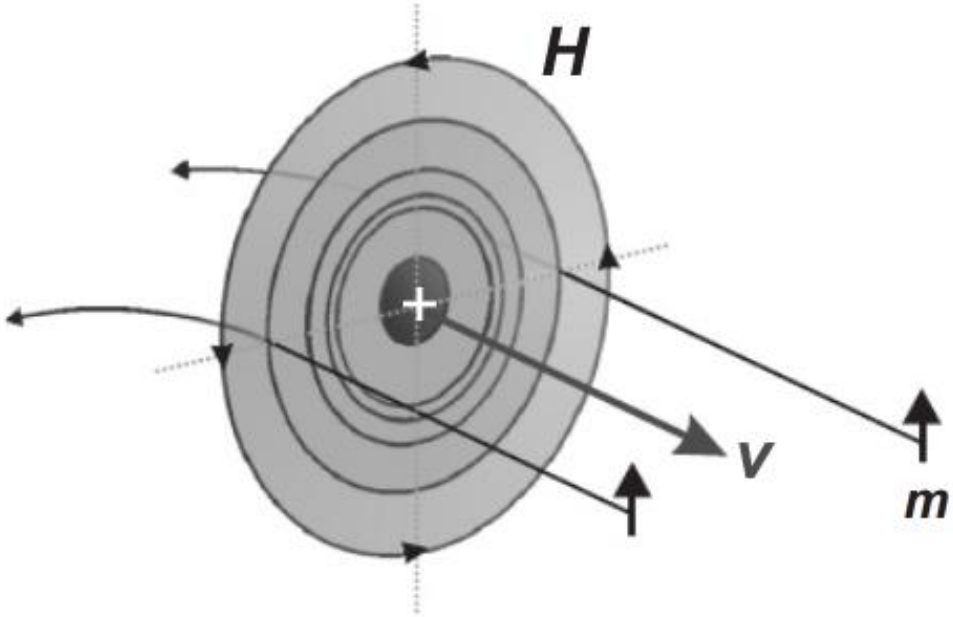

Fig. 3.10. Illustration how spin-orbit coupling in elastic Coulomb scattering can spatially separate the two spin states: The electron with its magnetic moment up is incident on an atom whose projection perpendicular to the incidence direction is shown. In the rest system of the electron, the positive charge of the atomic nucleus moves toward it with a velocity $\boldsymbol{v}$. This is equivalent to an electric current with circular magnetic field lines as shown. The force $\boldsymbol{F}$ on the magnetic moment of the electron is directed toward increasing field when the moment is parallel to the field (*right*), but toward decreasing field when it is antiparallel (*left*). If $\boldsymbol{m}$ and $\boldsymbol{H}$ are perpendicular the force is zero. In this way, the magnetic moment of the electron experiences a force toward the left side when it is aligned upward no matter on which side of the atom it passes. In contrast, electrons with magnetic moment "down" are preferentially scattered to the right in our figure

Mott detector

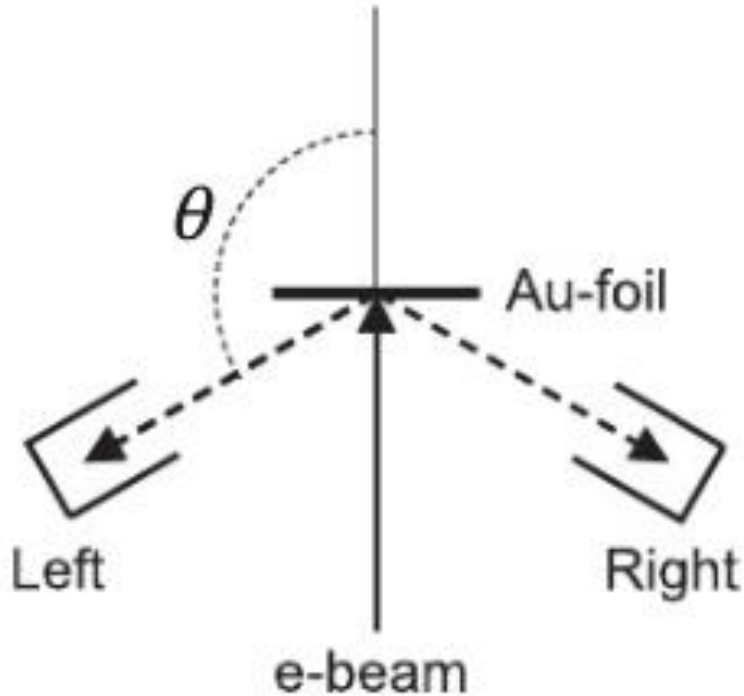

Fig. 3.11. Experimental setup to measure the scattering asymmetry A caused by the spin polarization of an electron beam. The electrons elastically scattered into the scattering angle θ to the right and to the left are measured. If the spins of the electrons in the incident beam are polarized perpendicular to the scattering plane, a scattering asymmetry occurs which is proportional to the degree of spin polarization $P_\perp$.

Spin-resolved ARPES

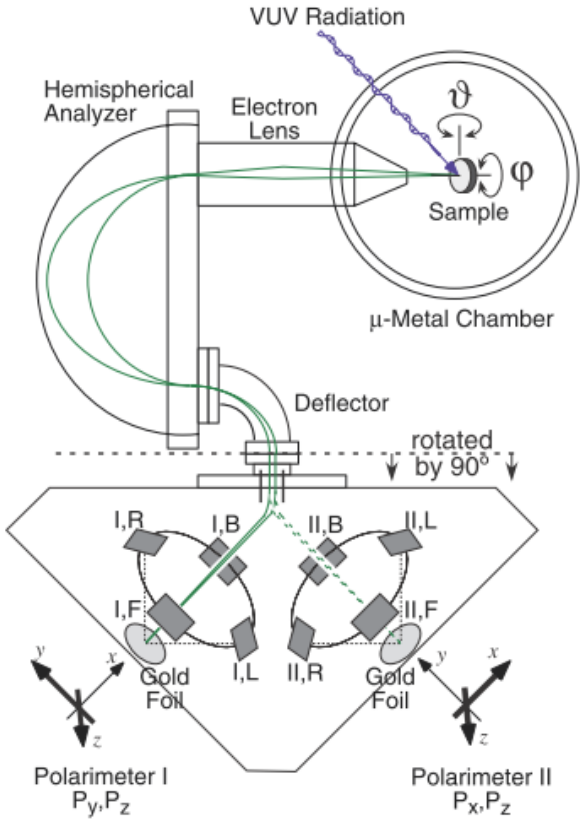

Fig. 5. Schematic view of the three-dimensional polarimeter [7]. Electrons that are photoemitted from a sample by ultraviolet radiation are energy and angle selected by an electrostatic analyzer and detected in two orthogonal Mott polarimeters (named polarimeter I and II). In an electrostatic beam deflection system the spin direction is conserved and polarimeter I measures the polarization components P_y and P_z, while polarimeter II measures P_x and P_z. The beam is switched between the two in order to allow quasi-simultaneous data collection. In the figure, the polarimeter system is shown rotated by 90° for graphical clarity, i.e. in reality the z axis is directed straight to the left and parallel to the electron lens of the spectrometer

SR-ARPES: example

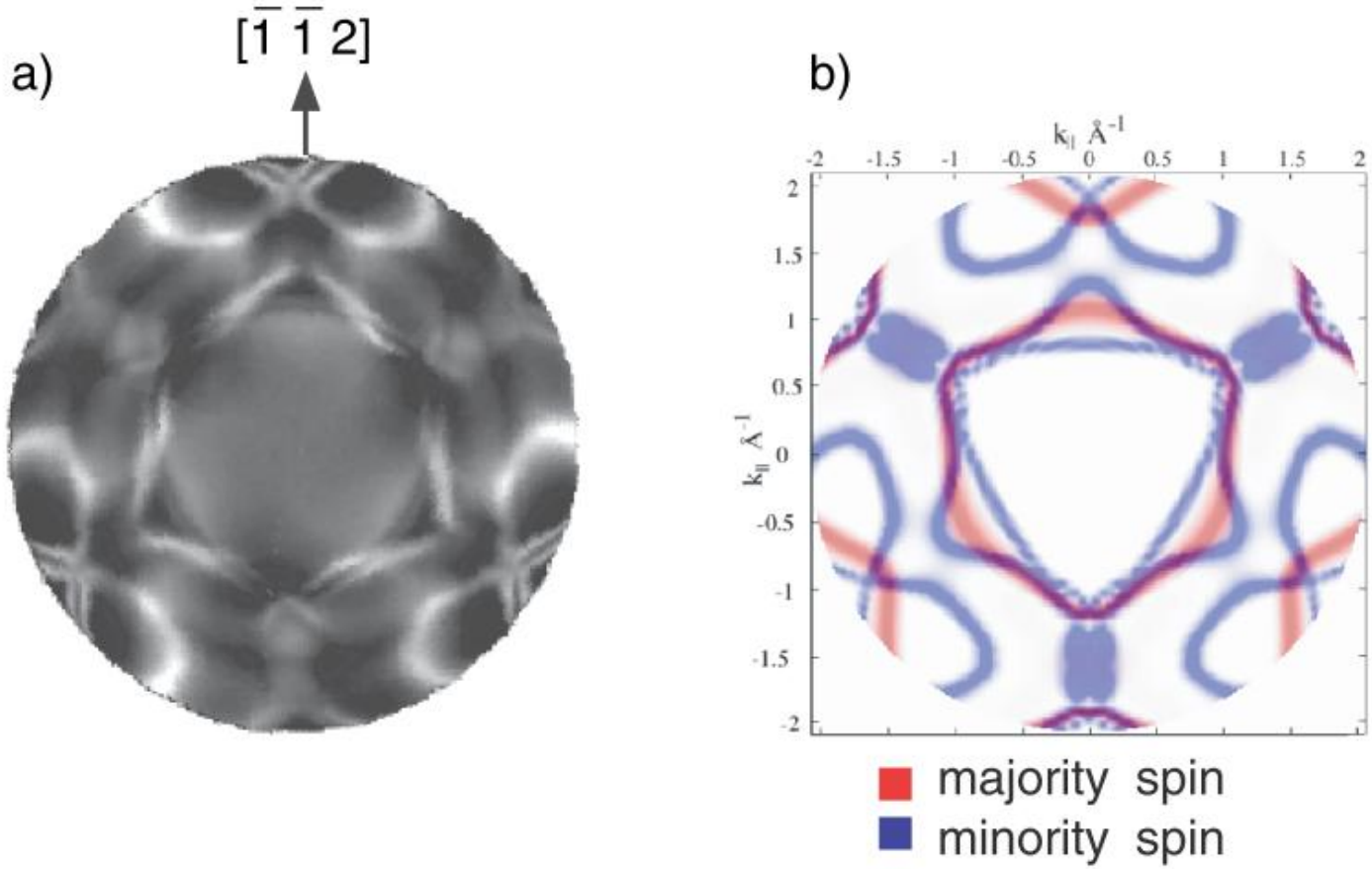

Fig. 2. (**a**) He Iα excited Fermi surface map ($h\nu = 21.21$ eV) from Ni(111). A $\boldsymbol{k}_{\parallel}$ projection of the raw data is presented in a linear grey scale, with highest intensities in white, lowest in black. In (**b**) the corresponding spin-polarized band structure calculation is displayed, showing Fermi level crossings at the same $\boldsymbol{k}_{\parallel}$ locations as in the measurement (a). Majority spin bands are shown in red, minority spin bands in grey (From [10], with improved experimental data by W. Auwärter)

Basic property

A <u>topological insulator</u> is an insulator
that always has a metallic surface state (SS)

Key properties:

- SS is topologically protected
- SS is spin-polarized

Today: Only 3D-TI, not Quantum Spin Hall effect (2D-TI)

Topologically trivial SS

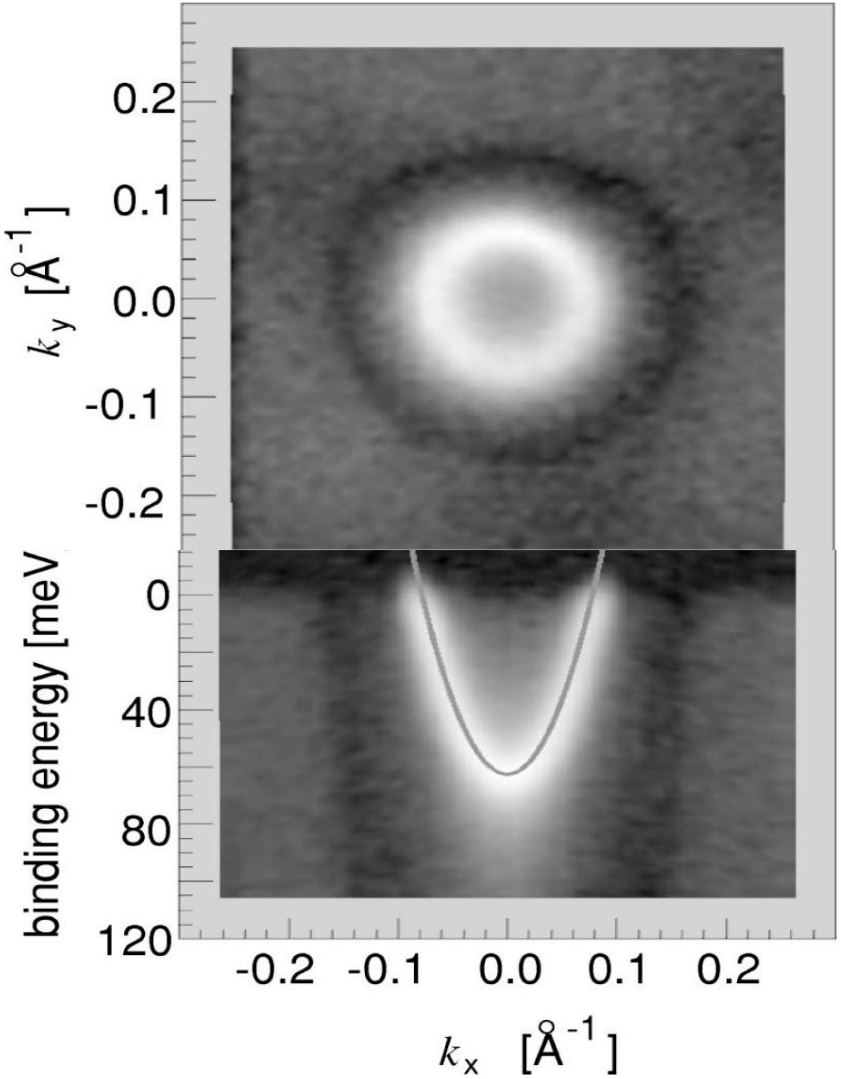

Ag(111)

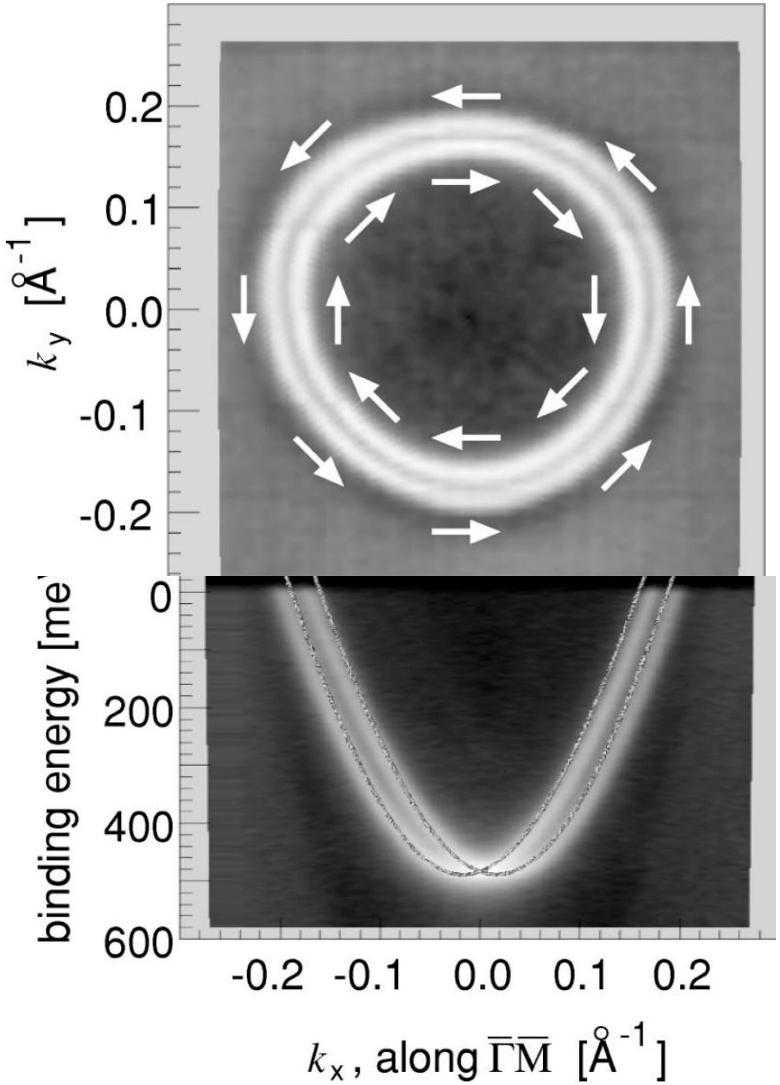

Au(111)

Experimental Example Bi_2Te_3

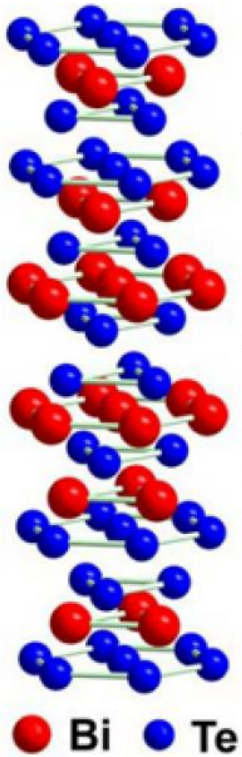

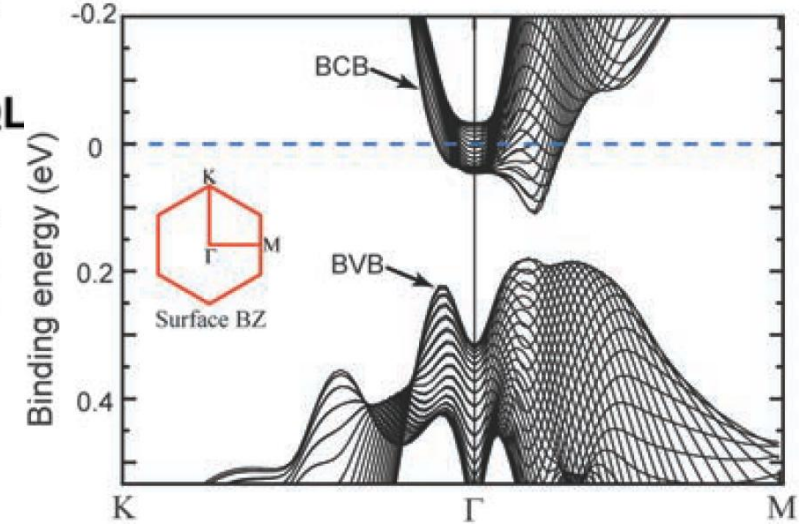

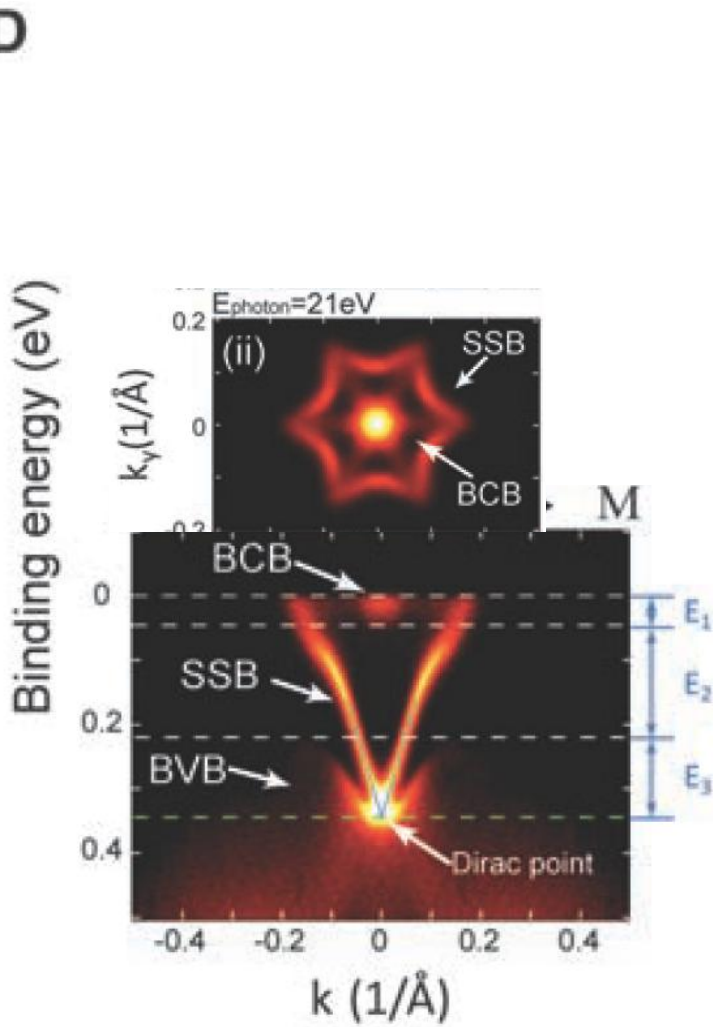

Surface state in a Topological Insulator

Bi2Te3: strong SOC

1.25 eV ≈ 2 · Au(111)

Exp. resolution sufficient to detect splitting for Au(111)

⇒degenerate surface state ruled out

but: where is the missing spin?

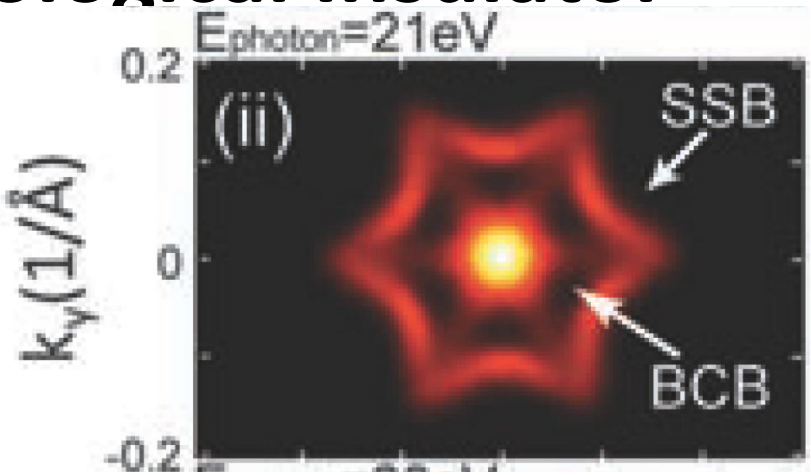

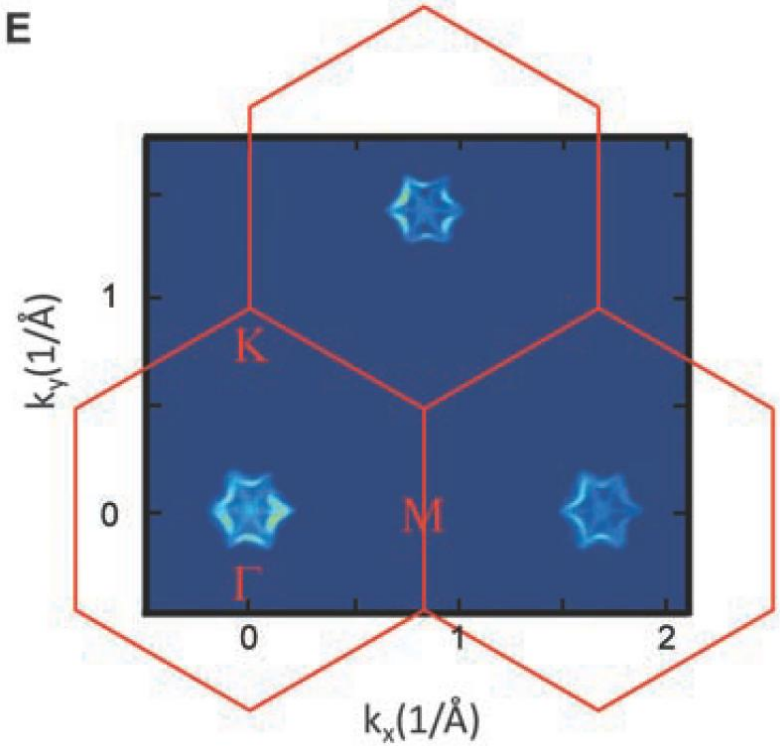

Spin-polarized Surface State

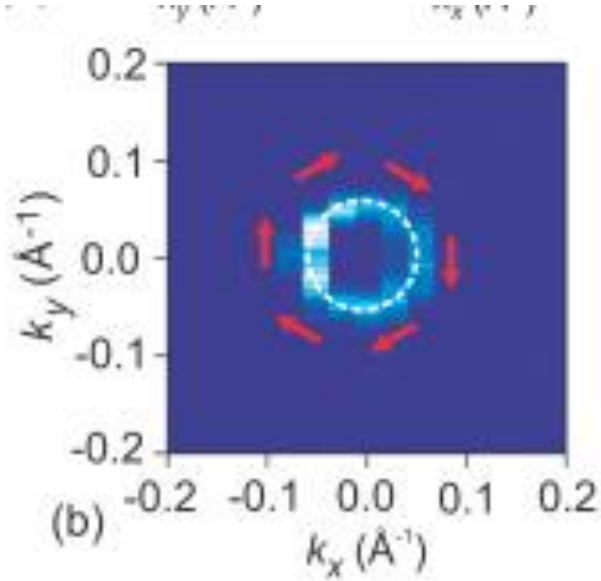

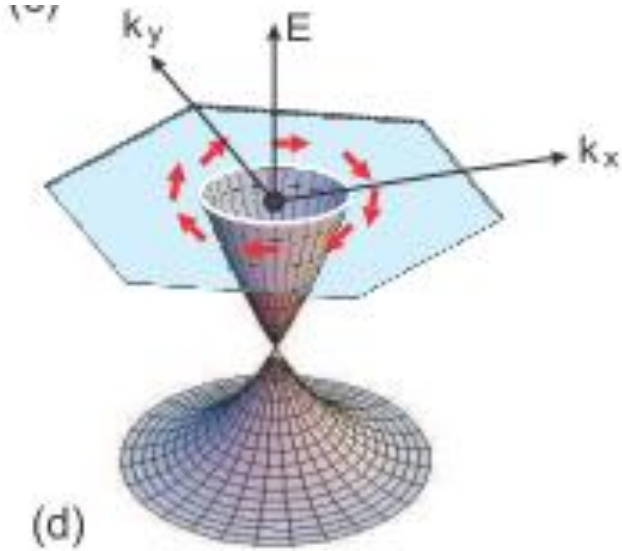

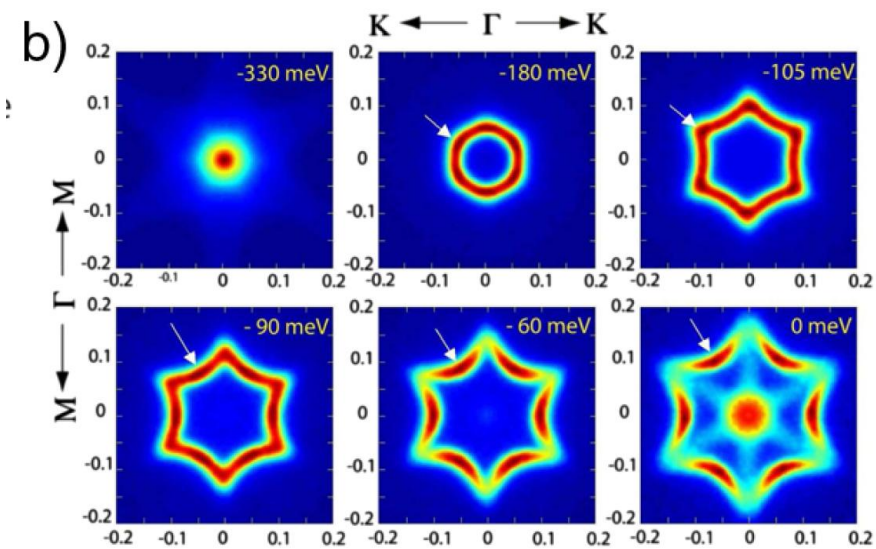

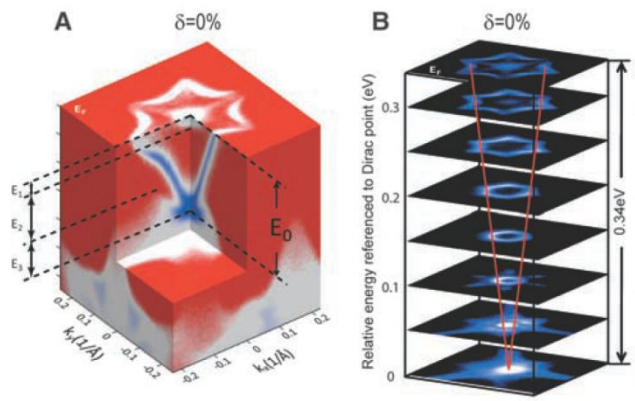

Topological foundation

ordinary insulator with spin-splitted surface state

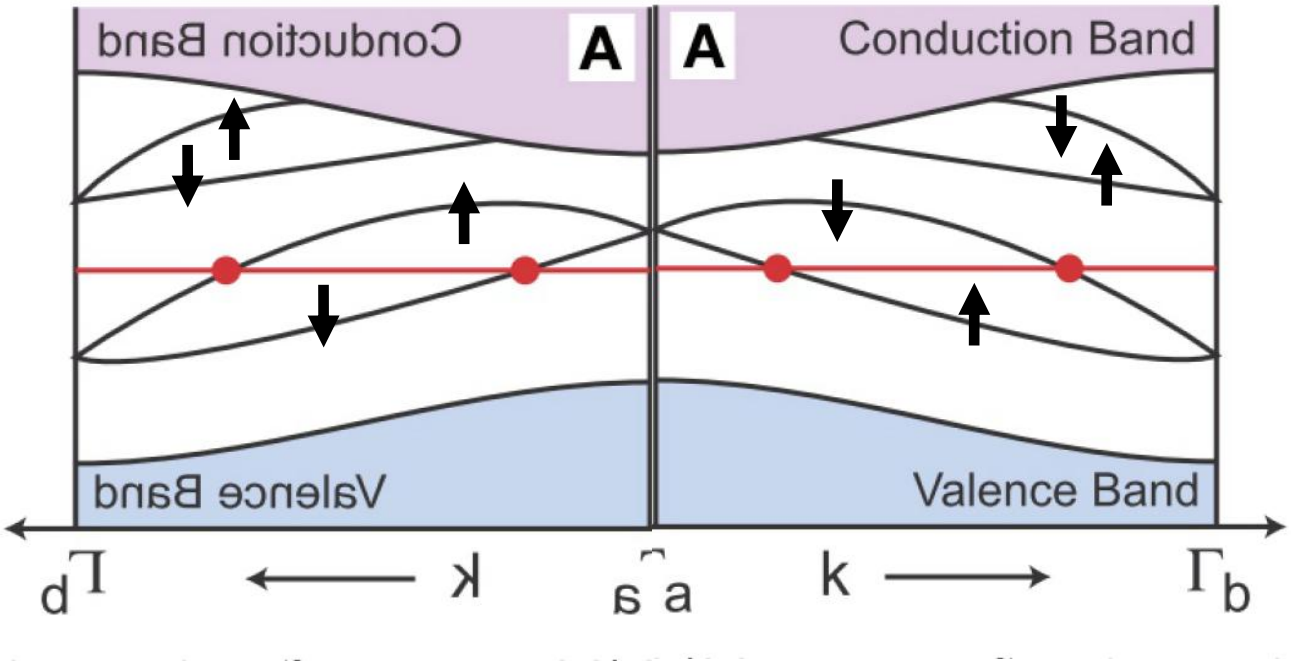

Kramers points

$$
\begin{aligned}
E(\mathbf{k},\uparrow) &\stackrel{!}{=} E(\mathbf{k},\downarrow)\,(\text{Forderung}) \\
&= E(\mathbf{k}-\mathbf{G},\downarrow)\,(\text{Translation}) \\
&= E(-\mathbf{k}+\mathbf{G},\uparrow)\,(\text{Zeitumkehr}) \\
\Rightarrow\ \mathbf{k} &= \frac{\mathbf{G}}{2}.
\end{aligned}
$$

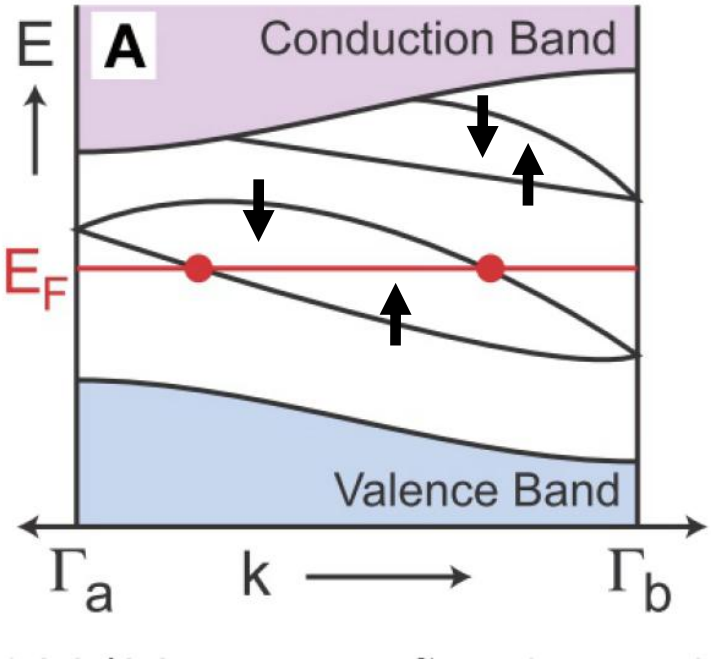

Connection of TRI

Topology: how are two TRI connected?

- pairwise: trivial insulator
- not pairwise: topological insulator

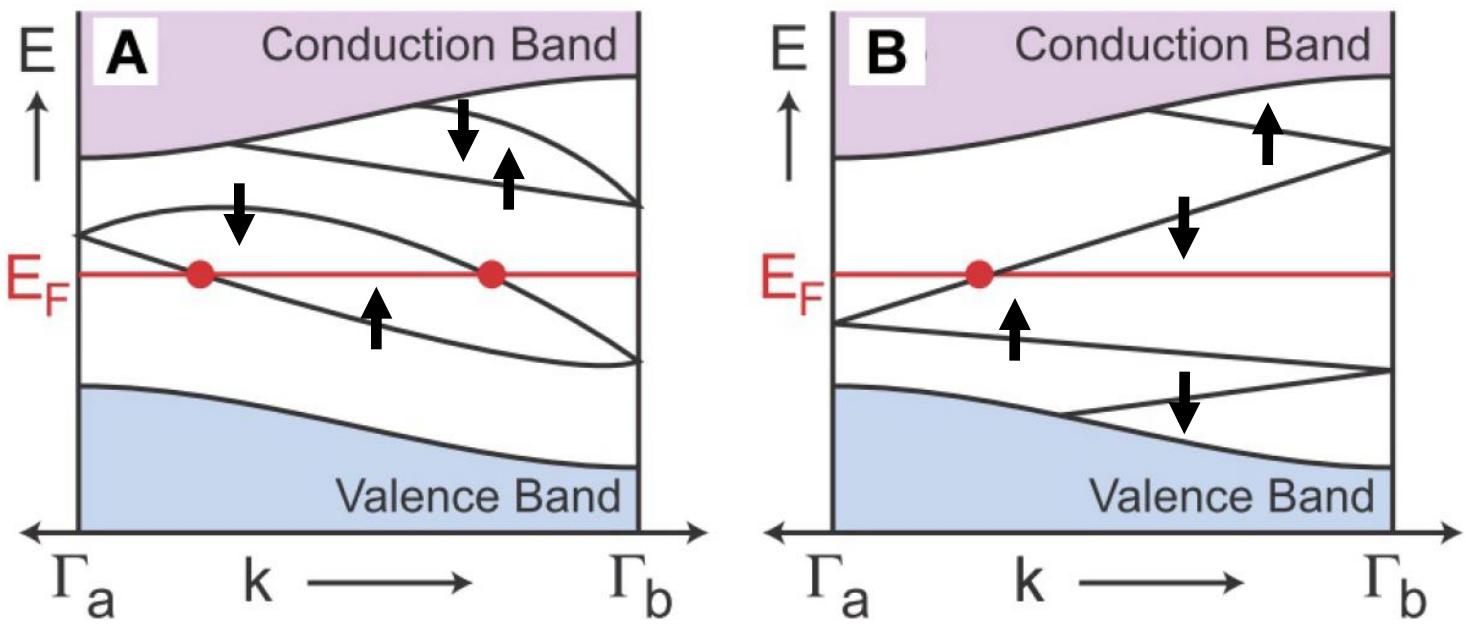

trivial insulator **topological insulator**

Topological protection

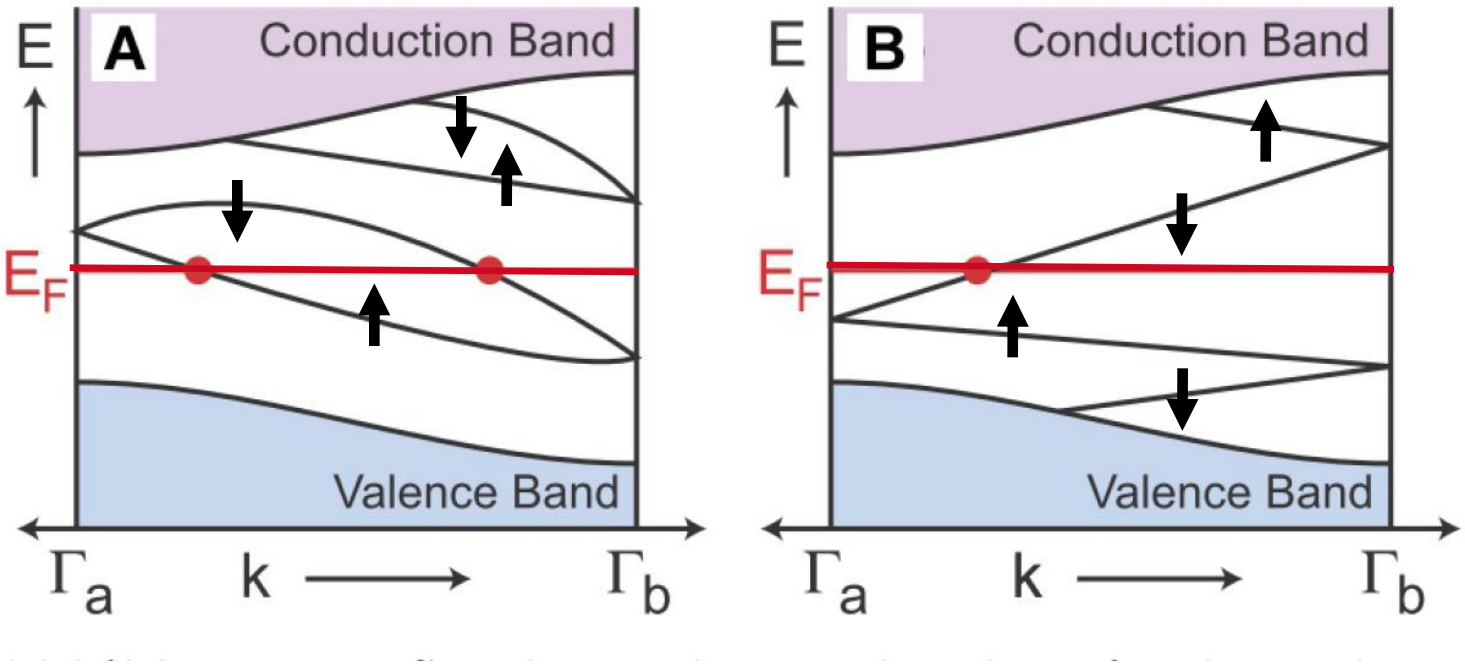

trivial insulator **topological insulator**

Main message

spin-polarized surface state

surface state is topologically protected

Topology

Topology deals with properties of geometric objects that remain unchanged by a homeomorphism (continuous function with continuous inverse function)

Analogon: 2D-Surfaces

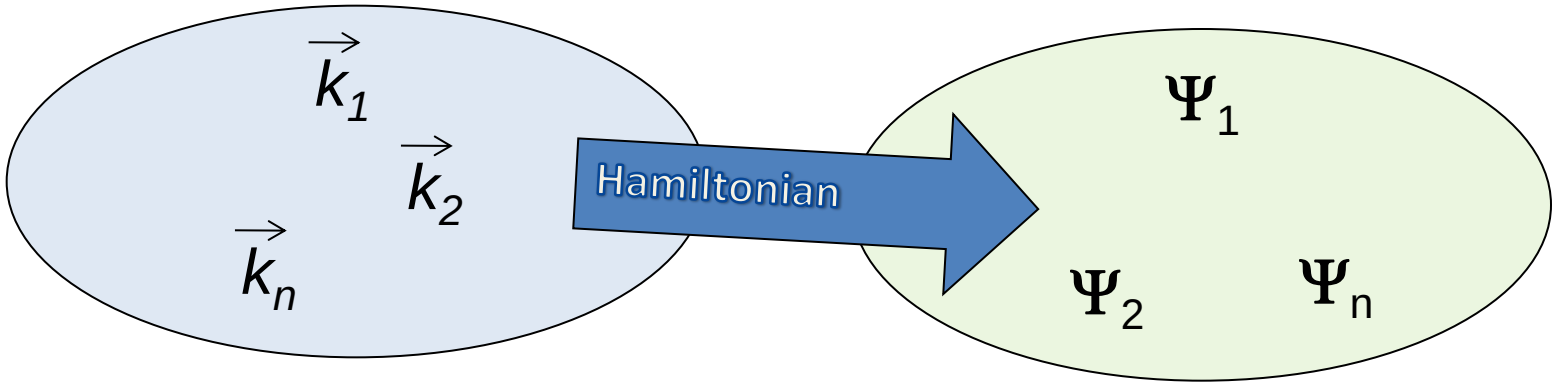

Brillouin-Zone $\mathbb{R}^3$

Hilbert-Space $\mathcal{H}$

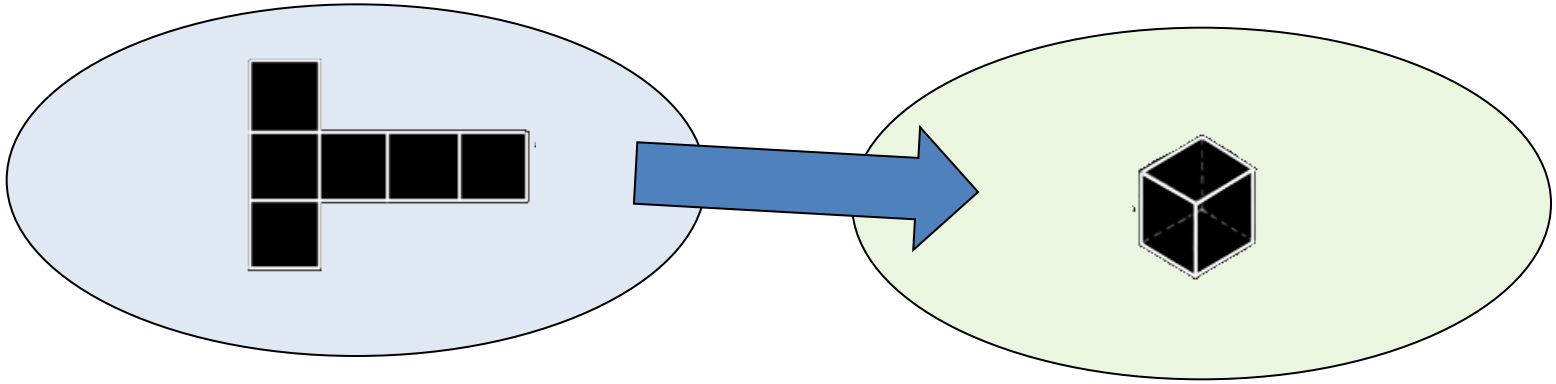

Plane $\mathbb{R}^2$

Space $\mathbb{R}^3$

Genus

Euler characteristics:

Cube:

Corners – Edges + Faces

8 – 12 + 6 = 2

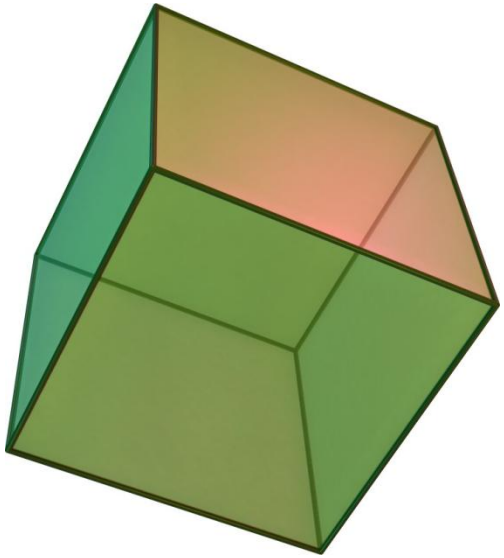

Cube with hole:

(8+8) – (12+20) + (6+10)

= 2- 2

= 2-2 *g*

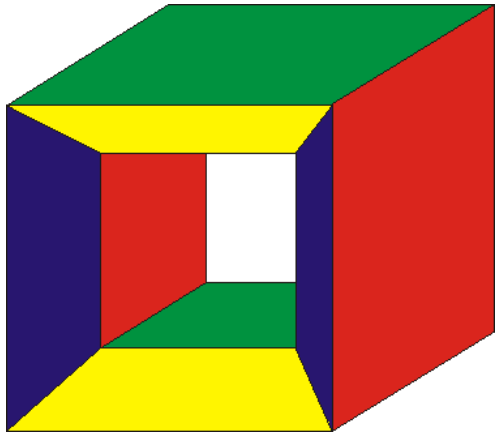

***g*: genus, here the number of holes**

Topology of bands

- time-reversal invariant band-structures with gap
- topological invariant: band-structures that can be continuously transformed into each other, especially without closing the gap
- conventional isolators are all topologically equivalent (including the vacuum)
- turned around: two bandstructures from <u>different</u> topological classes <u>can not</u> be transformed into each other without closing the band gap
- generate interface between materials with different invariants (e.g. topological insulator/vacuum)
- bandgap has to vanish at interface → metallic surface states

Topological invariant

$\mathbb{Z}_2$ invariant ν_0 determines wether the surface Fermi line encloses an odd or an even number of Kramers points

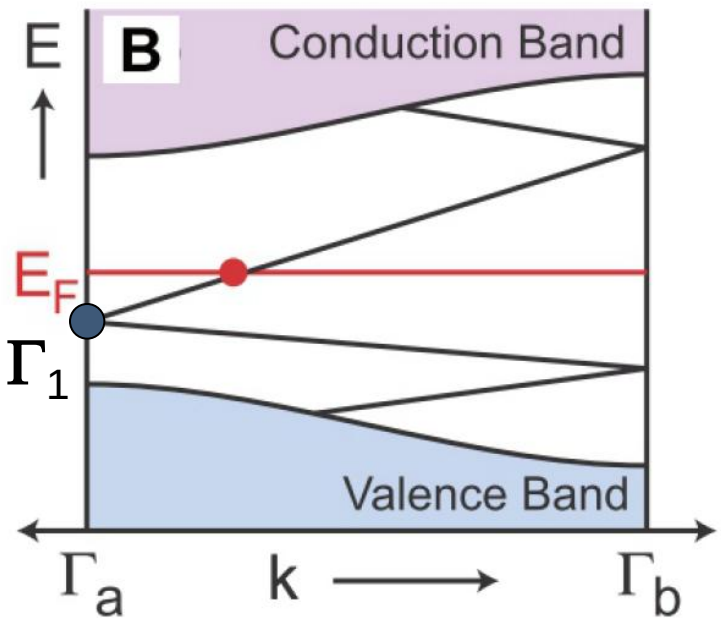

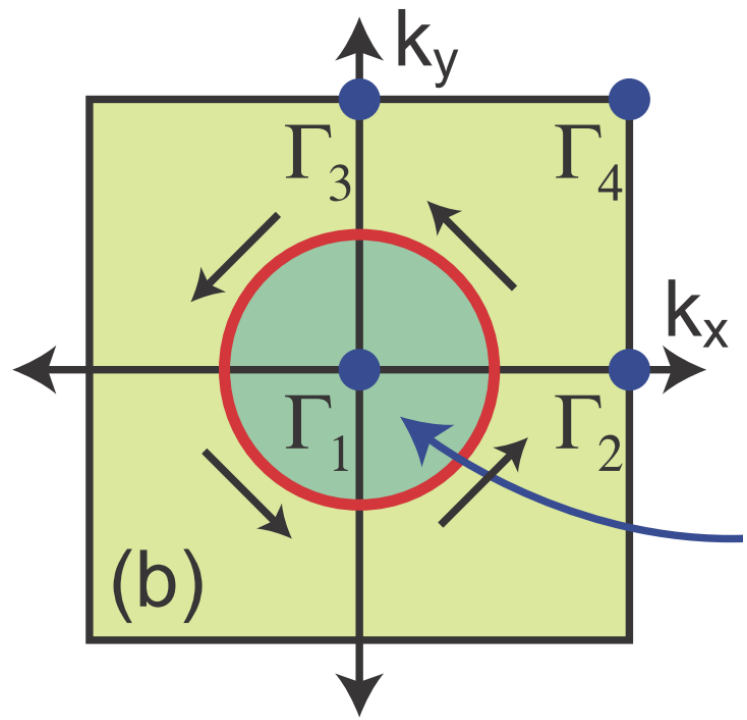

SP-ARPES on Bi_2Se_3

PHYSICAL REVIEW B **84**, 165113 (2011)

Widespread spin polarization effects in photoemission from topological insulators

C. Jozwiak,[1,*] Y. L. Chen,[1,2,3] A. V. Fedorov,[1] J. G. Analytis,[2,3] C. R. Rotundu,[4] A. K. Schmid,[4] J. D. Denlinger,[1] Y.-D. Chuang,[1] D.-H. Lee,[4,5] I. R. Fisher,[2,3] R. J. Birgeneau,[4,5,6] Z.-X. Shen,[2,3] Z. Hussain,[1,†] and A. Lanzara[4,5,‡]

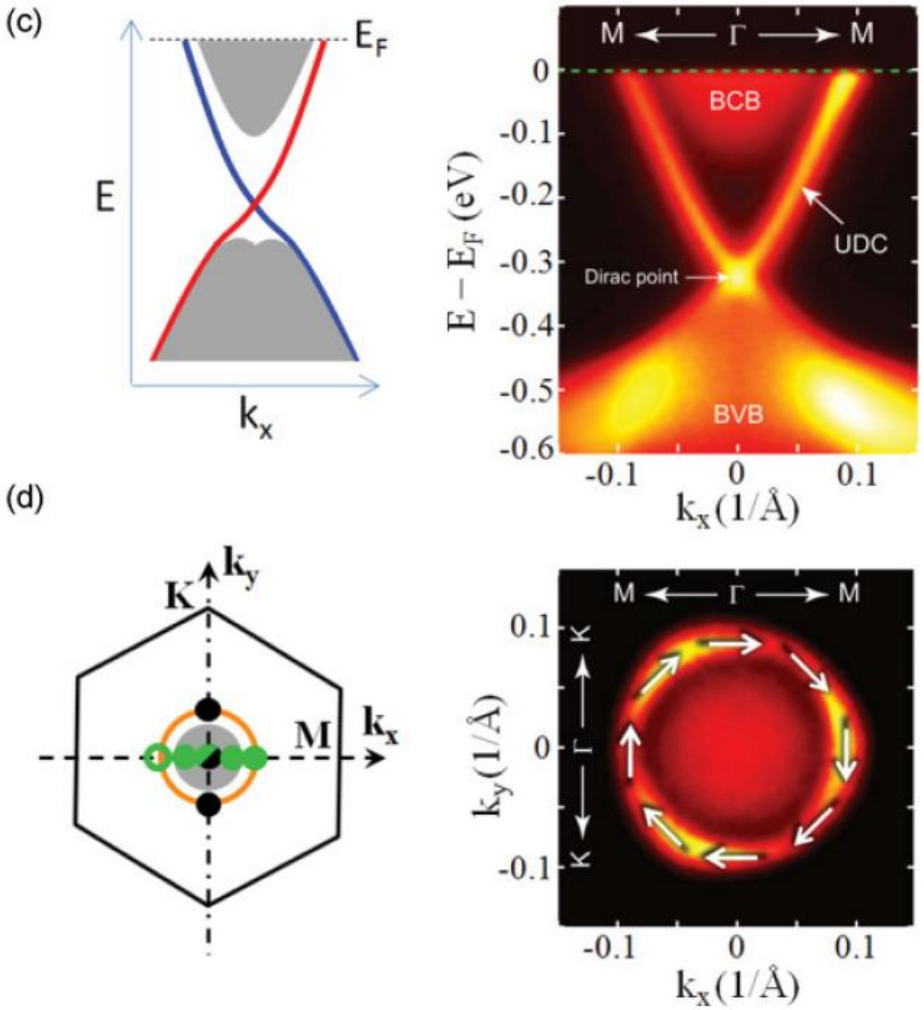

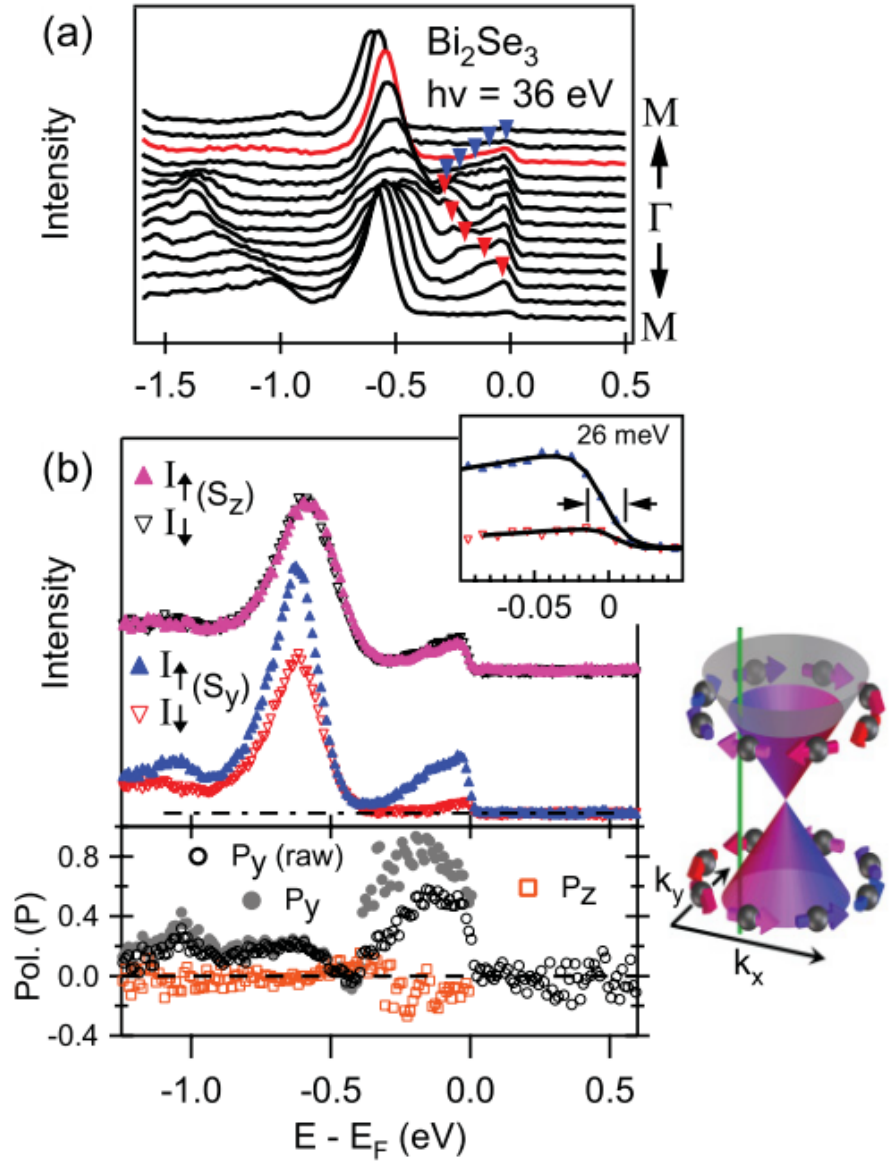

Spin-SEM
(SEMPA – SEM with polarization analyser)

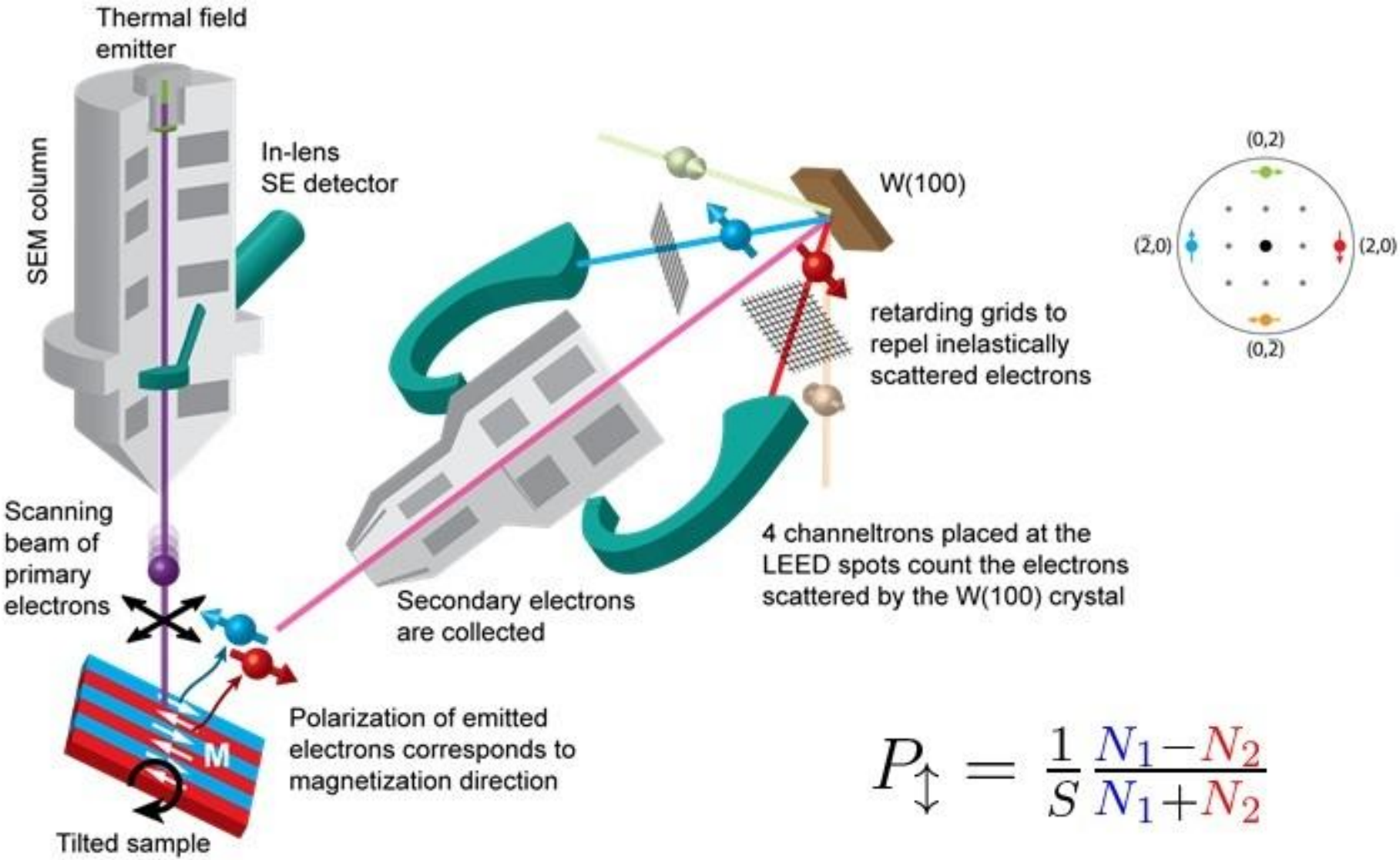

$$P_{\updownarrow} = \frac{1}{S}\frac{N_1 - N_2}{N_1 + N_2}$$

Application of Spin-SEM (AG Oepen – Hamburg)

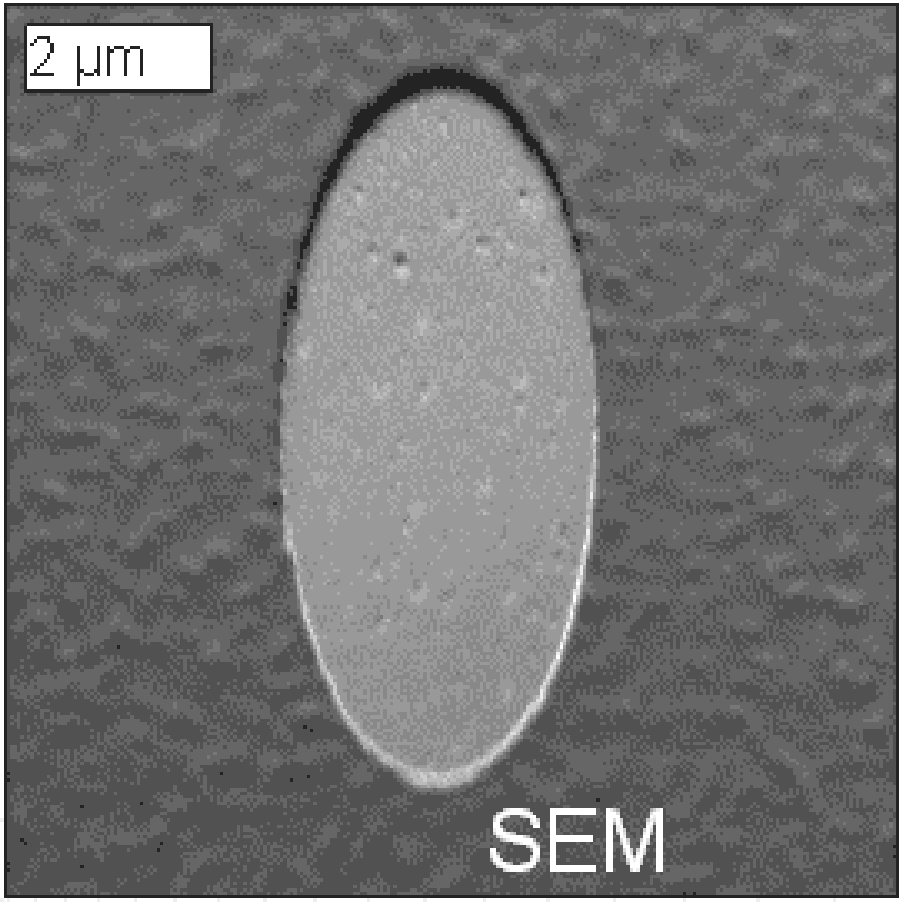

Spin-SEM Aufnahme der Domänenstruktur einer 20nm dicken Permalloy-Ellipse

NMR experiment

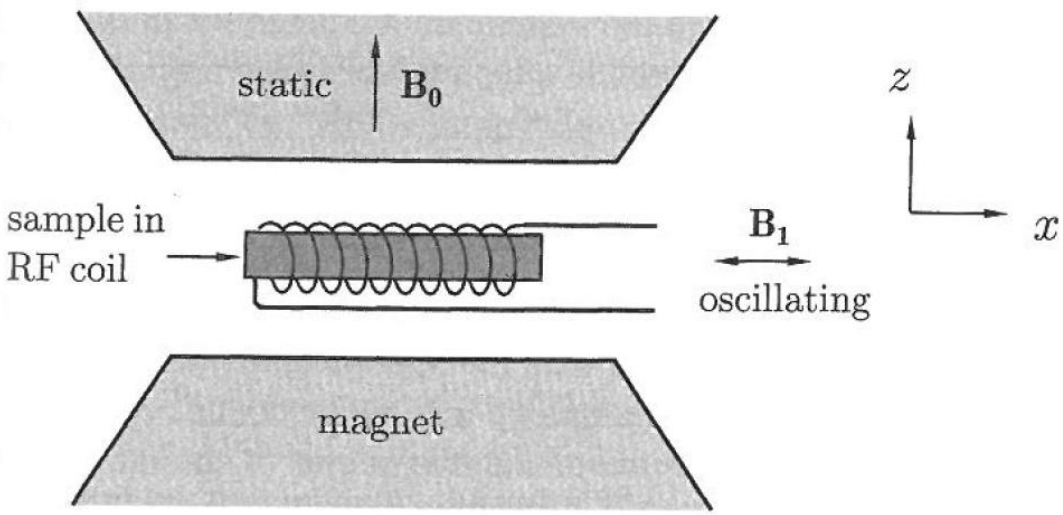

Fig. 3.9 Schematic diagram of an NMR experiment. The sample sits inside a radio frequency (RF) coil which produces an oscillating RF field. A highly homogenous static magnetic field is provided by a magnet. The static field $\mathbf{B}_0$ and the oscillating field $\mathbf{B}_1$ are perpendicular to each other. In a real experiment, the sample would be much smaller than is shown here so that it experiences a uniform field from the RF coil.

Zeeman splitting

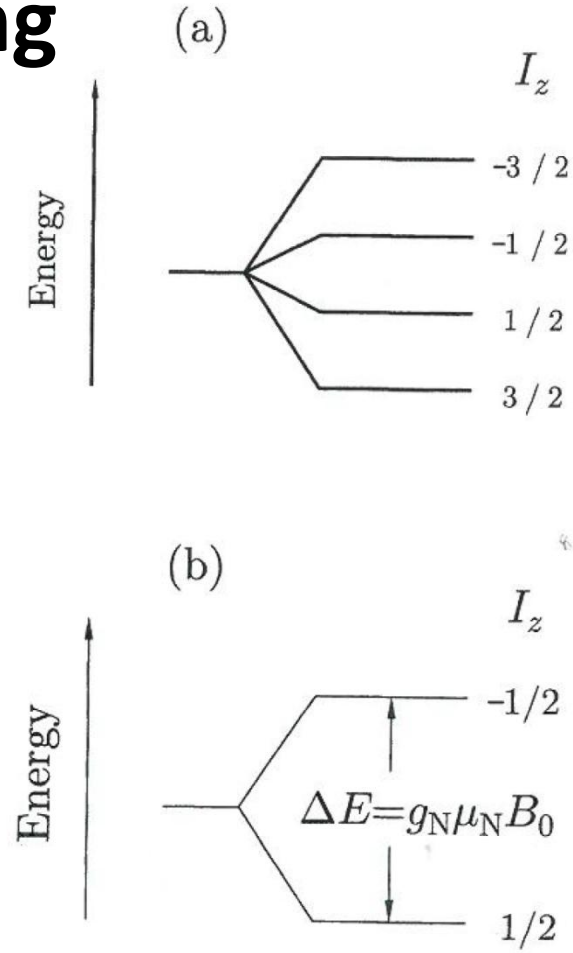

Fig. 3.10 (a) The four levels from an $I = \frac{3}{2}$ nucleus. (b) In the simpler case of an $I = \frac{1}{2}$ nucleus, there are just two levels. These two nuclear levels are separated by an energy $\Delta E = g_N \mu_N B_0$; the lower (upper) level corresponds to the nuclear magnetic moment lying parallel (antiparallel) to the magnetic field B_0.

MNR example: Graphite oxide

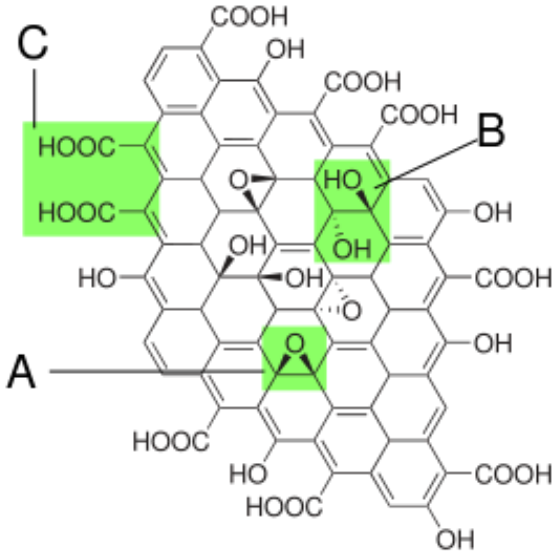

www.wikipedia.de

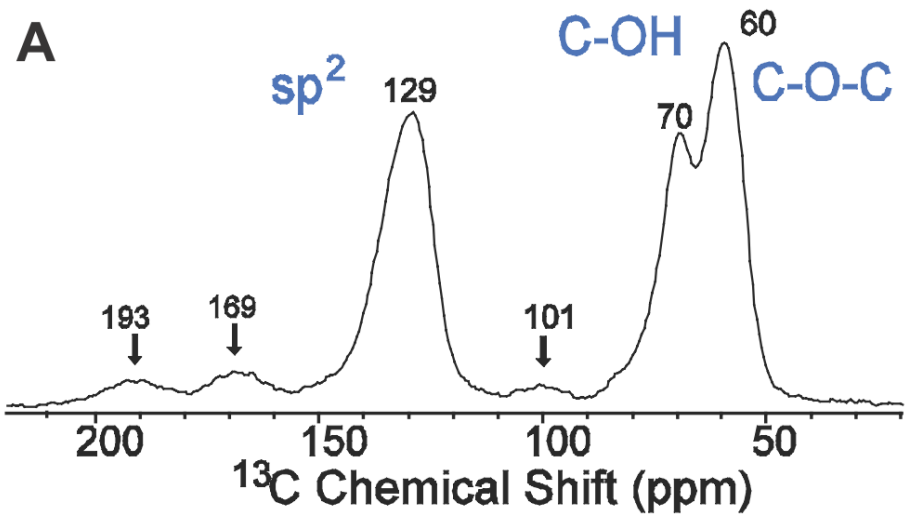

W. Cai et al., Science 1815 (2008); 321

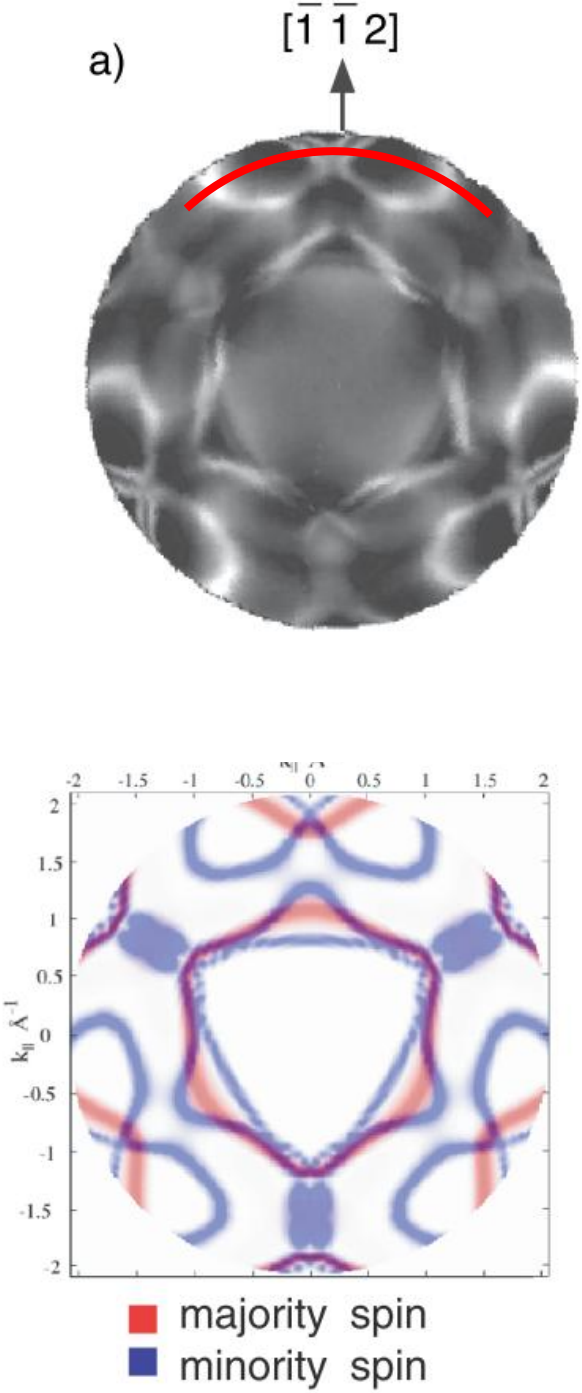

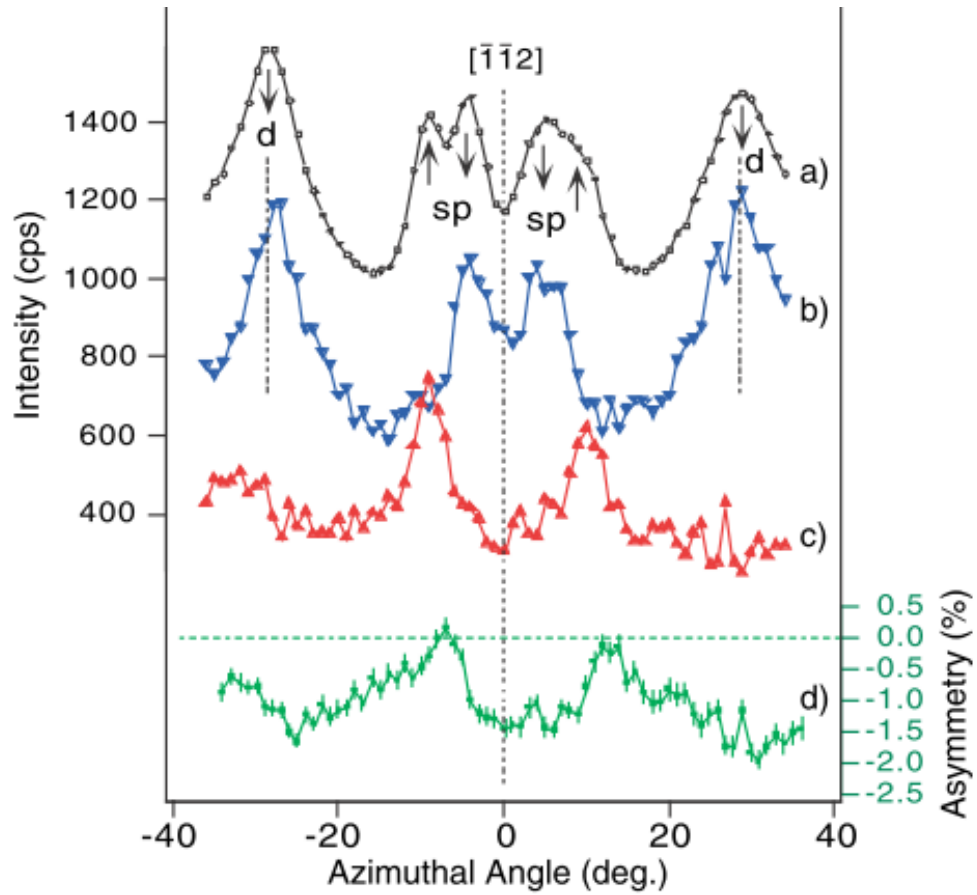

Fig. 6. (**a**) He Iα excited and spin-integrated intensity scan measured at the Fermi energy on Ni(111) along a path near the upper edge of Fig. 2a, producing an azimuthal momentum distribution curve. The peaks are annotated by their known orbital and spin assignment. Curves (**b**) and (**c**) present the spin-resolved minority and majority spin spectra, respectively, as obtained from curves (a) and (**d**) by applying (2). Curve (d) is the spin asymmetry for the polarization component measured along the sample magnetization direction (from [7]). See text for a discussion of quantitative aspects

ESR experiment

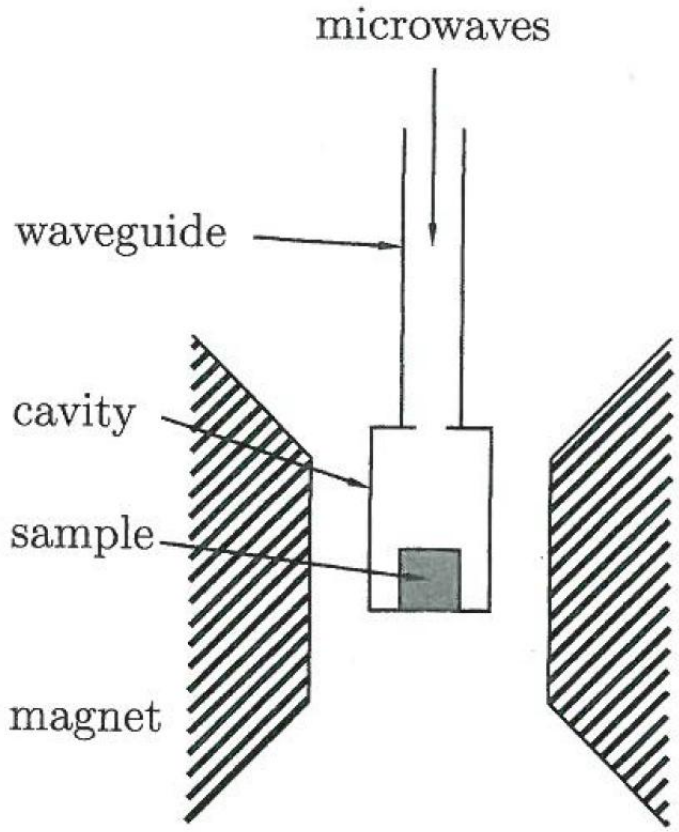

Fig. 3.14 Schematic diagram of an ESR experiment. Microwaves enter a cavity via a waveguide and the absorption of microwaves induced by a resonance is measured by monitoring the Q-factor of the cavity. The sample must be placed in the centre of the magnet, where the field is most clearly uniform.

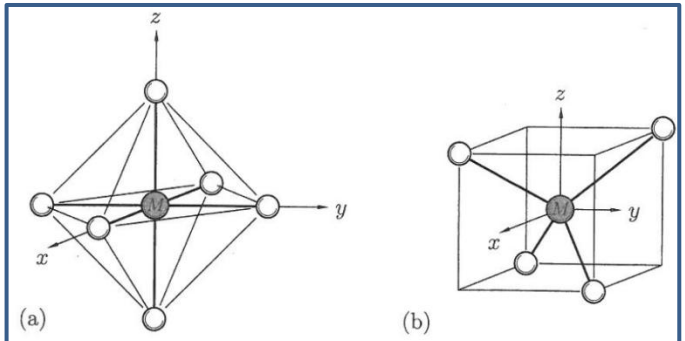

Fig. 3.2 A metal atom M in an (a) octahedral and (b) tetrahedral environment. The octahedral environment is found in many transition metal oxides where oxygen anions sit on the corners of an octahedron with the metal atom at the centre. The tetrahedral environment can be conveniently described by considering alternate corners of a cube as shown.

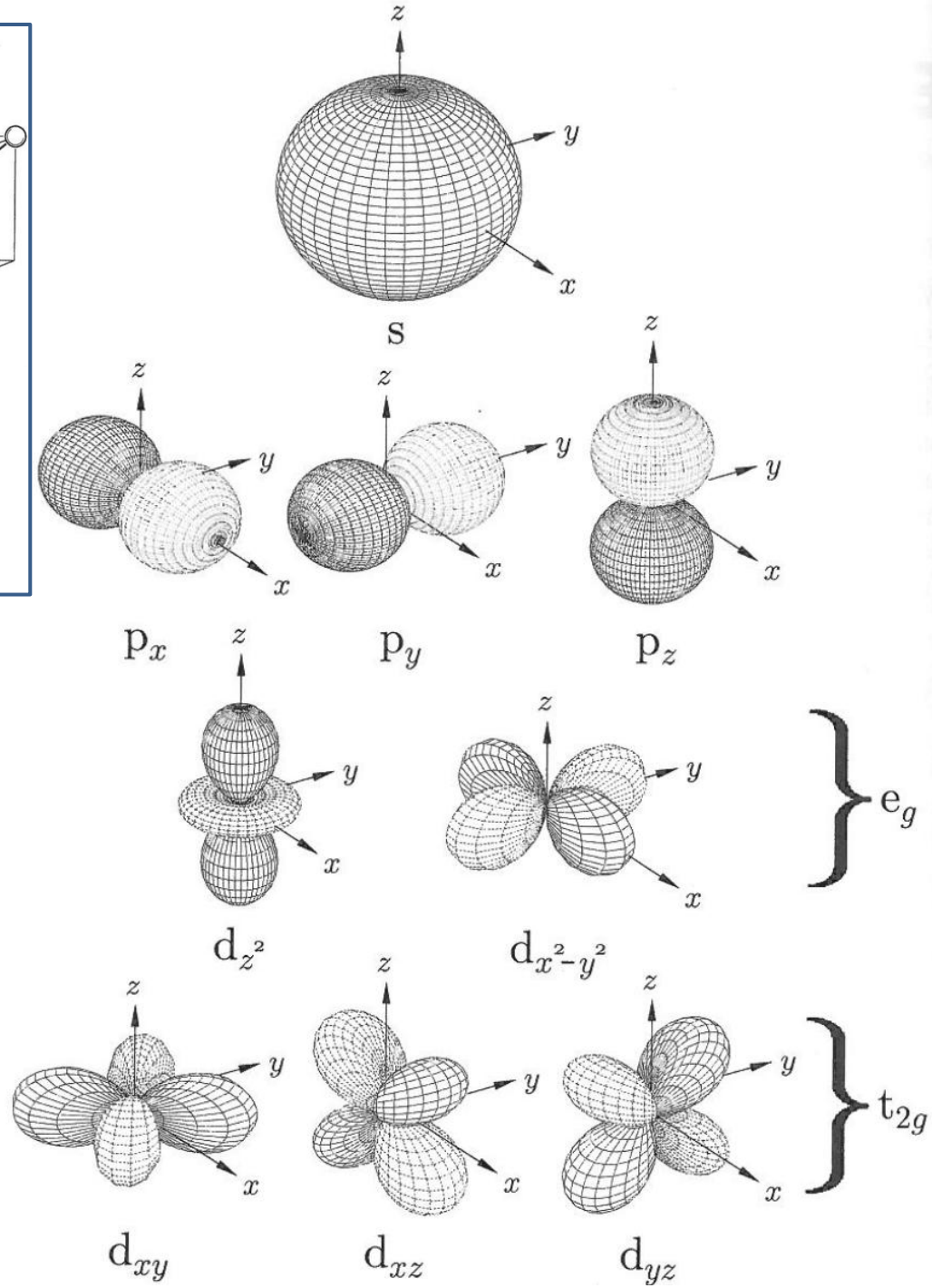

Fig. 3.1 The angular distribution of the s, p and d orbitals. The d_{z^2} and $d_{x^2-y^2}$ levels are grouped together and called the e_g levels. The d_{xy}, d_{xz} and d_{yz} levels are grouped together and called the t_{2g} levels. The d_{z^2} orbital is sometimes referred to as $d_{3z^2-r^2}$.

Crystal field splitting

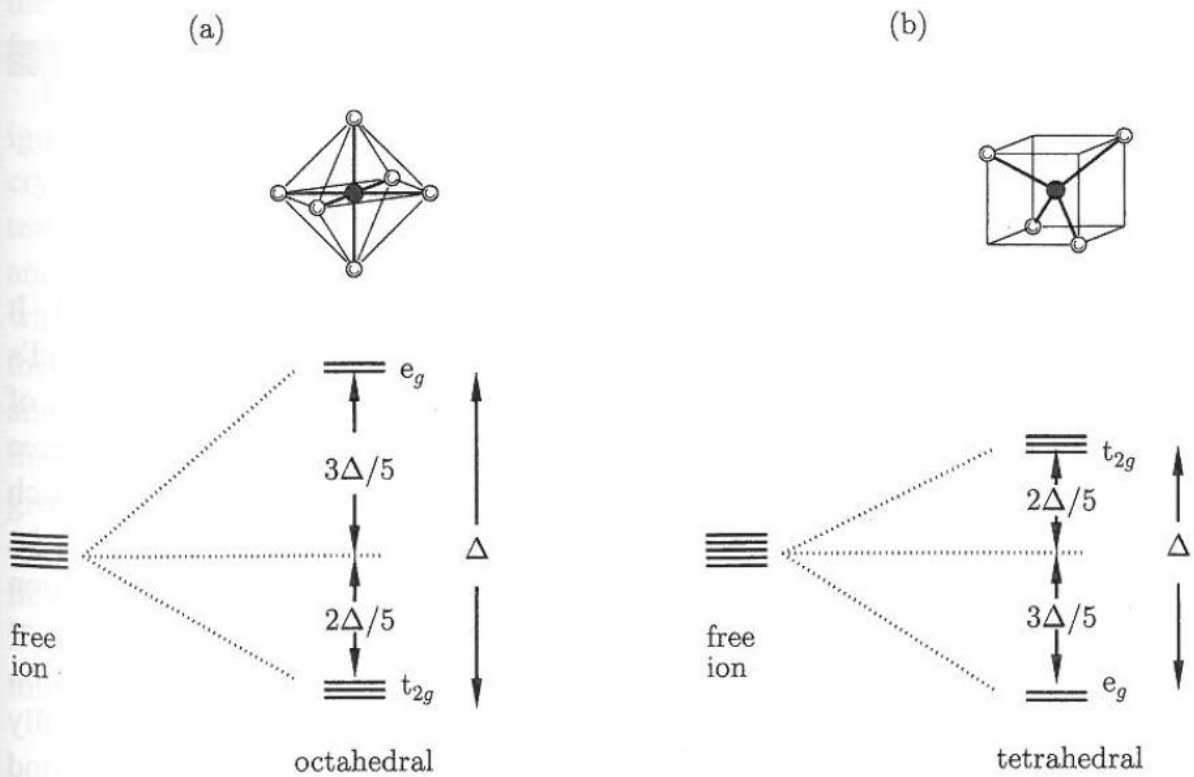

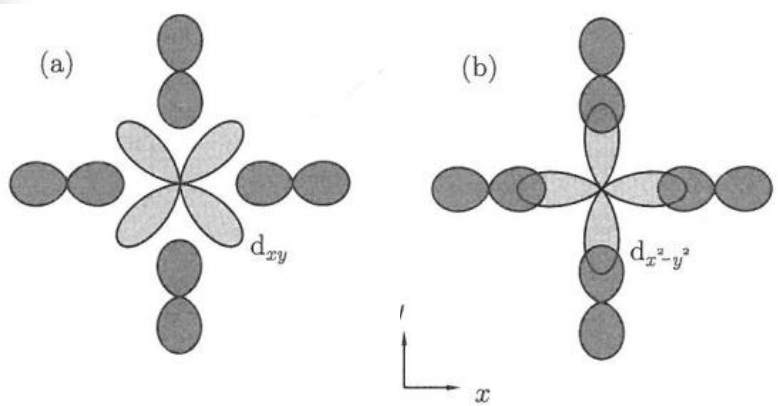

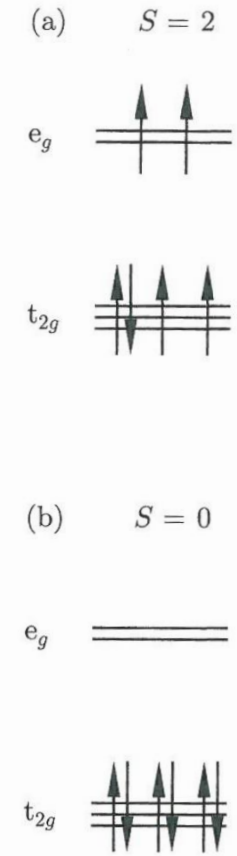

Fig. 3.5 Electronic configurations for the (a) high-spin (weak-field) and (b) low-spin (strong-field) cases for a $3d^6$ ion, e.g. Fe^{2+}.

ESR schematics

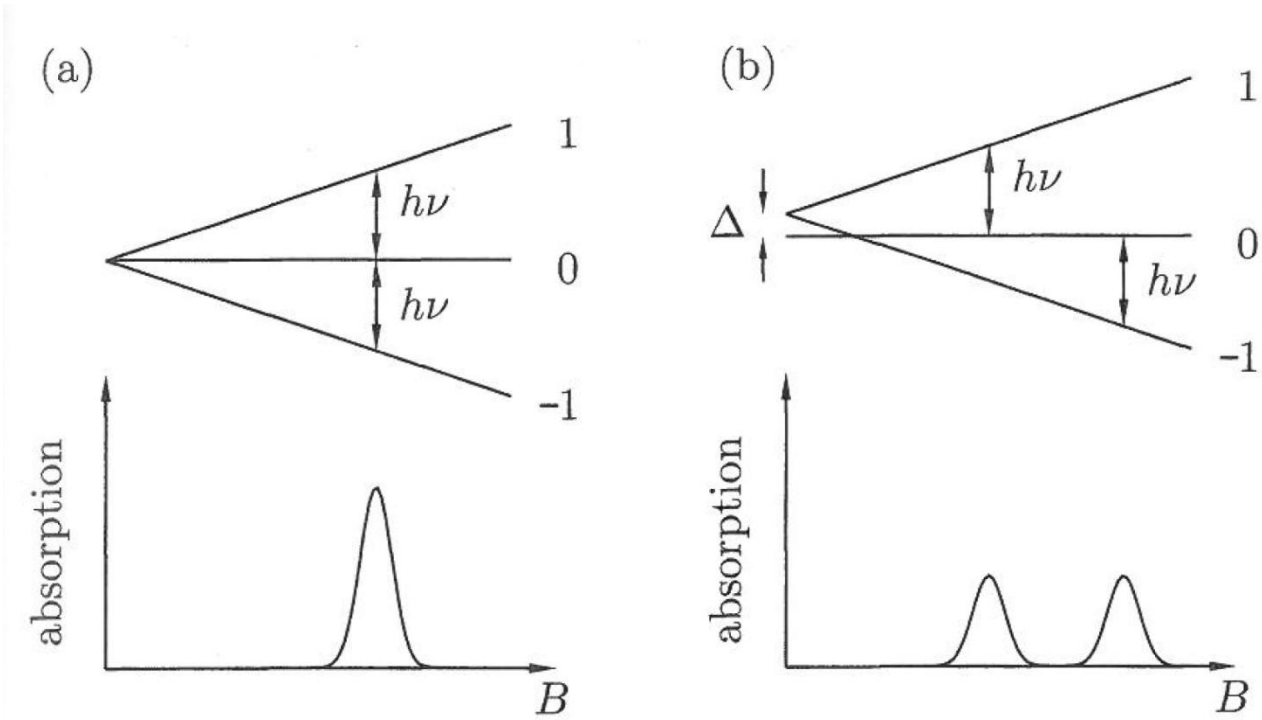

Fig. 3.15 ESR in an ion with $J = 1$ such as Ni^{2+} with (a) no crystal field splitting (leading to a single ESR line) and (b) crystal field splitting Δ (leading to two ESR lines).

Jahn-Teller effect

$$E(Q) = \pm AQ + \frac{1}{2}M\omega^2 Q^2,$$

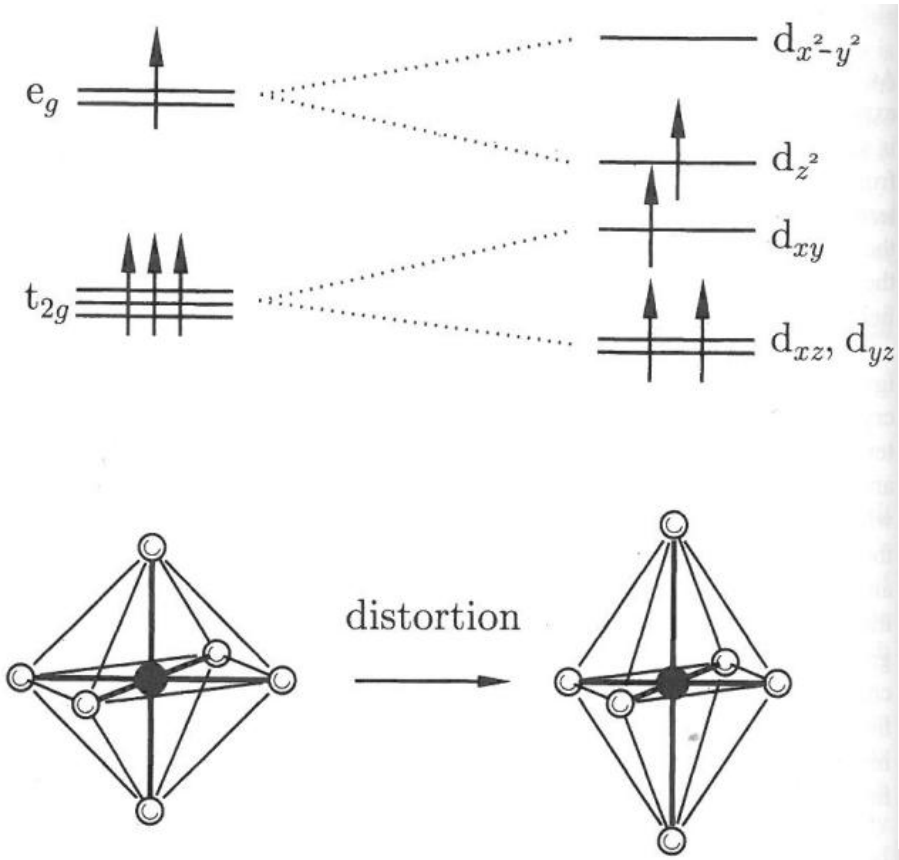

Fig. 3.6 The Jahn–Teller effect for Mn^{3+} ($3d^4$). An octahedral complex (left) can distort (right), thus splitting the t_{2g} and e_g levels. The distortion lowers the energy because the singly occupied e_g level is lowered in energy. The saving in energy from the lowering of the d_{xz} and d_{yz} levels is exactly balanced by the raising of the d_{xy} level.

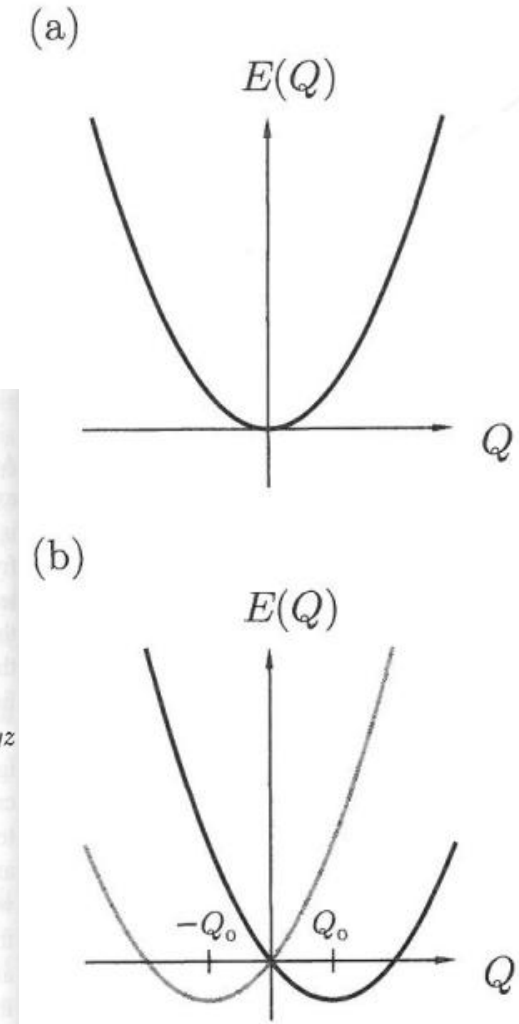

Fig. 3.7 (a) The energy of an octahedral complex as a function of the distortion Q according to eqn 3.3. (b) The energy of an octahedral complex as a function of the distortion Q according to eqn 3.4.

ESR example: $CuSO_4 \cdot 5\ H_2O$

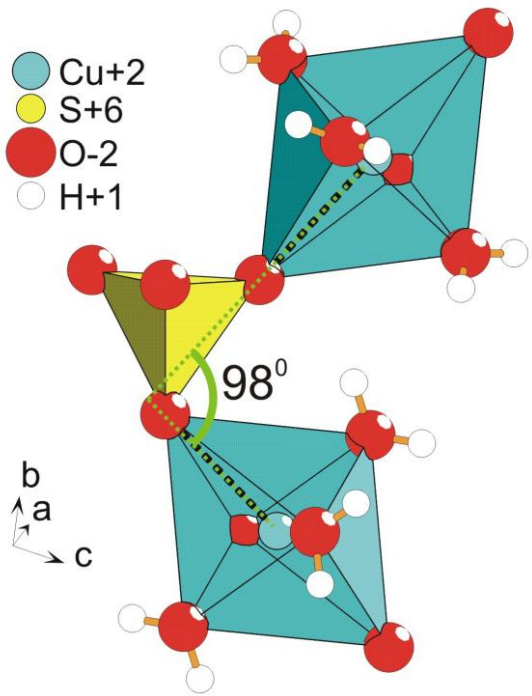

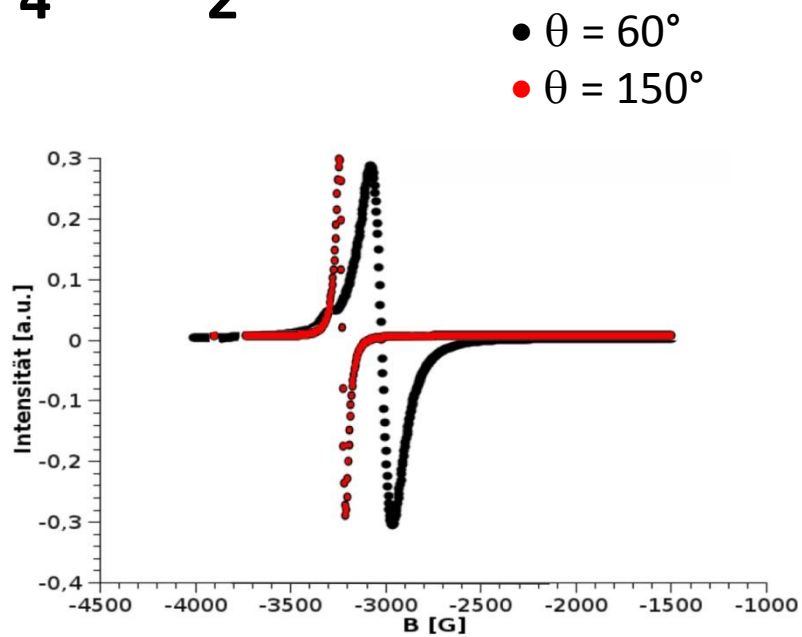

$Cu2^+$:$1s^2 2s^2 2p^6 3s^2 3p^6 3d^9$

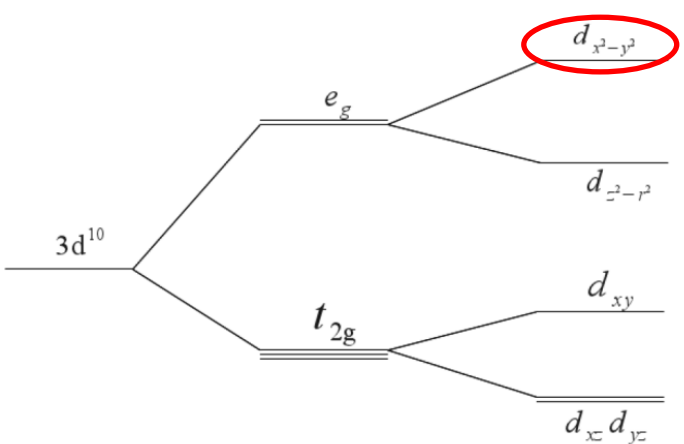

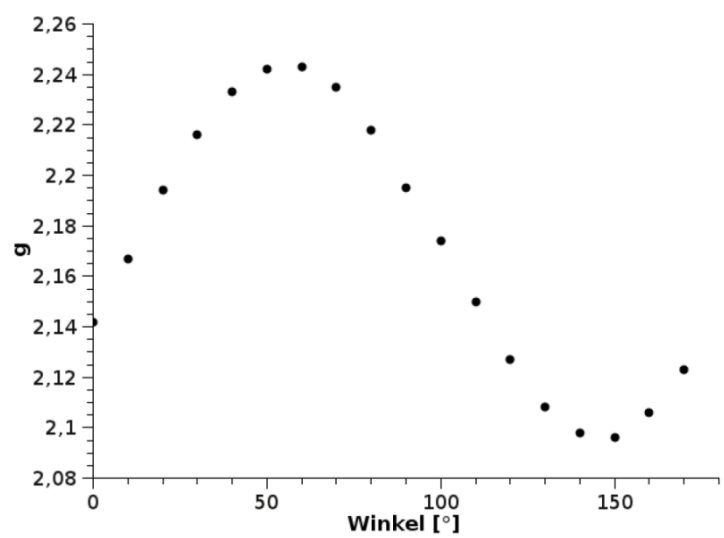

Thermodynamic variables and functions

1 … heat of magnetization
2 … heat of deformation
3 … magneto-volume effect
4 … magnetic susceptibility
5 … magnetocaloric effect
6 … forced magnetostriction
7 … heat capacity
8 … thermal magnetization
9 … thermal expansion
10 … compressibility
11 … converse magnetostriction
12 … piezocaloric effect

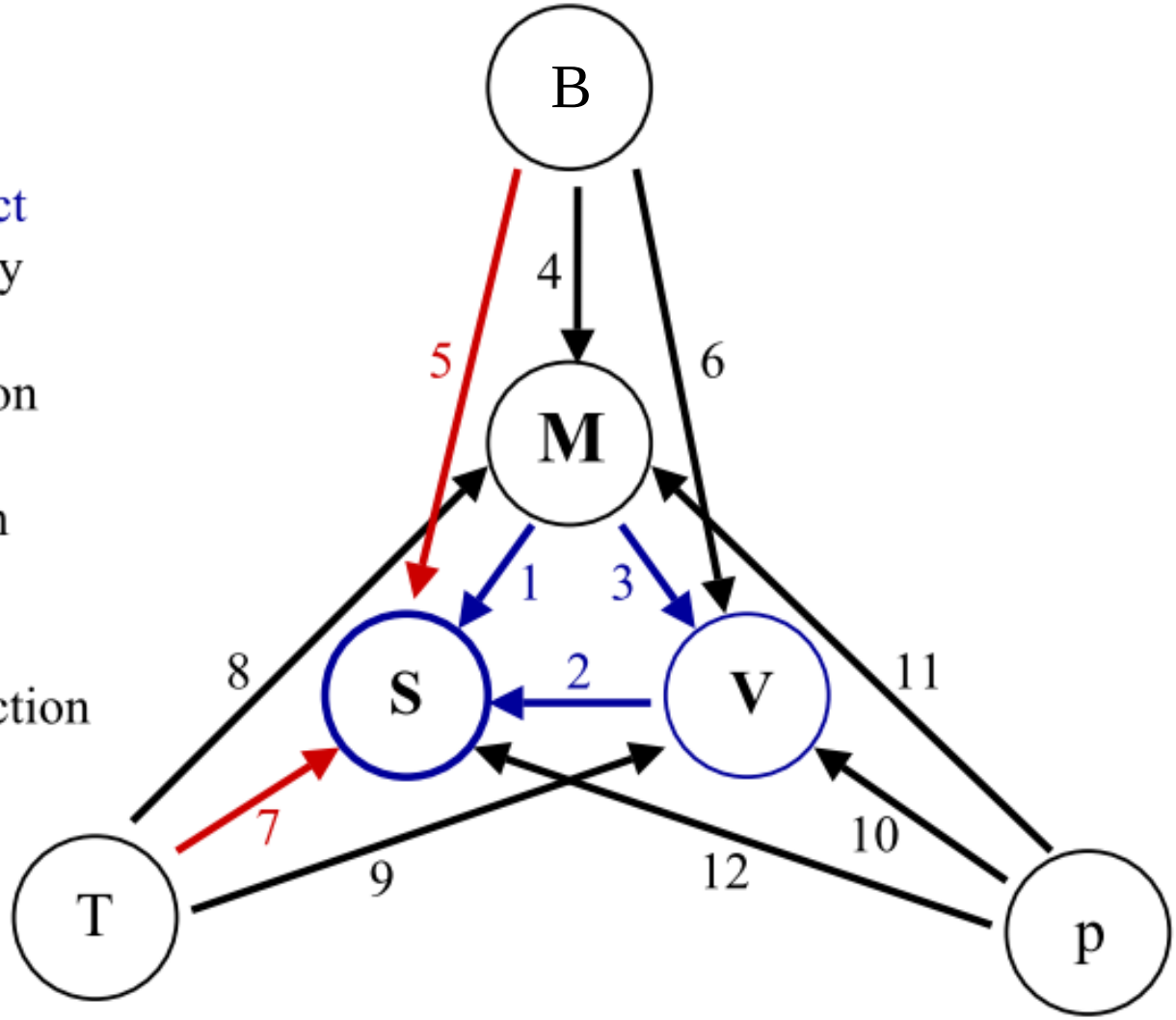

H. Michor, TU Wien

Historic dilatometer

Paris, 1810

Methods

Methods	Sensitivity
X-ray diffraction	10^{-5}
Neutron diffraction	10^{-5}
Capacitive dilatometry	10^{-9}
Strain gauge	10^{-7}

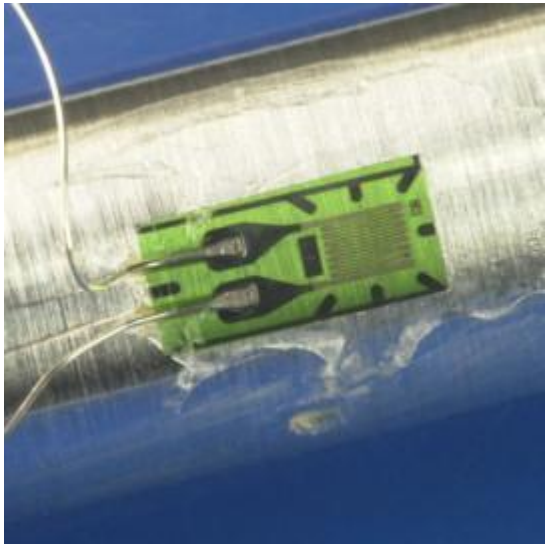

Strain gauge

Capacitive dilatometer

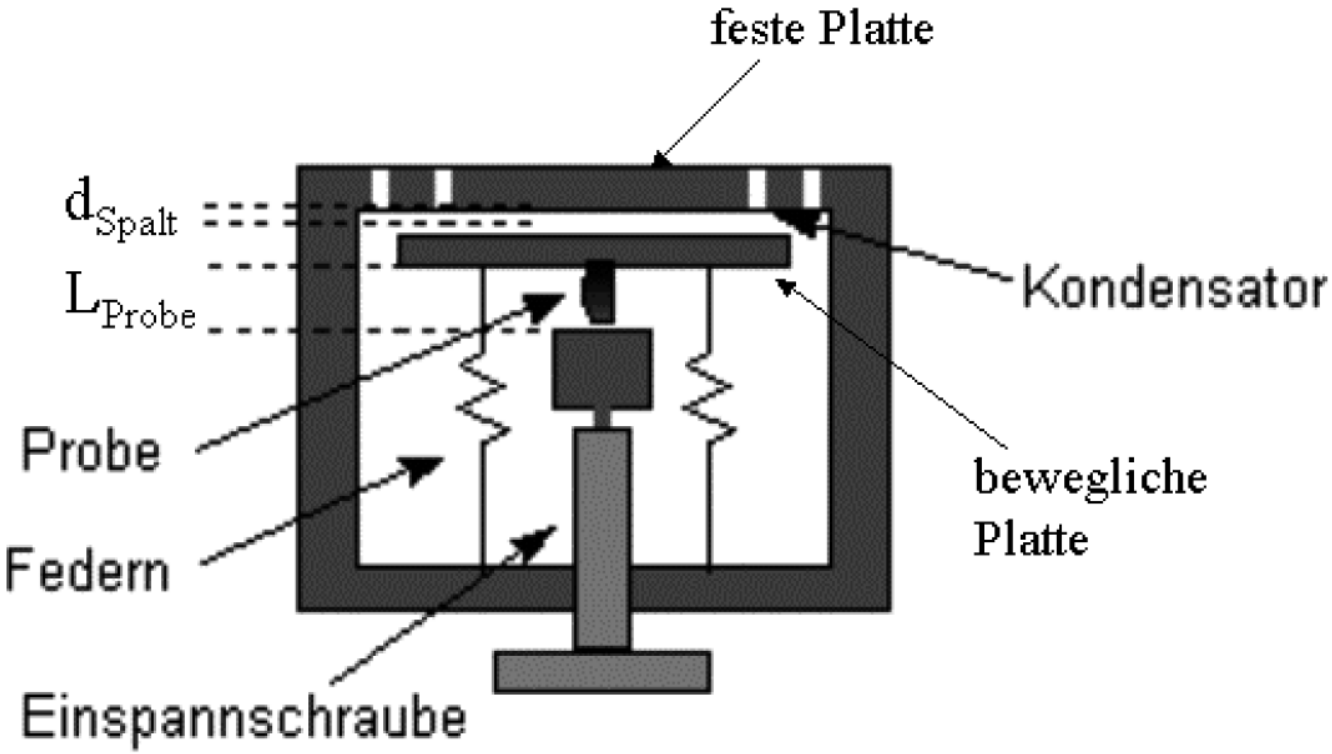

O. Heyer, Diploma thesis, Universität zu Köln, 2005

Capacitive dilatometer

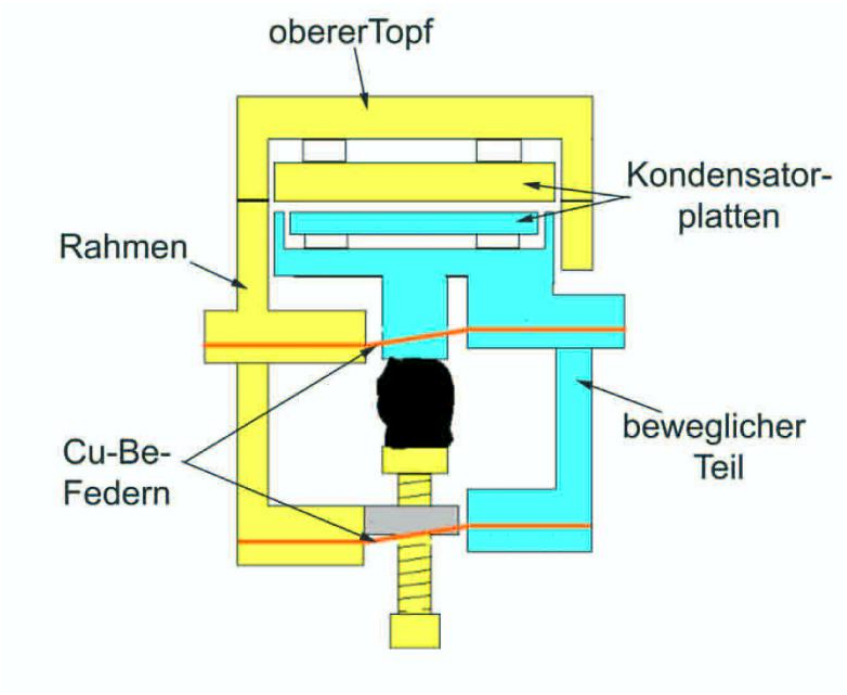

O. Heyer, Diploma thesis, Universität zu Köln, 2005

Sample environment: low T; high B

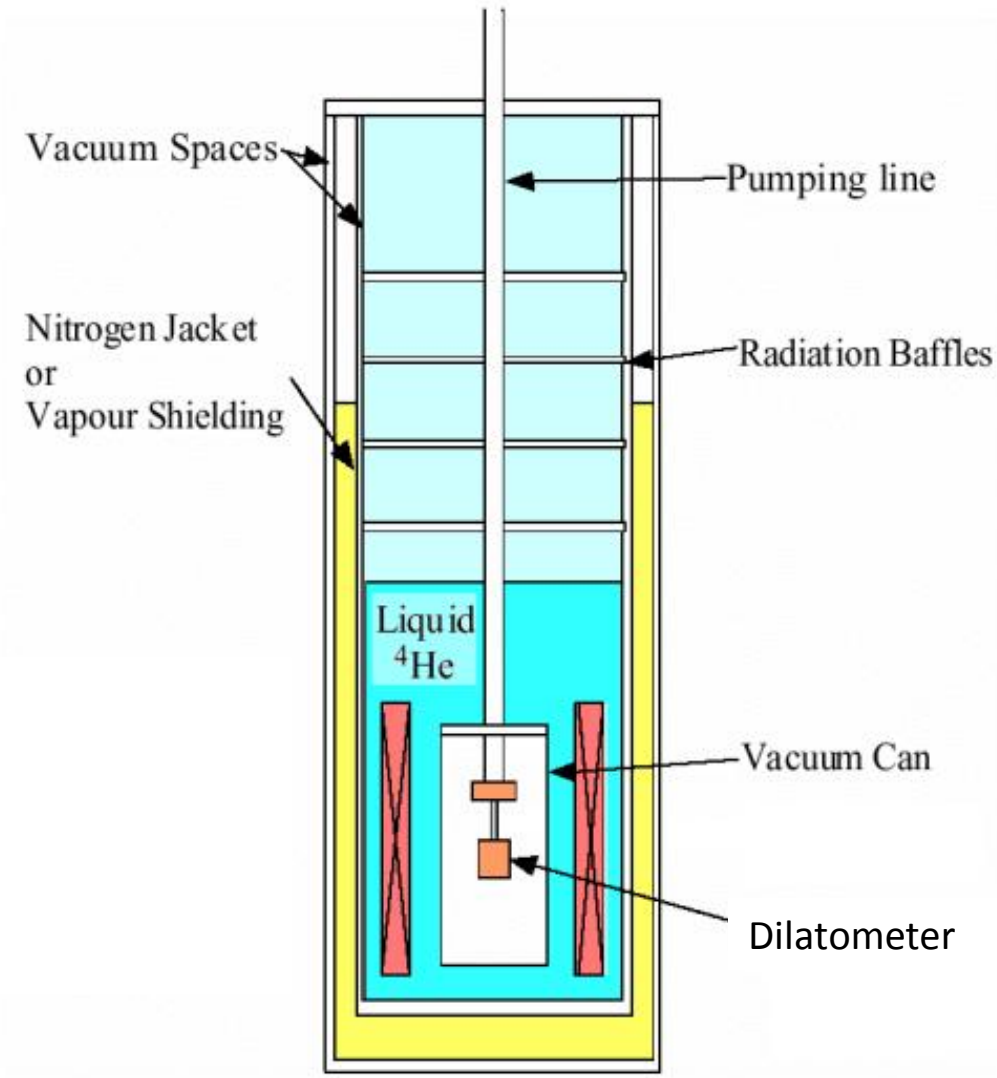

H. Michor, TU Wien

Ice calorimeter

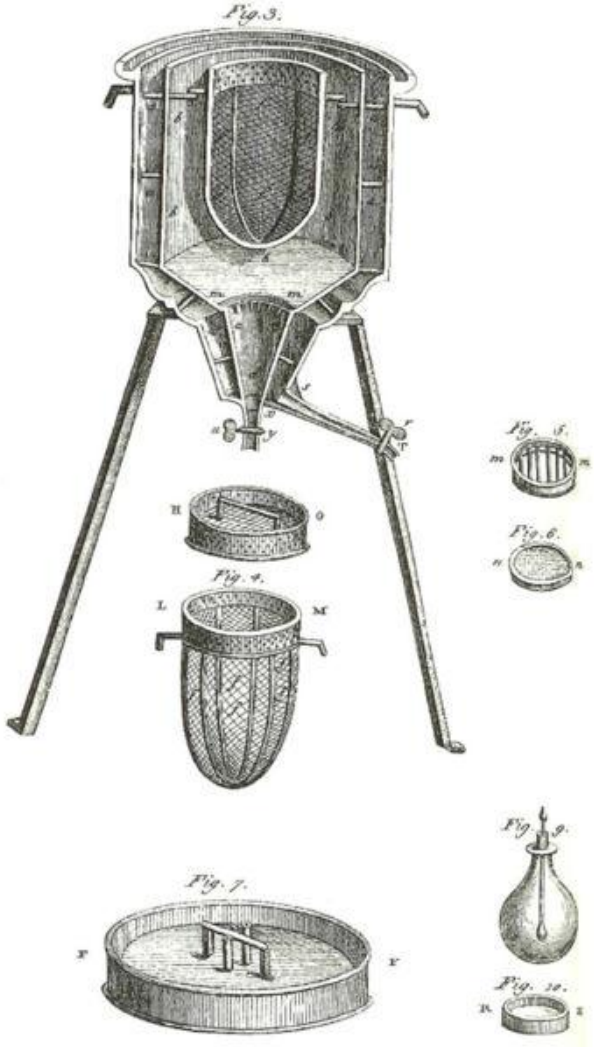

Laplace, Lavoisier 1782

Nernst method

NERNST (step heating)

$$C\left(\frac{T_E+T_A}{2}\right) = \frac{I_H \times U_H \times \Delta t}{T_E - T_A} = \frac{Q}{\Delta T}$$

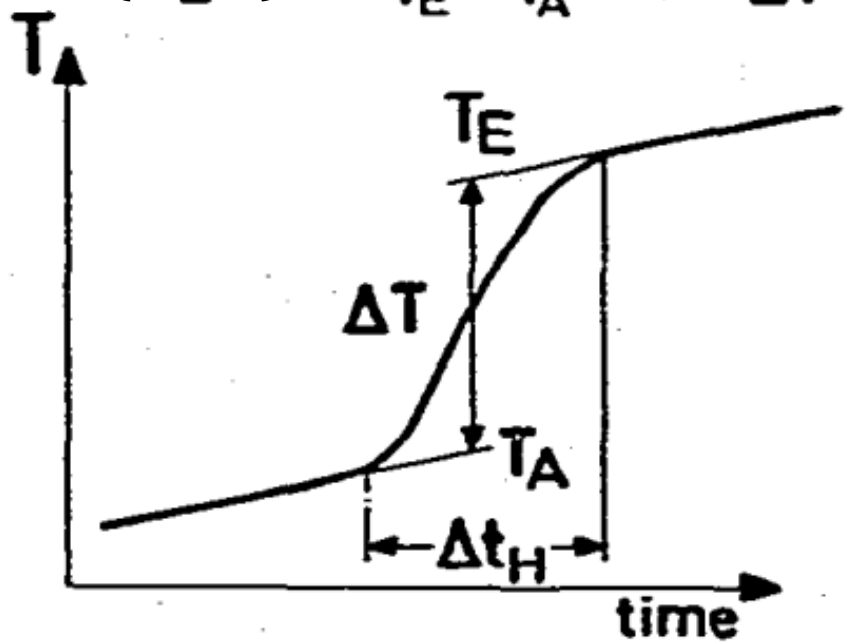

Continious heating

$$C(T) = \frac{I_H \times U_H}{(dT/dt)}$$

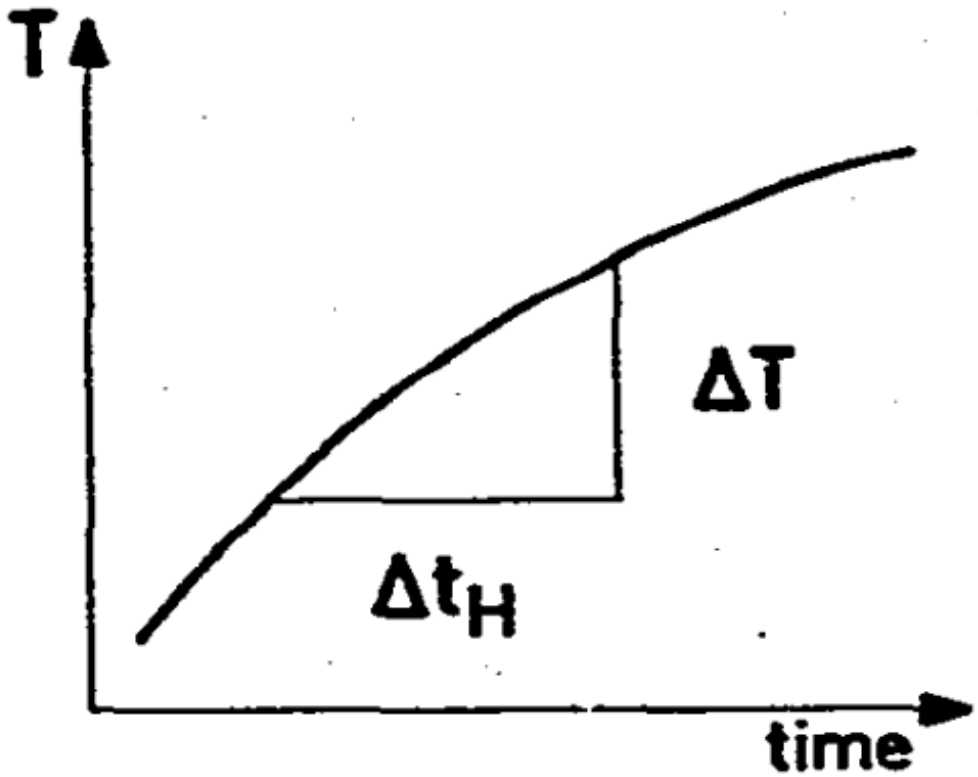

Relaxation time method

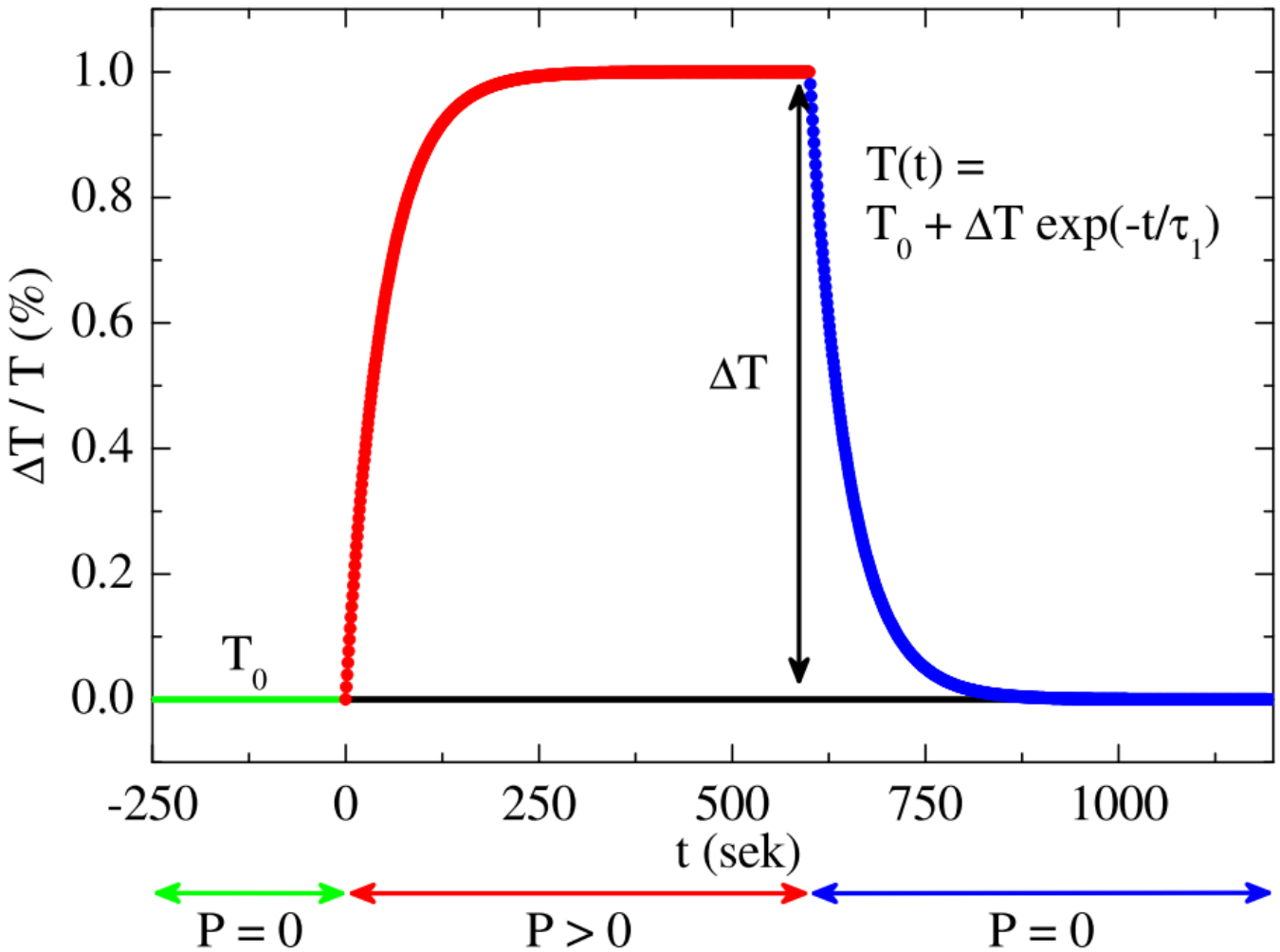

M. Kriener, PhD-thesis, Universität zu Köln, 2005

Example: S=1/2, T_c=10 K

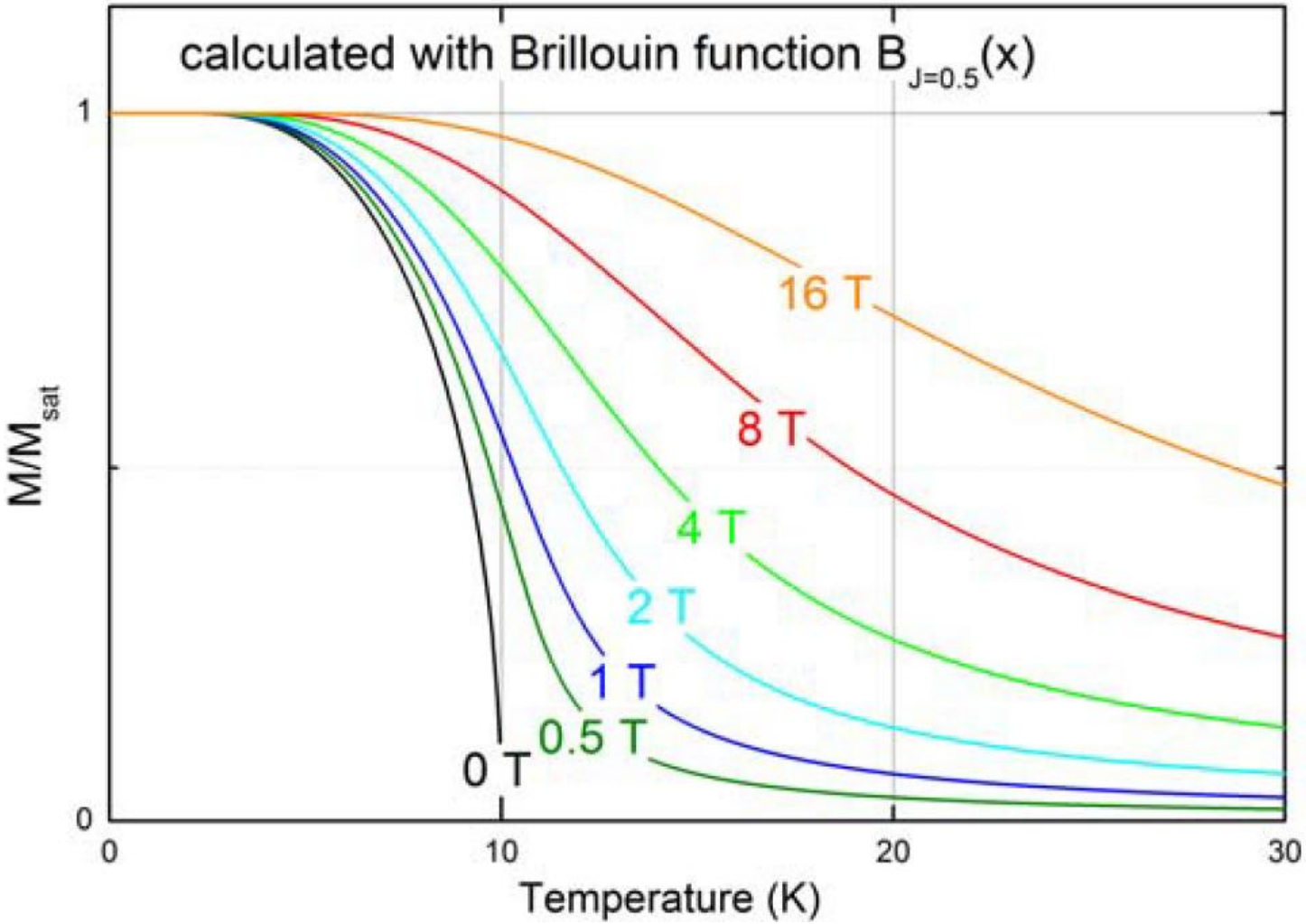

O. Heyer, PhD-thesis, Universität zu Köln, 2011

Model system: EuC_2

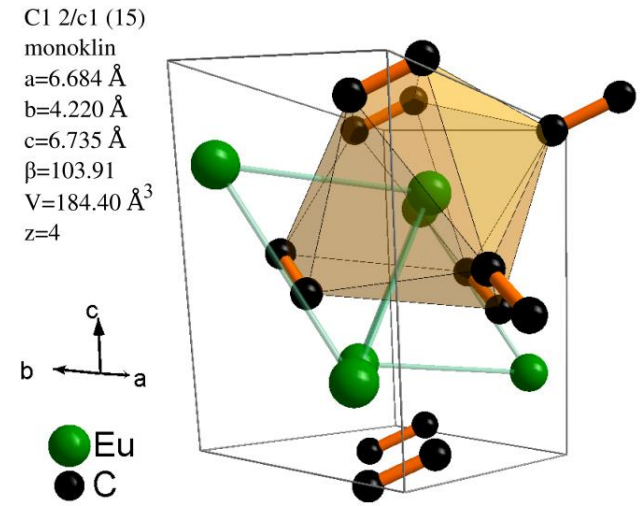

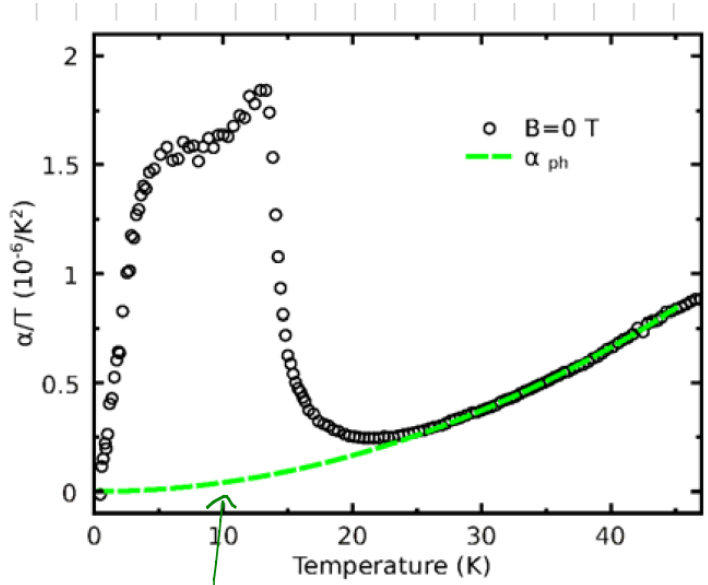

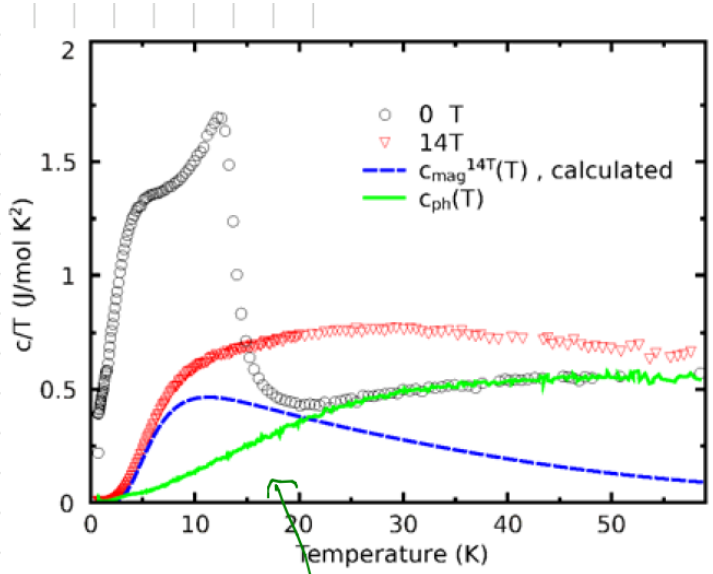

$\alpha = \alpha_{ph} + \alpha_{mag}$

$c_p = c_p^{phon} + c_p^{mag}$

O. Heyer, PhD-thesis, Universität zu Köln, 2011

Temperature regimes

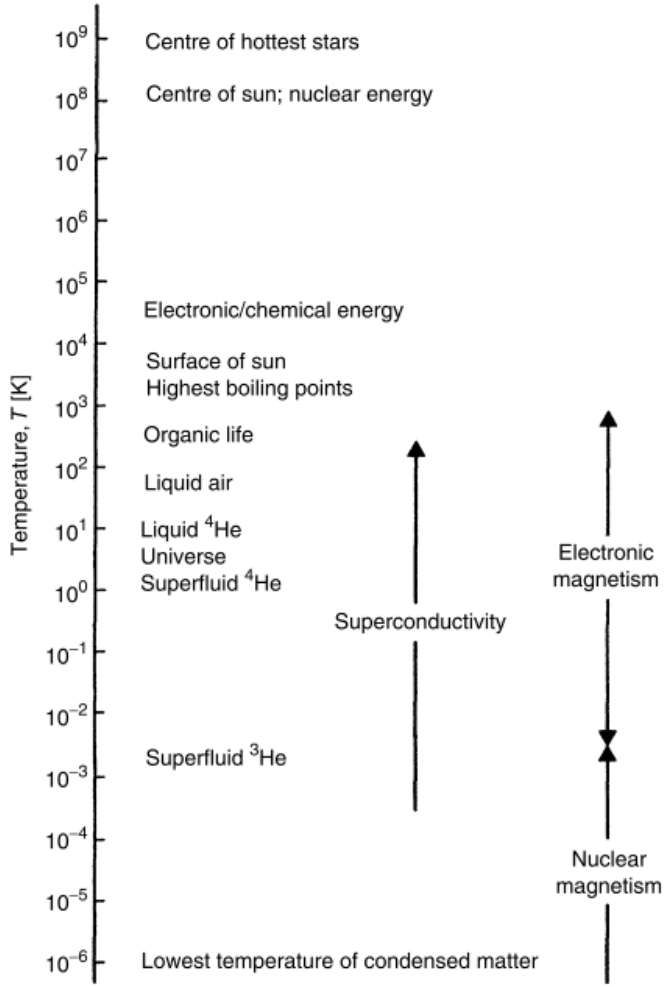

Fig. 1.1. Logarithmic temperature scale with some characteristic phenomena

Frank Pobell, Matter and Methods at Low Temperatures

History of low T

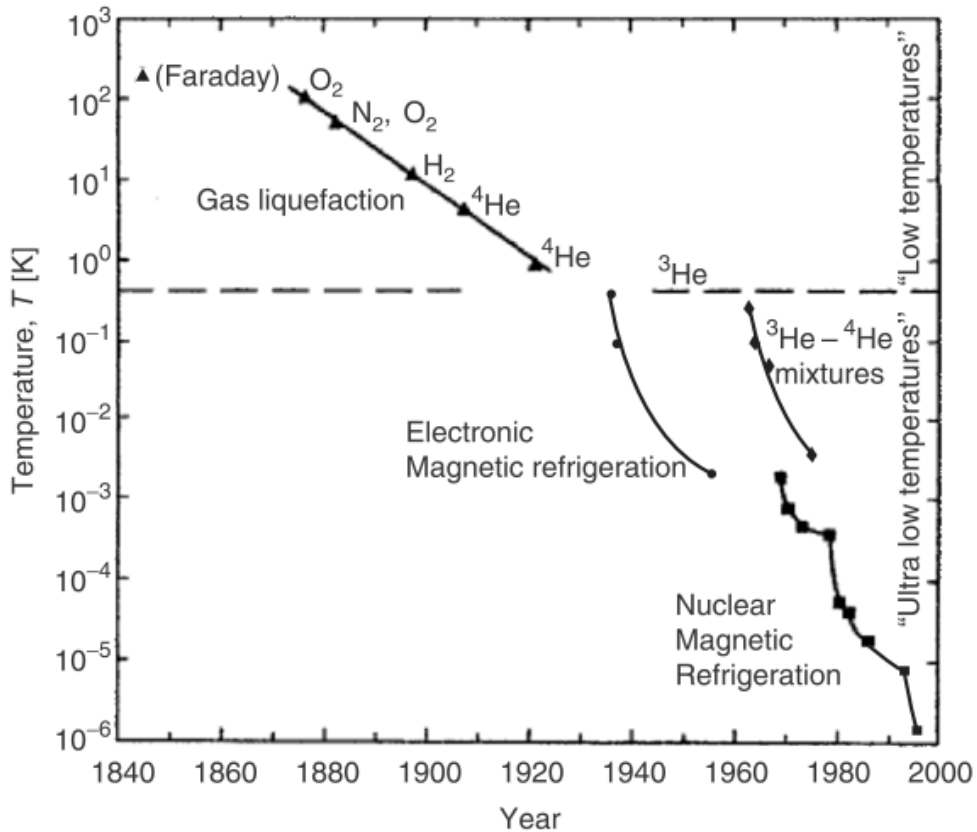

Fig. 1.2. Historical development of refrigeration temperatures of condensed matter, starting about 160 years ago with Faraday's gas liquefaction. The low temperature range was made accessible by liquid air, liquid H_2 and liquid ^{4}He (▲). Ultralow temperatures were attained by magnetic refrigeration with electronic magnetic moments (•) and later with nuclear magnetic moments (■). Refrigeration with liquid ^{3}He and liquid ^{3}He–^{4} He mixtures (♦) developed as the rare helium isotope became available in sufficient quantities

Frank Pobell, Matter and Methods at Low Temperatures

Refrigeration techniques

Table 1.1. Refrigeration techniques. The methods which dominate in the three temperature ranges are in italics

Temperature range		Refrigeration technique	Available since	Typical $T_{\min}$	Record $T_{\min}$
I	Kelvin	Universe			2.73 K
		Helium-4 evaporation	1908	1.3 K	0.7 K
		Helium-3 evaporation	1950	0.3 K	0.23 K
II	Milli-kelvin	**^{3}He–^{4}He dilution**	1965	10 mK	2 mK
		Pomeranchuk cooling	1965	3 mK	2 mK
		Electronic magnetic refrigeration	1934	3 mK	1 mK
III	Micro-kelvin	**Nuclear magnetic refrigeration**	1956	100 μK	1.5 μK[a]

[a]The given minimum temperature for the microkelvin temperature range is the *lattice* (*electronic*) *equilibrium* temperature. *Nuclear spin* temperatures as low as 0.3 nK have been reached (Table 10.2)

Frank Pobell, Matter and Methods at Low Temperatures

Stirling process

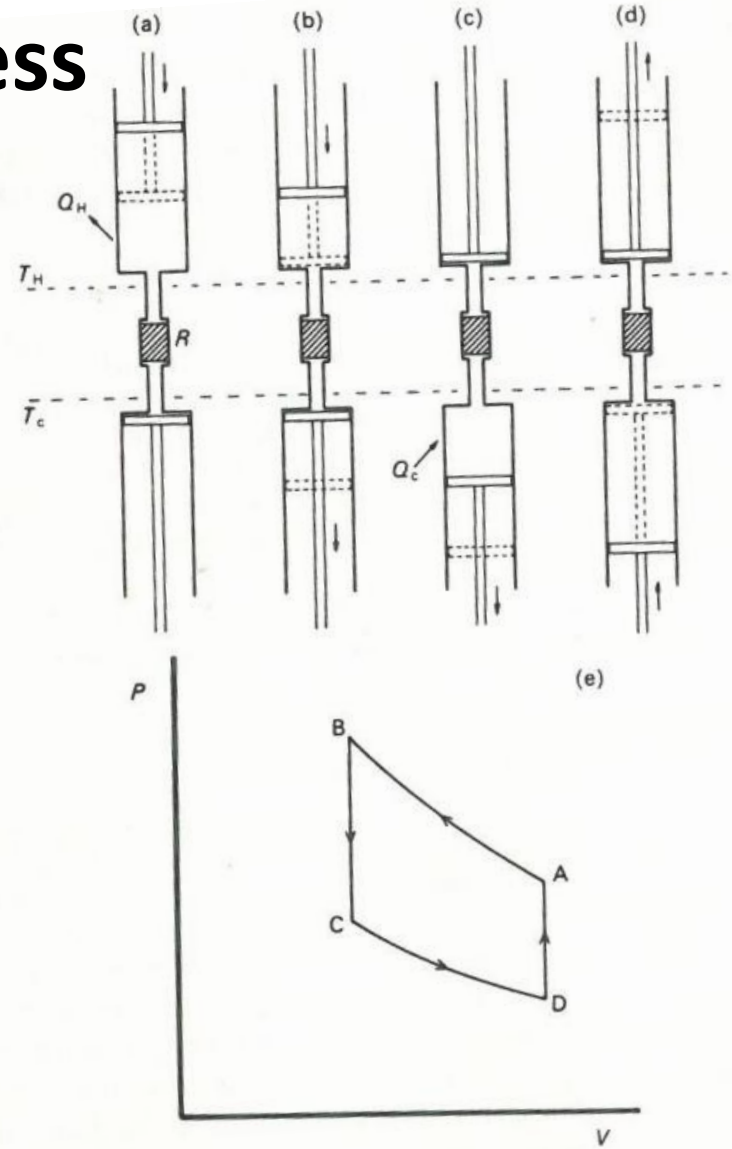

Figure 1.4 The Stirling refrigeration cycle: (*a*)–(*d*) represent different positions of the pistons and (*e*) is the corresponding pressure-volume indicator diagram for the cycle. For description of operation, see text.

McClintock, Meredith, Wigmore, Matter at Low Temperatures

Joule-Kelvin effect

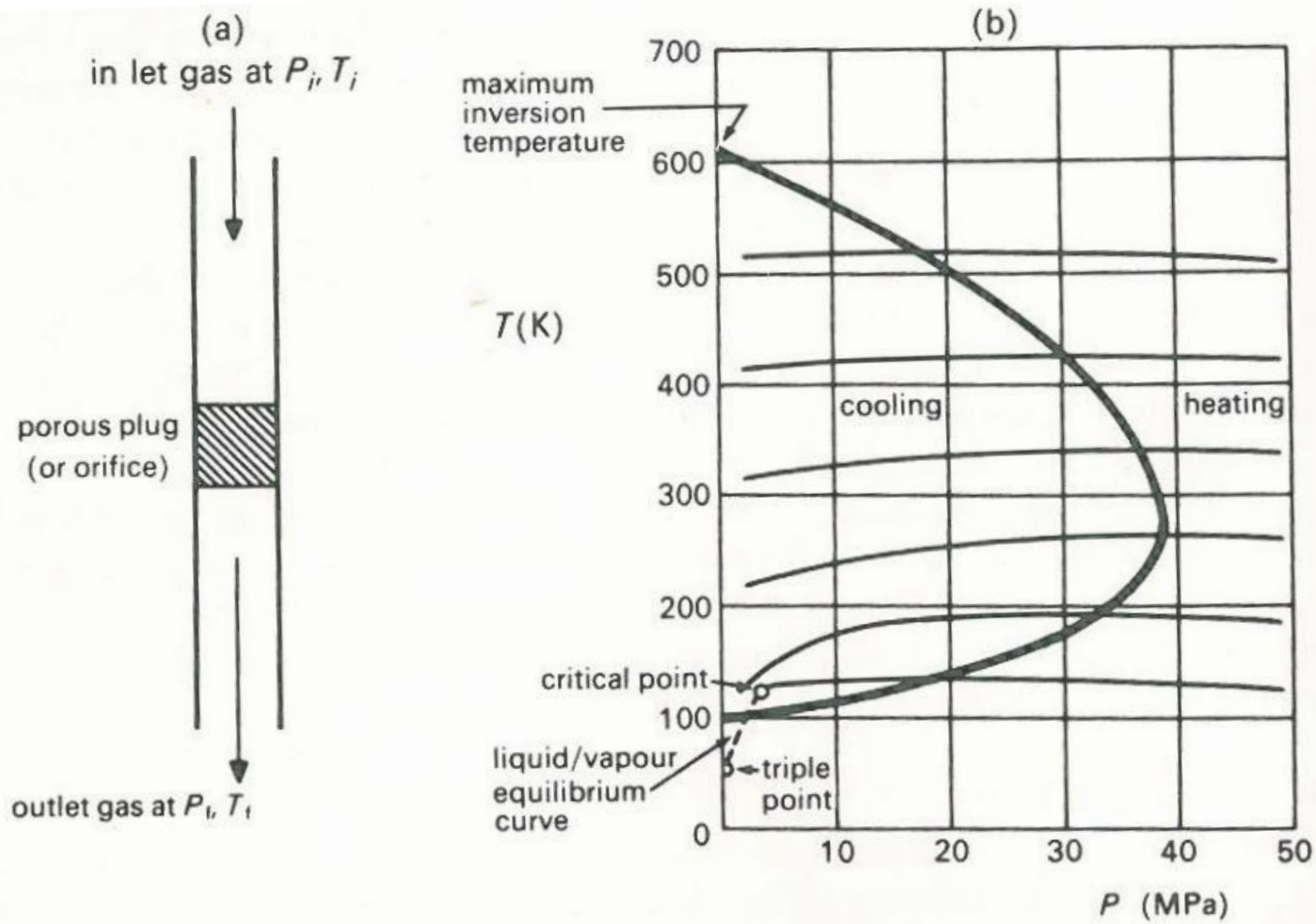

Figure 1.5 The Joule–Kelvin effect. (*a*) When gas is allowed to expand through a porous plug or orifice it may become either warmer or cooler, but its molar enthalpy remains constant. (*b*) Examples of isenthalps, for nitrogen. For pressures to the left of the inversion curve (bold line) cooling will occur on expansion.

Joule-Kelvin effect

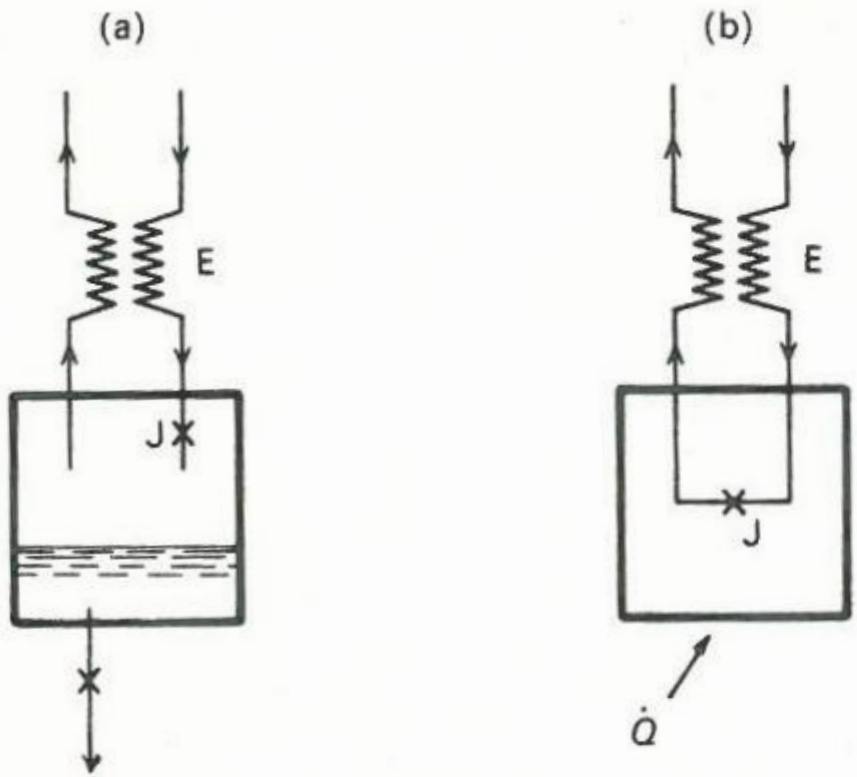

Figure 1.6 (*a*) Principle of operation of liquefier based on Joule–Kelvin expansion. The gas expands through valve *J*, some of it liquefies, and the outgoing cold gas cools the incoming gas stream through the heat exchanger *E*. (*b*) Virtually the same arrangement will serve as a refrigerator in which a heat flow $\dot{Q}$ can be absorbed at the cold end of the system, but no liquid is collected.

Properties of cryoliquids

subst.	T_b (K)	T_m (K)	T_{tr} (K)	P_{tr} (bar)	T_c (K)	P_c (bar)	lat. heat, L (kJ l^{-1})	vol% in air
H_2O	373.15	273.15	273.16	0.06*	647.3	220	2,252	–
Xe	165.1	161.3	161.4	0.82	289.8	58.9	303	0.1×10^{-4}
Kr	119.9	115.8	114.9	0.73	209.4	54.9	279	1.1×10^{-4}
O_2	90.1	54.4	54.36	0.015	154.6	50.4	243	20.9
Ar	87.2	83.8	83.81	0.69	150.7	48.6	224	0.93
N_2	77.2	63.3	63.15	0.13	126.2	34.0	161	78.1
Ne	27.1	24.5	24.56	0.43	44.5	26.8	103	18×10^{-4}
n-D_2	23.7	18.7	18.69	0.17	38.3	16.6	50	–
n-H_2	20.3	14.0	13.95	0.07	33.2	13.2	31.8	0.5×10^{-4}
^{4}He	4.21	–	–	–	5.20	2.28	2.56	5.2×10^{-4}
^{3}He	3.19	–	–	–	3.32	1.15	0.48	–

* The exact value is $P_{tr} = 61.1657$ mbar

^{3}He-^{4}He phase diagram

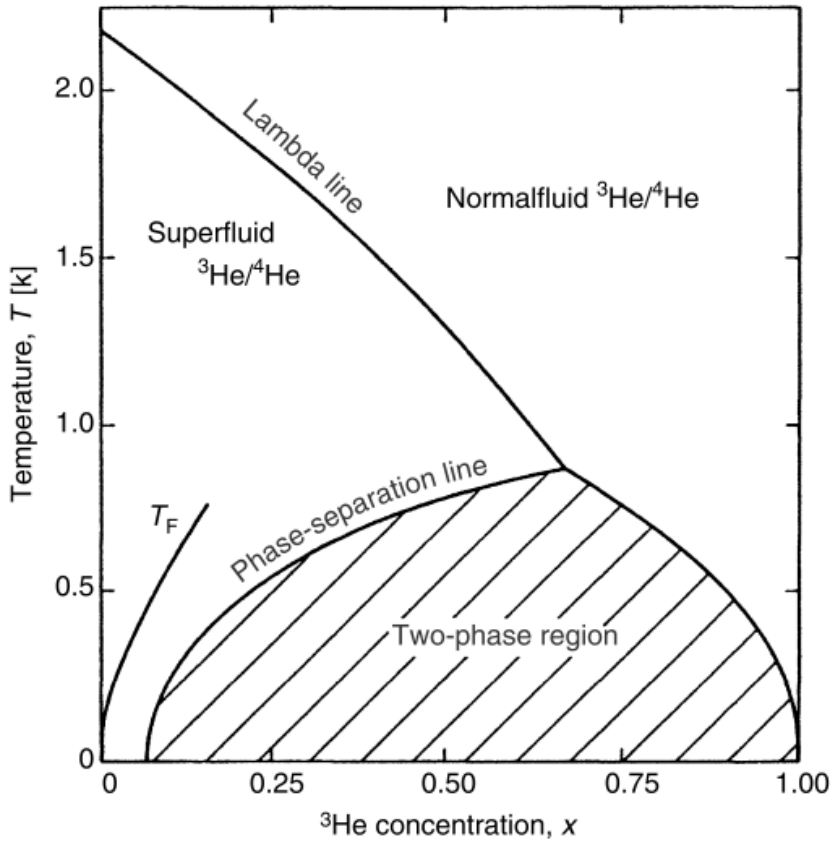

Fig. 7.1. Phase diagram of liquid ^{3}He–^{4}He mixtures at saturated vapour pressure. The diagram shows the lambda line for the superfluid transition of ^{4}He, the phase separation line of the mixtures below which they separate into a ^{4}He-rich and a ^{3}He-rich phase, and the line of the Fermi temperatures T_F of the ^{3}He component (From [7.11, 7.17] which give references to the original work from which data were taken to construct this phase diagram)

Frank Pobell, Matter and Methods at Low Temperatures

Schematic ^{3}He-^{4}He dilution refrigerator

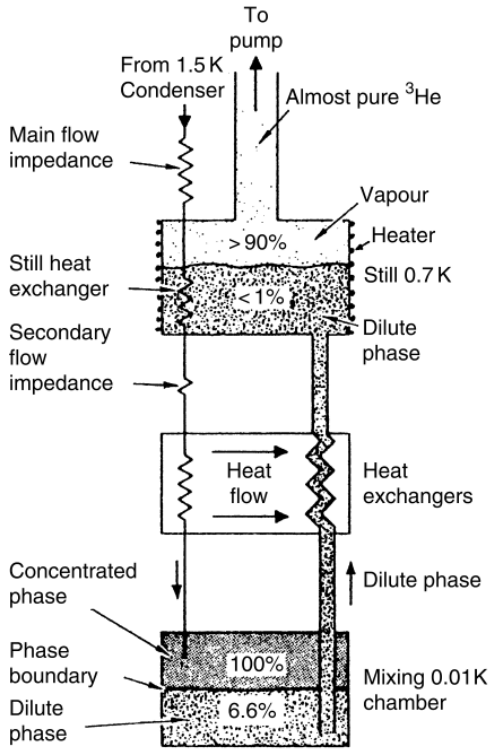

Fig. 7.9. Schematic ^{3}He–^{4}He dilution refrigerator. This part will sit in a vacuum chamber that is immersed in a ^{4}He bath at 4.2 K. The incoming ^{3}He gas is condensed on a continuously operating ^{4}He pot at 1.5 K (Sect. 5.2.4)

Frank Pobell, Matter and Methods at Low Temperatures

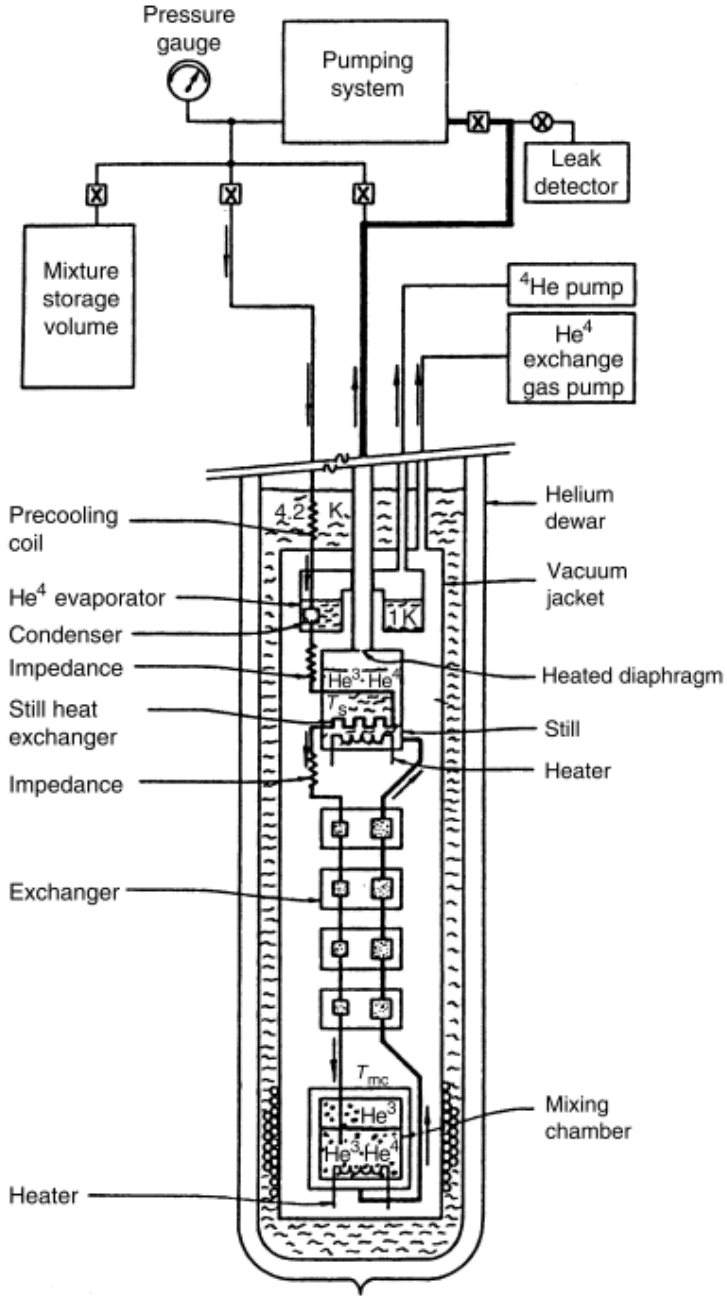

Fig. 7.16. Schematic of a typical ^{3}He–^{4}He dilution refrigerator with four heat exchangers [7.6]

Frank Pobell, Matter and Methods at Low Temperatures